Title
Non-uniform Erosion and Surface Evolution of Plasma-Facing Materials for Electric Propulsion

Author
Matthes, Christopher Stanley Rutter

Publication Date
2016

Peer reviewed|Thesis/dissertation

University of California
Los Angeles

Non-uniform Erosion and Surface Evolution of Plasma-Facing Materials for Electric Propulsion

A dissertation submitted in partial satisfaction
of the requirements for the degree
Doctor of Philosophy in Aerospace Engineering

by

Christopher Stanley Rutter Matthes

2016

Abstract of the Dissertation

Non-uniform Erosion and Surface Evolution of Plasma-Facing Materials for Electric Propulsion

by

Christopher Stanley Rutter Matthes

Doctor of Philosophy in Aerospace Engineering

University of California, Los Angeles, 2016

Professor Nasr M. Ghoniem, Chair

A study regarding the surface evolution of plasma-facing materials is presented. Experimental efforts were performed in the UCLA Pi Facility, designed to explore the physics of plasma-surface interactions. The influence of micro-architectured surfaces on the effects of plasma sputtering is compared with the response of planar samples. Ballistic deposition of sputtered atoms as a result of geometric re-trapping is observed. This provides a *self-healing* mechanism of micro-architectured surfaces during plasma exposure. This result is quantified using a QCM to demonstrate the *evolution* of surface features and the corresponding influence on the instantaneous sputtering yield. The sputtering yield of textured molybdenum samples exposed to 300 eV Ar plasma is found to be roughly $\frac{1}{2}$ of the corresponding value of flat samples, and increases with ion fluence. Mo samples exhibited a sputtering yield initially as low as 0.22±8%, converging to 0.4±8% at high fluence. Although the yield is dependent on the initial surface structure, it is shown to be transient, reaching a steady-state value that is independent of initial surface conditions. A continuum model of surface evolution resulting from sputtering, deposition and surface diffusion is also derived to resemble the damped Kuramoto-Sivashinsky (KS) equation of non-linear dynamics. Linear stability analysis of the evolution equation provides an estimate of the selected wavelength, and its dependence on the ion energy and angle of incidence. The analytical results are confirmed by numerical simulations of the equation with a Fast Fourier Transform method. It is shown that for an

initially flat surface, small perturbations lead to the evolution of a selected surface pattern that has nano-scale wavelength. When the surface is initially patterned by other means, the final resulting pattern is a competition between the "templated" pattern and the "self-organized" structure. Potential future routes of research are also discussed, corresponding to a design analysis of the current experimental study.

The dissertation of Christopher Stanley Rutter Matthes is approved.

Richard E. Wirz

Jeffrey D. Eldredge

Jaime Marian

Nasr M. Ghoniem, Committee Chair

University of California, Los Angeles

2016

Dedicated to my grandfather, Dr. H. P. Secher,
whose example taught me the importance of education.

Table of Contents

List of Figures

List of Tables

Acknowledgments

I am extremely grateful for all the people who have played a role in carrying out this work, as it is very clear to me that the completion of this project would be impossible without the help of countless individuals.

Firstly, I would like to offer endless thanks to Professor Ghoniem, who has been an exceptional advisor to me the past few years. His experience, wisdom, patience, and vision for my work has sustained me through my career at UCLA, and has helped me grow as a researcher and person.

I would also like to thank Professor Wirz and his research group for support and guidance on the experimental arm of my research. Their hard work has been essential in producing the results presented here. In particular, I'm grateful for the time and energy put forth by Chris Dodson and Gary Li in carrying out the experiments and providing great efforts to improve the experimental facilities. Special thanks to Taylor Matlock for his continual support and presence throughout the project, as well as Dan Goebel, who has been an infinite source of technical knowledge and advice.

I am also appreciative to my thesis committee members, Professor Eldredge and Professor Marian, who have been gracious and generous in their time and energy.

Much thanks goes to my lab mates, David Rivera, Andrew Sheng, and Edward Gao, who have been there with me through many classes, discussions, debates, and meetings. Their friendship and support has motivated me throughout the entire process. Likewise, special thanks goes to Giacomo Po, who has taught me a great deal and continually provided valuable insight and encouragement. Thanks also to Tamer Crosby and Can Erel, whose presence in the lab has provided me with a great example for work ethic and eagerness.

Thanks to my faithful friends, Kendall Partie and Kene Izuchukwu, who have developed

me as a person and stood by me through every moment these past couple years. To my wonderful fiancée and best friend, Jenny, who inspires me every day and has always been completely devoted to supporting my present and future dreams. I couldn't imagine a better partner, teammate, and supporter.

Finally, I would like to thank my incredibly loving and supportive parents Gerald and Margaret, who are the ones who made this all possible by putting me through college and showing me the value of education and ambition. For my Mom, who traveled with me to Huntsville, Alabama the moment I told her I was interested in aerospace. She has always believed in me and has constantly shown me my potential throughout my life. For my Dad, who traveled with me to Los Angeles and helped me get established when this process began. He has always been an example to me of creativity, and shown me the importance of taking initiative in my life. Thanks also to my siblings, Peter and Lydia, who have helped make me the person I am today. I am grateful to have them as family.

Vita

2012	B.S. (Mechanical Engineering), Michigan State University.
2013	M.S (Mechanical Engineering), University of California, Los Angeles.
2013–2016	Teaching Assistant, University of California, Los Angeles.
2012–present	Research Assistant, MATRIX Laboratory, University of California, Los Angeles.

Publications and Presentations

CS Matthes, NM Ghoniem , GZ Li, TS Matlock, DM Goebel, and RE Wirz. Fluence-Dependent Sputtering Yield of Micro-architectured Materials. Submitted to Applied Surface Science, 2016.

CS Matthes, NM Ghoniem, and D Walgraef. Theory & Simulations of Ion-Induced Surface Nano- Patterning. In preparation for submission to Physical Review B, 2016.

GZ Li, TS Matlock, DM Goebel, CA Dodson, CS Matthes, NM Ghoniem, and RE Wirz. In-situ sputtering yield measurements of molybdenum bombarded by a cusped argon plasma. Submitted to Plasma Sources Science and Technology, 2016.

NM Ghoniem, CS Matthes, D Walgraef. The Multiscale Materials Modeling Conference (MMM). Berkeley, CA. October, 2014. Theory, Modeling, and Experiments of Nano-structured surfaces by Plasma Ions.

NM Ghoniem, CS Matthes, RE Wirz, TS Matlock, et al. The International Conference on Metallurgical Coatings and Thin Films (ICMCTF). San Diego, CA. April, 2016. Erosion and Self-Healing of Micro- architectured Materials for Space Electric Propulsion.

CHAPTER 1

Motivation and Introduction

1.1 Electric Propulsion Overview

Electric propulsion (EP) uses high exhaust velocities to achieve thrust with a low amount of propellant relative to combustive propulsion methods. For space applications, this technology is particularly useful as it allows for significant reduction in launch mass. Regarding spacecraft design, the primary concerns for EP systems include the provision of electrical power necessary for the desired thrust output, as well as the need to dissipate thermal power in the form of waste heat that results from operation[23].

The three main performance factors considered in EP engines are thrust, specific impulse (I_{sp}), and efficiency. The most prominent electric propulsion technologies are the ion and Hall thrusters because of their performance capabilities. Ion thrusters generate plasma and electrostatically withdraw ions from the plasma using a biased grid, accelerating them to high velocities. Ion thrusters achieve high efficiency and specific impulse. Hall thrusters use the Hall effect to produce plasma by trapping electrons in a magnetic field and using them to ionize gas particles. An electric field perpendicular to the magnetic field accelerates the ions to high velocities to produce thrust. Hall thrusters generally have lower efficiency and I_{sp} than ion thrusters, but produce higher thrust and have a simpler design.

An ion thruster contains three main components: the plasma generator, the accelerator grids, and the neutralizer cathode. Plasma is generated by the discharge anode and cathode, then electrostatically accelerated through the grids, where the neutralizer cathode injects electrons into the beam to neutralize the charge.

Likewise, a Hall thruster is comprised of three elements: a cathode, a discharge region, and the magnetic field generator. A radial magnetic field confines electrons traveling to the anode and causes them to travel around the thruster axis, producing a Hall-effect current. These electrons then ionize gas fed into the discharge channel and follow the electric field between the anode and cathode and exit the channel. A common limiting factor in conventional Hall thrusters comes from the degradation of the discharge channel walls near the exit plane of the thruster, resulting in degradation of the magnetic pole pieces and affecting the performance and lifetime of the thruster[60]. In order to combat the erosion of discharge channel walls, magnetic shielding has been implemented to prevent the magnetic field lines from intersecting with the discharge channel walls[10]. Figure 1.1 illustrates the lines of force generated by the magnetic pole pieces that prevent ions from degrading the insulating material.

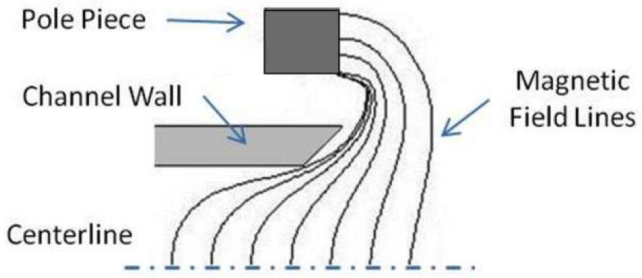

Figure 1.1: Lines of force on a magnetically shielded Hall thruster[10]

Without magnetic shielding, gas particles ionized by the electric current are accelerated out of the discharge channel and degrade the insulator rings, leading to the wear illustrated in Figure 1.2. This wear occurs as ions are accelerated by the electric field, from the anode are to the cathode-potential plasma at the front of the thruster, and bombard the edges of the insulator rings at energies from 50-300 eV[23].

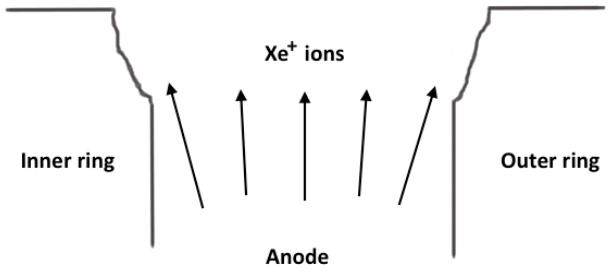

Figure 1.2: Wear to the insulator rings caused by ions exiting the discharge channel.

1.2 Electric Propulsion Plasma Environment

Ion and Hall thrusters typically use heavy inert gases such as argon and particularly xenon as the propellant. Lithium has also been used as a propellant, showing good results. These are desirable because they are non-hazardous, easily storable, and able to produce thrust more efficiently because of their large mass. There are a variety of parameters that characterize the plasma environment to which EP devices are exposed.

Table 1.1 shows the parameter quantities that describe the environment experienced in the operation of various types of EP thrusters[19]. It can be seen from the ion thruster data that different components experience varied levels of ion flux, heat flux, ion energies, etc., and therefore will have different lifetime considerations. In addition, plasma is composed of a combination of electrons and ions, which bombard the material surfaces of thruster components. It can be seen from the data in Table 1.1 that there are distinguishable conditions that are caused by each particle type.

As shown in the table, ion thrusters primarily use molybdenum as the standard electrode material due to its advantageous thermal and structural properties, as well as its resistance to sputter erosion. In addition, Mo has the ability to be chemically etched to form an aperture array[23]. Other refractory metals, such as tungsten and rhenium are similarly useful for these reasons. In Hall thrusters, insulator rings are generally composed of dielectric materials such as boron nitride (BN) or borosil (BN-SiO_2) due to their low sputtering yield and low

Table 1.1: Operational parameters of main EP Devices[19]

Device	Particle Flux (ions/m^2/s)	Particle Energy (eV)	Heat Flux (MW/m^2)	Ion Type	Material	Life Fluence (TJ/m^2)	Lifetime (years)
Ion Thruster							
–screen grid	3×10^{20}	25-50	.0025	Xenon	Mo	0.4	3-5
–accel grid	6×10^{18}	250-500	.0005		Mo	0.08	
–cathode	6×10^{21}	25-50	.05		Mo/W	7.5	
MPD Thruster							
–Electrons	1×10^{24}	50-100	8	electron	Cu, W	0.5	0.1-2
–Li Ions	2×10^{23}		1.6	Li		0.1	
Hall Thruster							
–Electrons	5×10^{22}	50-100	0.8	electron	Boron	50	1-2
–Xe Ions	1×10^{21}	50-300	0.05	Xe	nitride	3	

occurrence of secondary electron yield.

1.3 Characteristics of surface erosion as a limiting mechanism of material life

The most significant erosion mechanism in ion thrusters is wear on the accelerator grid. Resonant charge exchange between beam ions and neutral propellant gas particles generates a current of secondary ions downstream of the discharge chamber. This process, where an electron is passed from a propellant atom to a beamlet ion, results in a fast neutral atom and a slow thermal ion. The negatively charged accelerator grid attracts these slow ions, causing them to bombard the surface with enough energy to sputter material from the grid. Over time the grid either fails structurally, or the apertures become too large to prevent electron backstreaming.

Accelerator grid erosion happens in two main ways, as illustrated in Figure 1.3. First is barrel erosion, which occurs when ions are generated between the screen grid aperture and the accelerator grid. The ions bombard the inside surface of the accelerator grid aperture

and increase the size of the aperture barrel. The increased barrel diameter requires the grid to be more negatively biased in order for there to be a sufficient voltage potential to prevent backstreaming of neutralizer electrons into the discharge chamber. Failure due to barrel erosion occurs when backstreaming is not sufficiently preventable at the minimum grid voltage. The second erosion mechanism for the accelerator grid is due to ion bombardment on the downstream face of the accelerator grid. This process results from charge exchange ions that are generated in the region immediately after the accelerator grid before the beamlets merge, which are then attracted back to the negatively charged accelerator grid[62]. These ions impact the downstream surface of the accelerator grid and sputter material away. This type of erosion can lead to structural failure of the grid if the material erodes sufficiently.

Also of significant importance is screen grid erosion from the plasma discharge. This erosion, which is due to direct impingement of plasma ions on the upstream surface of the screen grid, occurs at ion impact energies near the plasma potential of 20-30 V. This leads to relatively uniform loss of the screen grid thickness, and is often considered the life-limiting mechanism due to possible structural failure of the screen grid.

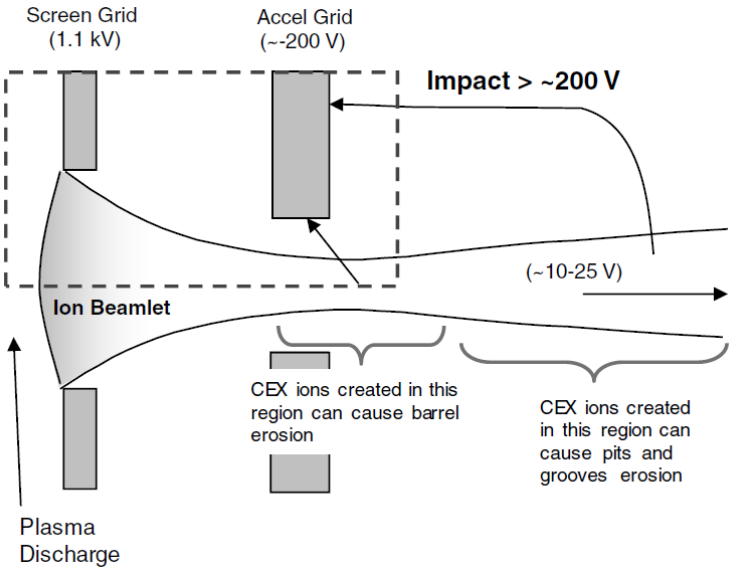

Figure 1.3: Charge exchange ion erosion mechanisms in an ion thruster. Image from Reference [62].

1.4 Materials and surface structures

Molybdenum is a commonly used material for the electrodes in ion thrusters. Mo and other refractory metals such as tungsten, and rhenium have a high resistance to sputter erosion, as well as possessing exceptionally resilient thermal and structural properties. Certainly, sputtering resistance is of critical importance in EP technologies, as the bombardment of ions is intrinsic to the physics of their operation.

In addition to material composition, surface geometry can play a significant role in the resilience and life of space EP devices. Micro-architecturing of material surfaces to produce dendrites, cones, and other structures on the surfaces of these devices through a chemical vapor deposition (CVD) process may be an effective way to solve degradation issues related to plasma exposure. It is expected that engineering of surface structures will allow for more resilient and lasting devices because of their improved performance in extreme plasma environments.

There are three general categories of micro-engineered (or micro-architectured) materials: reticulated, fractal, and dendritic surfaces. Reticulated structures are characterized by a network of interconnected fibers that comprise a porous or foam structure. Metallic foams have shown to exhibit favorable thermal management because of their high surface area-to-unit volume ratio, $< 20{,}000$ m^2/m^3[50]. These material structures are characterized by a network of interconnected ligaments, which can vary in size scale from the micron level to the millimeter range. They can be manufactured to porosities varying from 10 to 100 pores per inch (PPI). The second category, fractal geometries, possess a significant amount of folds in their surface structures. These remain a relatively unexplored type of formation, and offer great potential in their heat transfer and sputter resistance properties. Their size scale tends to be relatively large in size, with structures varying between tens to hundreds of microns in width. In addition, fractal coatings can vary in density, between closely packed fractal formations to more sparsely distributed structures.

Dendritic surface structures remain as the last category of micro-architectured geome-

tries. Figure 1.4 shows that there are many types of specific geometries that fall within the dendritic classification, with size scales varying between 1-2 nanometers to tens of microns in width. The improved behavior of architectured dendritic surfaces may be attributed to several factors. Thermal stresses are reduced, resulting from the capability of fine surface features to withstand a greater level of distortion. Secondly, net sputtering erosion from the ion bombardment is minimized because of geometric trapping of re-deposited atoms. Further, the higher surface area promotes better heat distribution over the sample, preventing localized overheating. These properties greatly enhance the longevity and resilience of materials used in space EP devices, which experience extreme plasma environments during regular operation.

The textured samples are classified according to the materials that are used to produce the various structures. These samples consist of various combinations of metals, including course tungsten over molybdenum and heavy molybdenum over dendritic rhenium, for example. The context of the words "course" and "heavy" indicate a thicker coating of the outer element, as opposed to "light," which refers to a thinner layer. Figure 1.4 shows a some instances of these type of structures at different magnifications.

1.5 Thesis Objectives

This thesis follows two main branches: experimental and computational. The experimental study was primarily aimed at observing the effects of micro-architectured surfaces on the evolution of materials exposed to plasma environments. The computational side of the research was aimed at modeling the evolution mechanisms experienced by materials subjected to plasma and ion bombardment. Figure 1.5 illustrates the respective and shared objectives of the two branches of this research. The primary objectives of the thesis may be grouped together as follows:

1. *Understand the competition between the various evolution mechanisms.*

   The overall goal of this research was to develop a deeper understanding of the many

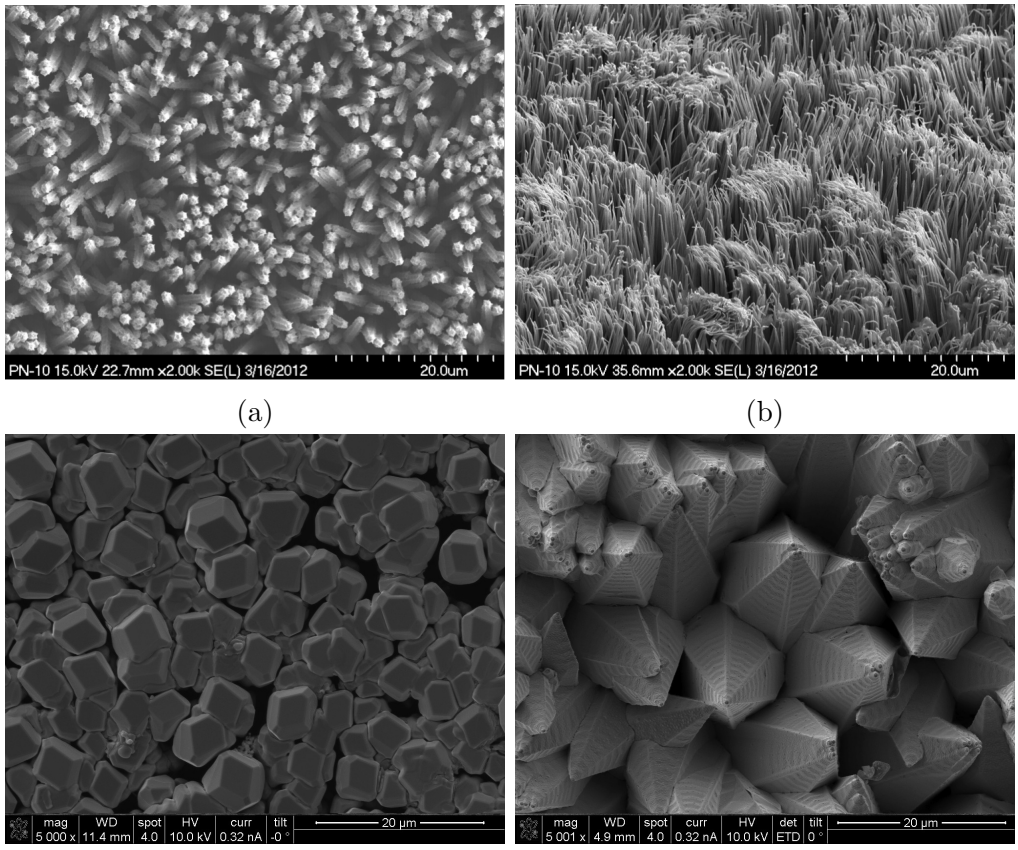

Figure 1.4: Dendritic surfaces. (a) Tungsten nodules (b) Evenly coated tungsten grass surface (c) Heavy Mo-coated Re nodules (d) Heavy Mo-coated Re spikes. Images (a) and (b) by Alp Sehirlioglu, Case Western Reserve; images (c) and (d) by C. Matthes

processes that occur during plasma bombardment, which is accomplished by both the experimental and computational branches. The evolution of material morphology is dependent on the balance of surface erosion with sputter deposition, where some of the the ablated material accumulates at a nearby location on the surface. In addition, surface diffusion processes affect the evolution response. The interaction of these mechanisms was studied, as well as the conditions that control each of their effects on the surface morphology.

2. *Develop a theoretical model for observing and predicting surface evolution.*

   Ion bombardment results in degradation of a material surface, the rate of which is dependent on surface geometry and plasma conditions. A theoretical framework was

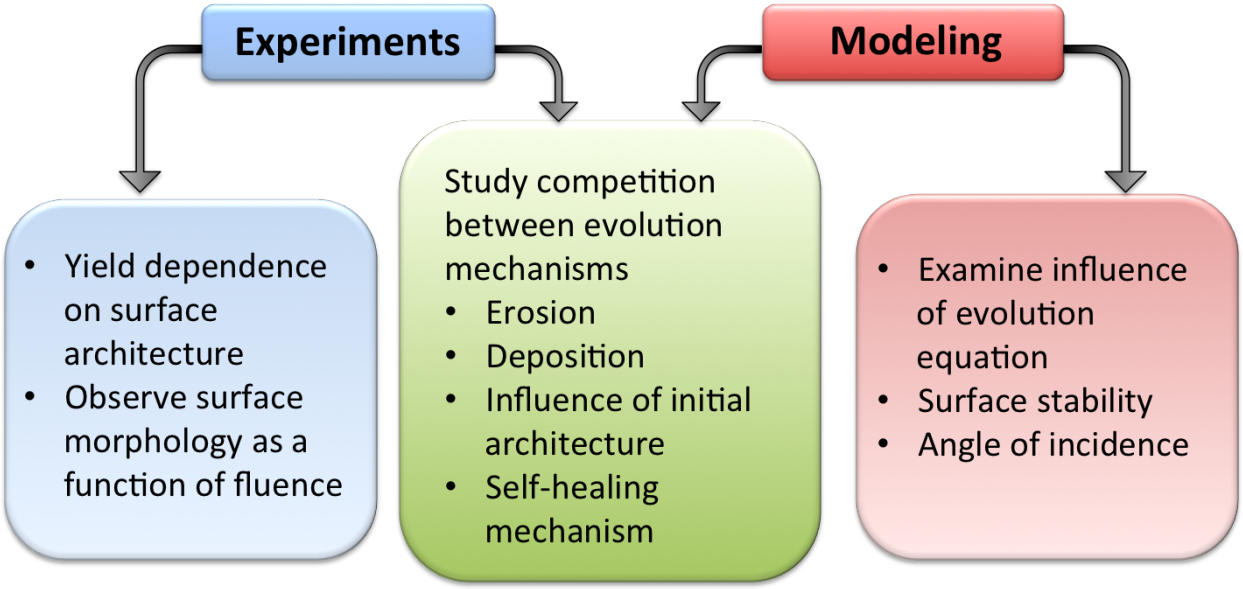

Figure 1.5: Thesis Objectives

developed by taking into account these variables. The model was used to predict and understand the erosion, deposition, and diffusive behavior of material surfaces with a given initial profile and particular ion parameters. The studied parameters included ion flux, ion energy, and angle of incidence. A numerical method was employed to simulate the evolution of the surfaces under selected ion conditions. Stability analysis was employed to validate the model by predicting the selected wavelength of periodic surface features.

3. *Quantify the relationship between surface architecture and the sputtering yield of materials.*

   Material samples with varying surface geometries were examined using both computational and experimental means. Observing the response of unique material architectures to plasma exposure provides a better understanding of the influence that surface geometry design may have on the reliability and longevity of materials in extreme environments. In addition, it was desired to quantify the effect of unique surface architecture on the sputtering yield of a material to better measure the mechanisms that control surface evolution.

CHAPTER 2

Review of experimental observations on erosion, deposition, and surface pattern formation

2.1 Surface Patterning

The fundamental physics of plasma-material interactions (PMI) has a wide range of applications across various technologies, including electric propulsion, plasma processing, microelectronic fabrication, and fusion energy devices. It is now appreciated that in PMI, the uniformity of plasma interaction with surfaces is the exception rather than the norm. Spatially non-uniform interaction leads to two potentially interesting areas of study. The first one is the possibility of fabricating surfaces with self-organized nano structures, and the second intriguing aspect is the potential surface self-healing as a result of immediate deposition of some of the sputtered atoms. The two areas are complementary is a sense, since spatial non-uniformity of PMI can destabilize even flat surfaces, and lead to self-organization, while an initially structured surface may tend to become more uniform via ballistic atom deposition. The objective of the present study is to focus on the second facet of PMI non-uniformity, in an attempt to explore how an initially structured surface can be designed to partially heal itself. Additionally, we wish to quantify the relationship between surface morphology and sputtering erosion rate. Understanding how surface structure and roughness affect the rate of atomic sputtering, and vice-versa, is a key consideration in engendering longevity and resilience of materials used in plasma devices, for example in electric propulsion applications.

Utilization of energetic ion beams to produce surface nano-patterns has been the subject of intense interest for a couple of decades. Experimental and theoretical efforts have focused

on understanding the influence of such parameters as the ion energy, flux, fluence, angle of incidence, and sample surface temperature on the formation of specific surface patterns. Early insights into the relationship between surface structure and the sputtering rate were presented by Sigmund [52], who formulated the theory of atomic sputtering from a flat surface. The theory was later expanded to consider the influence of surface roughening [53]. The basic idea is as follows. A collision cascade is formed downstream of an obliquely incident ion just beneath the surface, and the energy from the cascade causes ejection of surface atoms when their energy exceeds their binding energy. If the surface is not locally flat (rough), surface peaks will tend to eject less atoms (because the cascade is somewhat farther away), while valleys will tend to eject more atoms. This fundamental idea was further advanced by Bradley and Harper [6] (BH), who showed that surface instability ensues, and that roughening and patterning of surfaces bombarded with energetic ions may indeed be feasible. The basic BH equation for surface height evolution, h, balances the rate of roughening (which is proportional to the curvature, κ) with the relaxation rate attributed to surface diffusion[16]. This can be simply expressed as: $h_{,t} = -v_0 + S\kappa + B\kappa_{,ss}$, where the subscripts refer to the partial derivatives with respect to time, t, and arc length, s. A small-slope approximation, $\kappa \approx \nabla^2 h$, is generally used for the BH equation to relate the curvature to the height of the surface profile [37]. The coefficient S accounts for the roughening due to sputtering, taking into account angular dependence of incoming ions, B is the rate coefficient of surface diffusion, and v_0 is the normal erosion velocity for a flat surface. While the equation is limited, it provides a basic understanding of the physical effects that surface geometry can have on ion sputtering.

2.1.1 Angular Dependence

It has been observed by Navez, et. al.[42] that the bombardment of a clean glass surface with an ion beam of air will produce a new surface morphology based on the incidence angle, θ of the ion beam. The observed phenomenon was the formation of a ripple structures oriented perpendicular to the ion beam for incidence angles close to normal ($\theta = 0$), and parallel to the

ion beam for incidence angles close to grazing (Figure 2.1). This experimental phenomenon

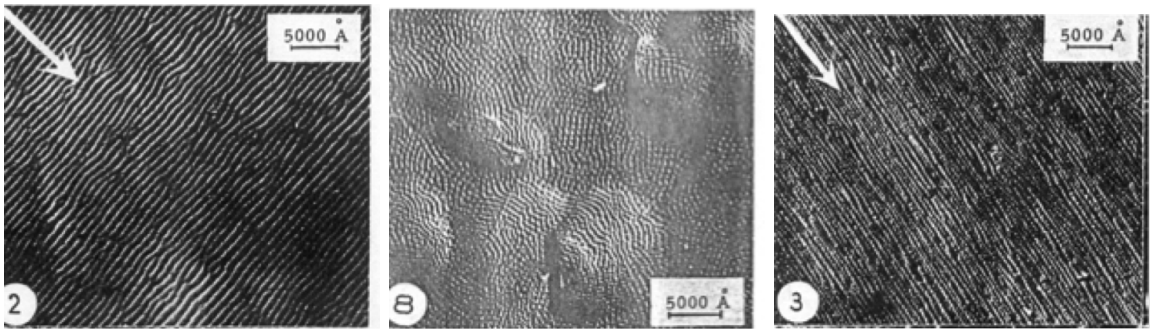

(a) (b) (c)

Figure 2.1: Experiment of Navez, et. al.[42] on glass. (a) Glass surface after 6 h bombardment, $\theta = 30$. The ripples align perpendicular to the beam. (b) $\theta = 0$ (c) $\theta = 80$. The ripples align parallel to the beam.

is analogous to wavelike structures formed by wind in a sand bed. This natural occurrence comes about due to the fluid-like behavior of sand particles, which can be considered as an immiscible fluid with air, moving at very different speeds[56]. The boundary between them can develop wavelike structures through an unstable process. If a small sand pile or hollow randomly forms, it will disrupt the airflow around it. In the case of a pile, the wind is slowed and can not carry as much sand with it. This causes continuously more sand to be deposited, making the pile grow larger. Similarly, the wind is sped up in a hollow, which results in more sand to be swept away and the hollow to grow deeper.

The formations caused by this process are qualitatively very similar to those resulting from ion bombardment, where the erosion of a solid surface is caused by the abrasive mechanism of ions hitting the material. Understanding the basic mechanisms of ripple formation in sand can allow for insight into the formation of surface features on materials subjected to ion bombardment.

2.1.2 Fluence Dependence

Figure 2.2 shows the surface patterns that result from increasing levels of ion fluence exposed to a highly ordered pyrolytic graphite (HOPG) surface with (0001) orientation to 5 keV Xe^+

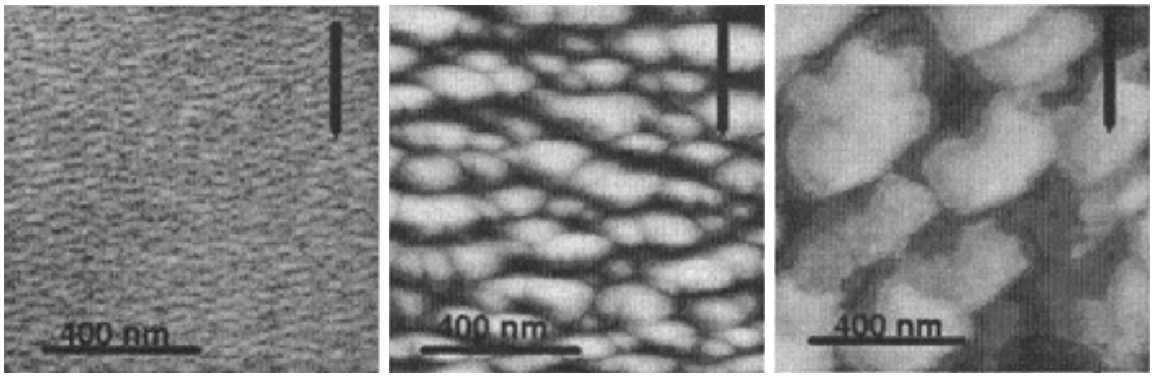

(a) (b) (c)

Figure 2.2: Eroded HOPG surfaces[24]. (a) Irradiation fluence of 5×10^{20} m^{-2} (b) Irradiation fluence of 2×10^{22} m^{-2} (c) Irradiation fluence of 5×10^{22} m^{-2}

ions, at increasing levels of ion fluence up to 6×10^{22} m^{-2}[24]. The wavelength is clearly dependent on fluence, where 2.2a shows the smallest nanostructures and 2.2c dramatically higher roughness. Fluence is a measurement of aggregate ion quantity over an area, so in the context of space EP, higher fluences correspond to longer operation. If the surfaces of materials used in EP devices mimicked the results seen in this experiment, since surface roughness directly proportional to operation time, older devices would exhibit roughened material surfaces.

2.1.3 Temperature Dependence

The influence of temperature on surface morphology was explored by Rusponi et al.[49] through ion bombardment experiments on silver surfaces using Ar^+ ions with an energy of 1 keV. The results are shown in Figure 2.3, where the dependence of surface morphology on temperature is considered. At low temperature 2.3a the surface is rough, without any clear level of organization. At T=230 K 2.3b a ripple structure begins to appear, where the wave crests are aligned along $< 100 >$. At higher temperatures the structure first develops into an array of rectangular mounds 2.3c; for even higher temperatures a ripple structure is formed, aligning along the $< 1\bar{1}0 >$ direction 2.3d, and becoming even more clear as the temperature heightens 2.3e.

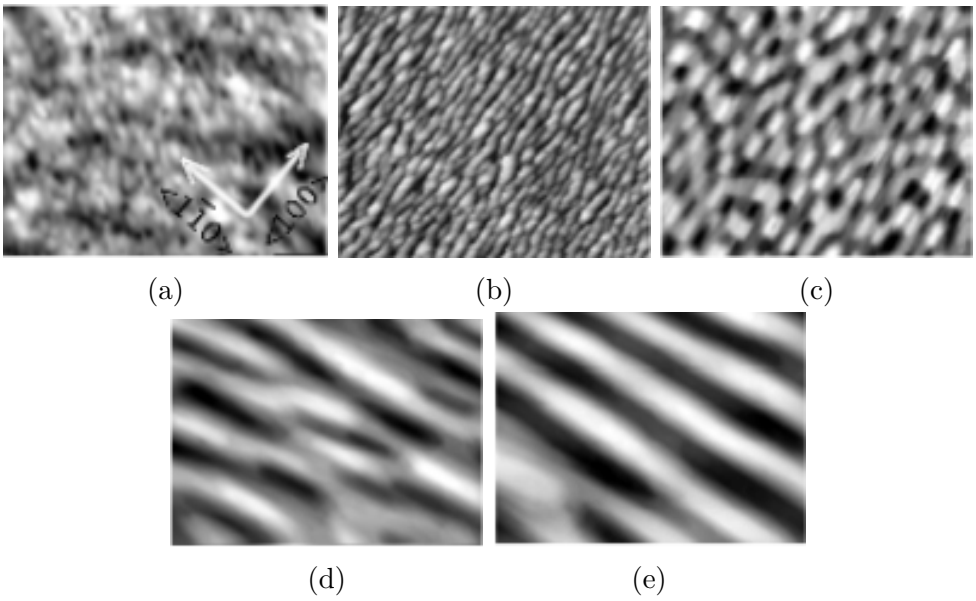

Figure 2.3: Ag(110) after ion sputtering at normal incidence[56]. (J = 4 $\mu A cm^{-2}$, t = 15 min, $\theta = 0$) for different temperatures. (a) 160 K; (b) 230 K; (c) 270 K; (d) 290 K; (e) 320 K

The tendency of surface structures to orient along a particular direction is attributed to the enhanced surface diffusion that occurs at higher temperatures. On the surface of metals such as Ag(110) and Cu(110), the in-channel direction, $< 1\bar{1}0 >$ is an easy pathway for the movement of adaptors and vacancies compared the cross-channel, or $< 001 >$ direction. Therefore, at higher temperatures where anisotropic surface diffusion is amplified, the ripple structures have a quicker path to organize in that orientation[11].

2.1.4 Erosive vs. diffusive regime

The temperature dependence of surface morphology explored in the previous section demonstrates the development of surface nanostructures, whose orientation is largely determined by the dominant diffusion direction. It is therefore useful to refer to the environment in which nanostructures appear according to this set of conditions the 'diffusive' regime. Generally this regime exists during normal ion incidence and high substrate temperatures. In the 'diffusive' regime, diffusion proceeds at a rapid rate compared to the rate at which ions impinge the surface. The result is that the orientation of the nanostructures, usually mounds

or ripples, is regulated by the structure of the surface unit cell. Namely, the step direction generally is situated along the thermodynamically advantageous orientation.

Alternately, a set of conditions exist in which the bombardment of ions is the controlling factor for the surface morphology. The environment in which the surface patterns are determined by the corrosive properties of ion bombardment is called the 'erosive' regime. The 'erosive' sputtering regime is where surface nanostructures are forced to be parallel to the ion beam orientation. These conditions are achieved at grazing-incidence sputtering angles and low substrate temperatures, where thermally activated diffusion processes are inhibited.

Figure 2.4 shows the transition between the diffusive and erosive regimes on account of the approach angle of incoming ions. A Cu (110) sample is exposed to an ion beam of increasing polar scattering angle, while holding the other parameters, such as the ion flux, ion energy, and substrate temperature, fixed. It can be seen from the results that in the range of $\theta = 55^\circ - 65^\circ$ there appears to be a transition in the direction of the ripple orientation, due to competition between diffusion, which tends to drive the nanostructures along $< 001 >$, and ion erosion, which in this case is in the $< 0\bar{1}0 >$ direction. It can be seen that a small increase in the ion angle to 70° produces a clear structural alignment characteristic of the 'erosive' regime.

Figure 2.5 demonstrates that when sputtering in the erosive regime, with the fixed conditions T=180 K and $\theta = 70^\circ$, the formation of surface structures does not depend on the crystal type, symmetry, or orientation. Independent of these material parameters, a comparable ripple wavelength of about 9 nm is obtained under similar sputtering conditions. Comparing 2.5a, where Ne^+ ions were used, to 2.5b and 2.5c, which were sputtered with Ar^+, the ion type does not modify the wavelength of the ripples. It can also be seen that the ion type has no bearing on the wavelength of the ripples, in comparing Ag(001) sputtered with Ne^+ ions with Cu(110) and Ag(110) sputtered with Ar^+ ions.

Further demonstration of the erosive regime is shown in Figure 2.6, where a Cu(110) substrate is exposed to an ion beam in an erosive environment. As the ion-beam alignment switches from $< 1\bar{1}0 >$ to $< 001 >$ the orientation of the ripples also change direction,

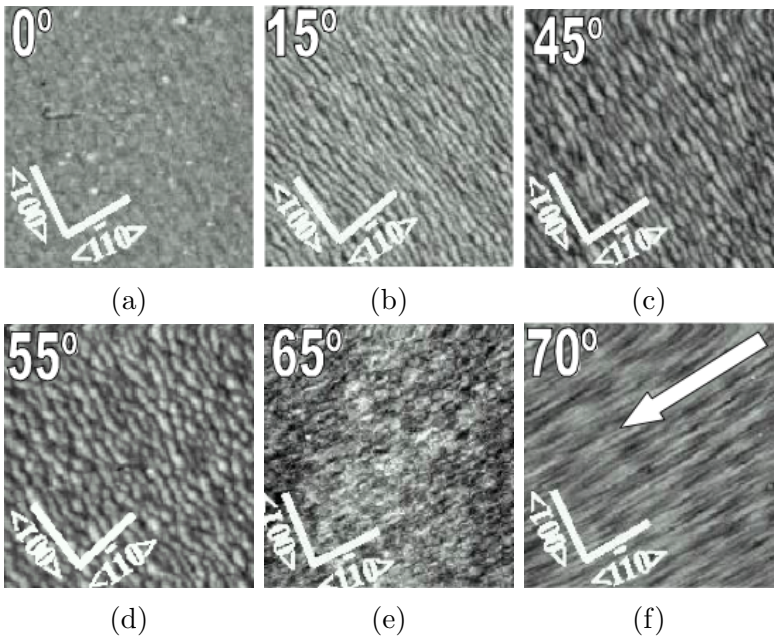

(a) (b) (c)

(d) (e) (f)

Figure 2.4: The role of ion incidence on the transition from the diffusive to the erosive sputtering regime for Cu(110)[56]. The white arrow shows the ion-beam direction. Image size 400x400 nm^2.

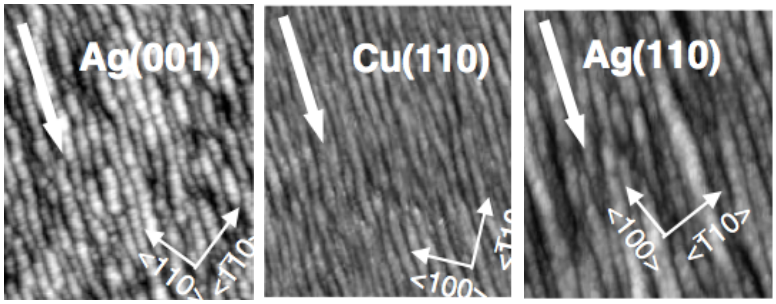

(a) (b) (c)

Figure 2.5: Sputtering in the erosive regime. (T = 180 K, $\theta = 70$) of different substrates. (a) Ag(001), Ne^+ ions, (b) Cu(110), Ar^+ ions, (c) Ag(110), Ar^+ ions, Image size: 180x180 nm^2.

while the surface morphology remains effectively unchanged, as the ripple wavelength and roughness are comparable for all cases of ion beam direction. This means that under erosive sputtering conditions, ripple formation may occur along thermodynamically unfavored directions.

At lower temperatures, when conditions may be classified as being in the erosive regime,

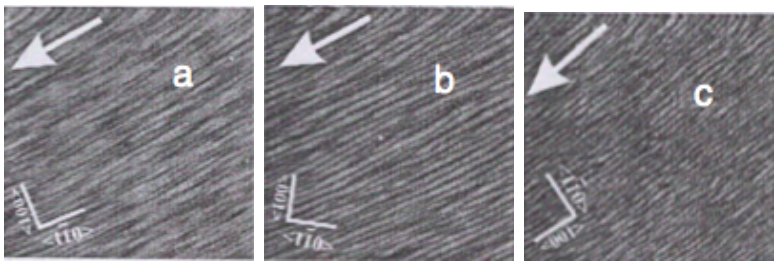

(a) (b) (c)

Figure 2.6: Grazing-incidence sputtering of Cu(110) in the erosive regime parametric in the azimuthal orientation of the ion beam[56]. Independently of the crystal orientation, the ripples always develop along the ion-beam direction. T=180 K.

ripple formation is correlated with ion-beam orientation. At high temperatures, the diffusivity of the defects produced by the impinging ions is so high that the surface morphology is solely dictated by temperature-induced diffusion. Figure 2.7 demonstrates the transition from the erosive regime to the diffusive regime on the morphology of Ag(001) as the substrate temperature is increased. Most sputtering parameters, such as beam energy, ion flux, and sputtering time are fixed, as well as the approach angle of $\theta = 70°$. At the very lowest temperature (2.7a) there appears to be little coherence in the formation of surface features. This indicates that even in the 'erosive' regime at very low temperatures where the diffusion processes are suspended, the lack of defect mobility prevents any correlation between adatom and vacancy clusters, thereby preventing structure formation.

At T=180 K (2.7b) and T=250 K (2.7c) ripples appear to be elongated and directed parallel to the ion beam. The ripple wavelength remains constant through this temperature range. At T=300 K (2.7d) the surface morphology appears to take on significant changes, as the enhanced mobility of the vacancy clusters causes them to merge and control the surface feature formation. At T=350 K (2.7e), it is clear that the features have been aligned along the energetically favored orientation, $< 1\bar{1}0 >$. The direction of the ion beam has no bearing on the morphological orientation under these diffusive conditions. In other words, the defect diffusivity is so high that on the timescale of successive ion impacts, the surface morphology is completely determined by the thermodynamic conditions[56].

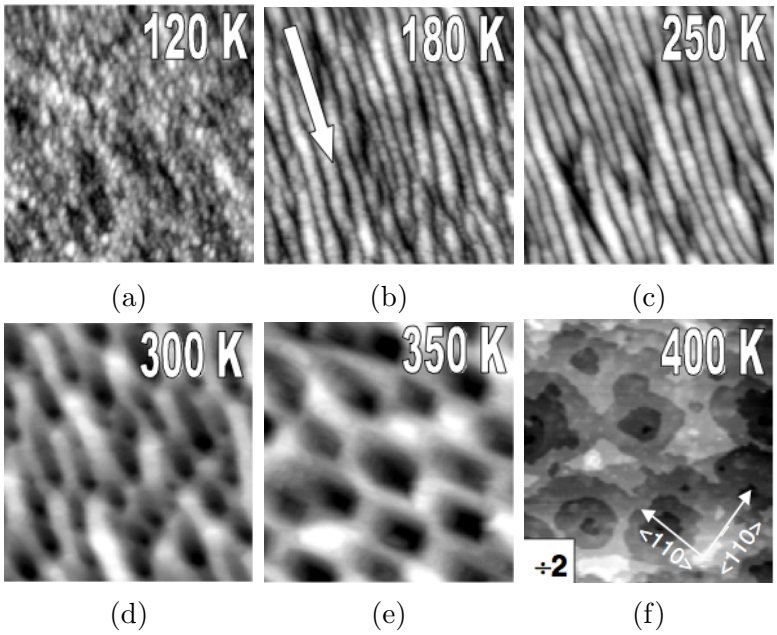

Figure 2.7: The influence of surface temperature in the transition from the erosive to the diffusive sputtering regime for Ag(001)[56]. Ne^+ ions, θ=70, T=400 K. Image size 180x180 nm^2.

2.2 Non-uniform Erosion

Ion bombardment has produced clear effects on material boundaries, in which the physical process of material ablation results in non-uniform surface erosion. Various experimental studies have been performed to examine the effects of plasma exposure on different materials. Additionally, the damage found in plasma-exposed surfaces used in space electric propulsion devices provides a view of the type of erosion caused by ion bombardment. The following sections outline experimental studies that have provided insight into the erosive behavior of ion-bombarded materials.

2.2.1 Surface Roughening

While energetic ions have been used as an independent source to shape the material surface and drive it to self-organize in nano-patterns, the other facet of PMI, namely the reverse influence of surface features on the rate of sputtering has also received some attention.

Thus, the influence of surface roughness on the sputtering rate has been another explored by a number of investigators. Sputtering yield, as the ratio of ejected atoms from the surface to incident ions, has been recently shown to be dependent on the surface nano- and micro-structure [20]. Surface atoms that receive sufficient energy from the ion collision cascade to exceed the binding energy will be removed, and will either escape or interact with an adjacent surface feature. In the latter case, the ejected atom may have a chance to be deposited on a nearby surface feature, and become part of the evolving surface itself. Thus, the surface structure is a dynamically evolving system, where atoms can be removed or deposited in a way that depend on its evolution history. Such geometric re-trapping of atoms offers an opportunity to design sputter-resistant surfaces that have self-healing properties.

The relationship between the surface structure and the rate of sputtering erosion has been experimentally explored. Rosenberg and Wehner first examined the influence of surface roughness on a material's sputtering yield. They compared the sputtering yield of a smooth nickel rod bombarded by Ar^+ ions from 70 to 600 eV to that of a threaded rod with a pitch of 0.45 mm[48]. The experiment showed that surface roughness decreases the measured sputtering yield as a result of increased geometric trapping of sputtered atoms. This study also showed that the effect is more pronounced at lower ion energies, when there is a more oblique distribution of sputtered material and the energy of ejected atoms is too low to induce secondary sputtering. Huerta et al.[27] used a view factor model to examine the sputter deposition behavior observed by Rosenberg and Wehner. Their model found significant decreases in net sputtering yield for surface pitch angles beyond approximately 45°, due to forward-biased sputtering that favors deposition of sputterants into surrounding surfaces. Ziegler et. al. used Chemical Vapor Deposition (CVD) to cover tungsten surfaces with tungsten whiskers, which were up to 80 μm high. They found that the whiskers dramatically reduced the sputtering coefficient for various ion energies, using 2-3 keV He^+ ions to a dose of 2.8×10^{23} m^{-2}[67]. CVD has also been used by Hirooka et. al. to produce textured molybdenum surfaces characterized by dome-like and faceted features on the order of 1 μm in diameter. The textured surfaces showed little damage compared to a polished sample,

each under 40 keV He^+ ion irradiation dose of 3×10^{22} m^{-2}[25]. This result was attributed to the fact that surface features cause an uneven depth distribution of implanted helium concentration, preventing the formation of bubbles that lead to blistering. Exposure of beryllium surfaces to 1000 eV H^+ ions has shown to produce high-angle, closely packed nano-cones at irradiation doses near 7.3×10^{21} m^{-2}[40]. As the cones develop, the sputtering yield of the surface was found to be reduced by 30-40%. These types of investigations have provided a context for the research presented here by establishing a basis for the effect of surface roughness and texturing on a material's sputtering yield. We aim to quantify the relationship between *surface evolution* and the sputtering yield of surfaces with purposefully-designed surface architecture. The current research extends recent findings[20] that nano- and micro-architectures result in reduced sputtering yield, with a focus on the transient nature of *both* surface structure and sputtering yield.

2.2.2 Erosion Patterns in Hall thrusters

The lifetime of Hall thrusters is generally limited by the insulator rings, which cover the magnetic coils that generate the magnetic field. These insulator rings are typically made of boron nitride (BN), and experience degradation resulting from ion bombardment. Wear tests have exhibited groove formations resulting from erosion of the inner and outer BN insulator rings[13], similar to the previously reviewed ripple formations seen on ion-exposed surfaces, but at a much larger scale ($\sim 10^{-3}$ m). This phenomenon is shown in Figure 2.8a.

Peterson, et. al.[45] studied the performance of Hall thrusters using krypton as the propellant. The tests were performed in a vacuum facility at NASA Glenn Research Center. A laser profilometry system was used to measure the wear experienced by the Hall thruster channels, in which the interaction of the laser with the material surfaced was imaged using a charge-coupled device (CCD) camera. The wear profiles of the inner and outer walls of the thruster demonstrated wear beginning further down from the outward face of the thruster. The authors point out that the wear on both boundaries begins at a location that corresponds to where the radial magnetic field is approximately 80% of its maximum. The

applied potential causes the ions to gain energy as they travel further downstream from the beginning of the ionized region.

In conventional Hall thrusters, the lifetime is defined by when the discharge plasma completely erodes the wall material of the insulator rings, however with the modern development of magnetic shielding, channel wall erosion is no longer a problem[26]. With magnetic shielding, pole pieces provide a magnetic field that directs ions out of the discharge chamber without interacting with the insulator ring material. Performance testing has shown that wear is prevalent on the surface of the magnetic pole pieces that generate the shielding field[22]. Figure 2.8b shows the surface of an inner pole piece, located inside the inner ring, after a 150-hour wear test. The pole piece appears to have a textured appearance, indicating the likely contributions of both erosion and deposition of the material. With the introduction of magnetic shielding, the failure mechanism is now the erosion of pole pieces that generate the magnetic field.

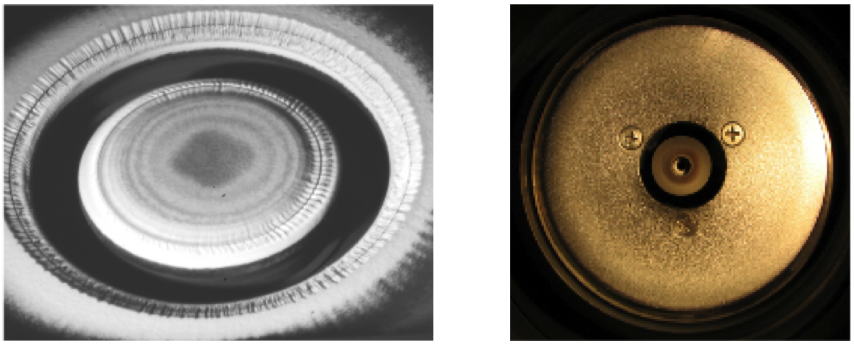

(a) (b)

Figure 2.8: (a) Ripple wear pattern in BN insulator rings on an unshielded BPT-4000 Hall thruster after 10,400 hours of operation[13]. (b) Photograph of an inner pole piece after 150 hours of exposure, showing surface texturing[22].

2.2.3 Erosion Patterns in Ion thrusters

Damage experienced by ion thruster acceleration grids is commonly characterized as the development of "pits" and "grooves" as back-streamed ions bombard the surface of the grid, as well as widening of the screen apertures[23]. Polk et. al.[46] performed an 8200 hour test

on a xenon-operated NSTAR ion thruster to observe the damage characteristics found in the various components. Figure 2.9 shows the "pit and groove" patterning that occurs on the face of the accelerator grid through thruster operation. Additionally, the figure shows carbon deposition around the apertures, attributed to the back-sputtering of carbon from the beam target back onto the engine.

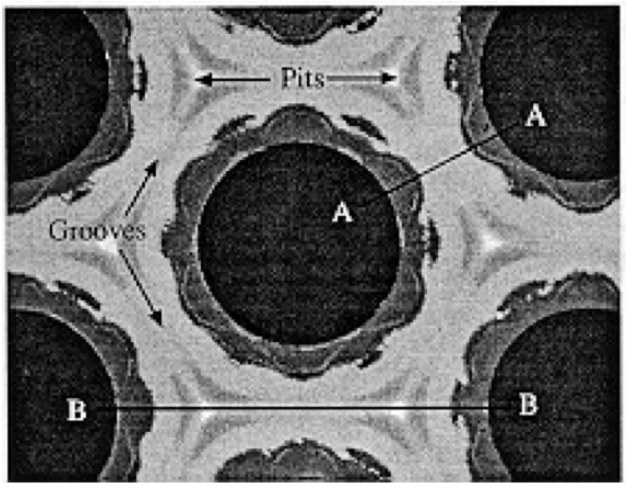

Figure 2.9: Pitting and grooving shown on the face of the accelerator grid after exposure. Apertures are ∼1.3 mm in diameter.[46]

A further wear site for ion thrusters is the orifice of the neutralizer cathode, which experiences widening from ion bombardment. Experiments have shown that the downstream end of the orifice exhibits a 70% increase in diameter after implementing thruster operating conditions[46]. This type of wear can have a significant effect on thruster performance after prolonged use.

CHAPTER 3

Experimental Techniques and Methods

A variety of techniques are used to understand the erosion of surface structures subjected to plasma bombardment. We employ a Chemical Vapor Deposition (CVD) process to produce refractory metal surfaces possessing unique surface geometries of different types, which are then exposed to plasma conditions to observe changes in the structures. These changes are the result of erosion due to lost material, as well as deposition of ablated surface atoms onto adjacent structures. A quartz crystal microbalance (QCM) is used to provide quantitative measurements of the sputtering rate at different points in the fluence exposure, which can then be converted to yield measurements.

3.1 Plasma interactions (Pi) Facility

The UCLA Plasma interactions (Pi) facility is operated by the Wirz Research Group, and designed for the purpose of investigating the interactions between plasma and materials under conditions that replicate the extreme environments experienced by electric propulsion and pulsed power devices. The extent of material samples examined using this facility has a wide potential for exploration, as a variety of materials and surface geometries may be considered. In particular, the application of this research focused on studying refractory metals such as molybdenum and rhenium, in order to observe the damage properties of these material surfaces. Table 3.1 displays the plasma characteristics for the experiments performed in Pi, determined using electrostatic probes in the plasma profile.

The facility (Figure 3.1) uses a hollow cathode to generate a plasma that is confined by

Table 3.1: Plasma profile characteristics

Parameter	Range
Plasma density	$\leq 1 \times 10^{18}$ m^{-3}
Electron temperature	2 to 8 eV
Ion energy	10 to 300 eV
Ion flux to target	10^{19} to 10^{21} m^{-2}s^{-1}

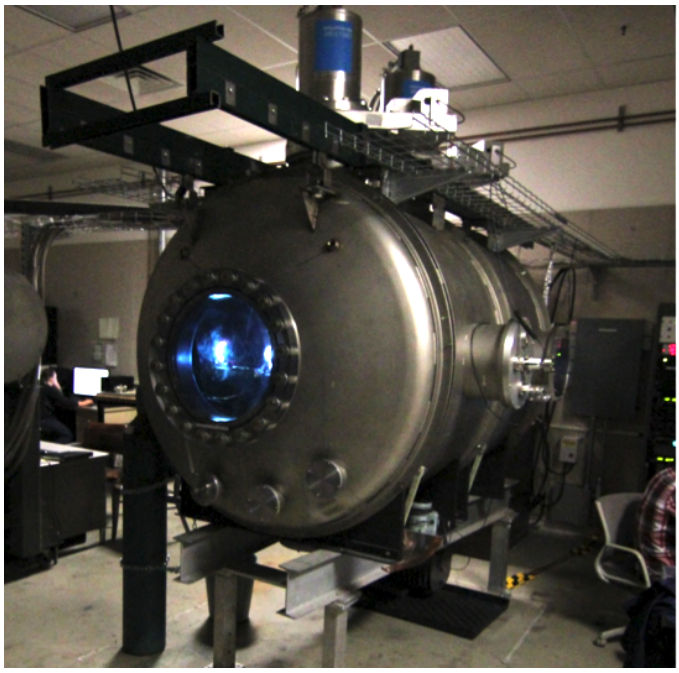

Figure 3.1: The Pi facility in operation at UCLA. Photo by Richard Wirz.

a series of solenoidal magnets. The plasma terminates approximately 2 m downstream of the cathode on a negatively biased material sample at a spot size of approximately 1 cm diameter. For the result reported herein, an argon plasma was used. The target surface can be differentially biased to provide normally incident ion bombardment at a desired ion energy. Matlock et al. present a detailed description of the Pi facility and the plasma operating conditions in references [38] and [35].

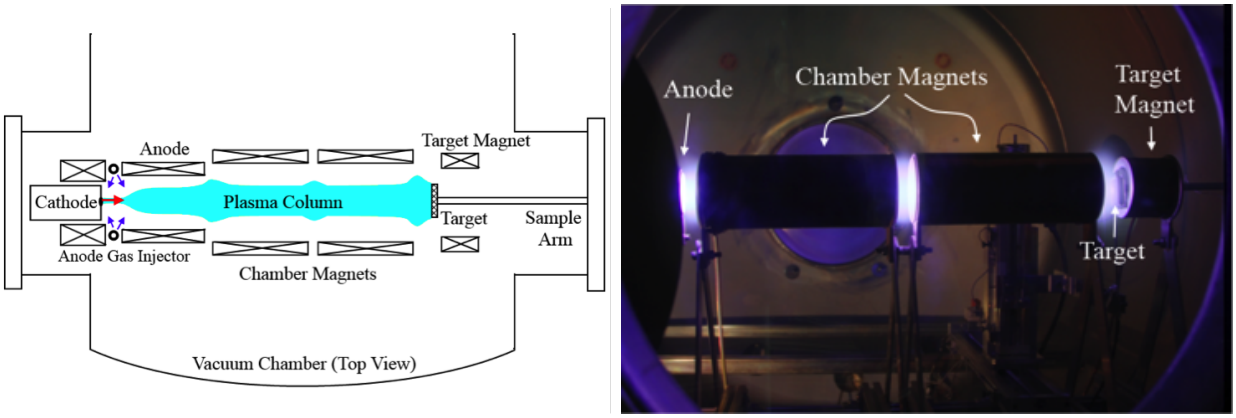

(a) (b)

Figure 3.2: (a) Schematic of the Pi facility (top view) with cathode flow indicated by red arrow, anode flow indicated by blue arrows. (b) Pi facility in operation, equipment components labeled. Images from [38].

3.2 Diagnostics and characterization

A variety of characterization techniques have been employed to further understand the evolution of material surfaces of different types. Scanning electron microscopy (SEM), energy dispersive spectroscopy (EDS), surface profilometry, and quartz crystal microbalance (QCM) measurements offer insight into the response of both micro-architectured and planar refractory metal samples to ion bombardment at different parameter levels. Specifically, these techniques can offer information on the morphological transformations, as well as the chemical and mechanical response of the surfaces being examined.

3.2.1 Scanning electron microscopy (SEM) imaging

SEM uses a focused beam of energized electrons that scans the surface of a material sample and interacts with the surface to provide various signals that may be used to produce an image[4]. This technique offers primarily qualitative information that offers important fundamental tracking of surface features on the material samples. The evolution of the features was observed over multiple exposures using this technique. In particular, SEM provides insight into the damage response of surfaces including cracking, melting, degradation,

etc. Additionally, it allows for the tracking of surface features, including the formation and evolution of structures due to sputter deposition. Features that are relevant include the nucleation of redeposited material ablated from ion impact. Surface mobility effects play a role in structure evolution, as impurities cause nucleation sites, and relaxation effects are prevalent due to temperature-induced surface diffusion. SEM offers an effective avenue for observing these phenomena. Examples of SEM images of micro-architectured samples are shown in Figure 3.3.

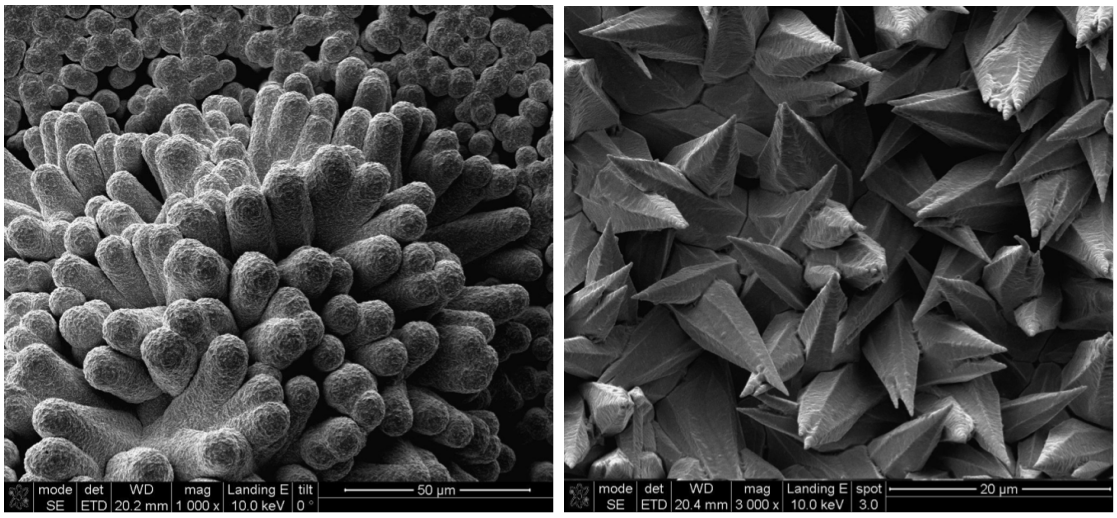

(a) (b)

Figure 3.3: W on dendritic Re, 1000x (a) Mo on black Re, 3000x (b). Images by D. Rivera

3.2.2 Energy dispersive x-ray spectroscopy (EDS)

EDS offers elemental analysis of the surface composition, which is useful for monitoring the presence of contaminants or oxidation. This technique uses a beam of electrons focused on a material sample to excite the emission of a characteristic X-rays corresponding to the elemental makeup of the surface. Every element has a unique peak energies in its X-ray spectrum, which allows the elements present to be identified and quantified[51]. Analysis was performed on the samples before and after each exposure. The purpose of tracking the chemical composition is to more accurately account for the emergence of peripheral elements on the sample as a result of plasma exposure. In the case of multi-composition samples

in which a dendritic material is coated with another, it is important to be aware of which elements are appearing in the spectrum, as erosion causes the underlying material to become more apparent. Additionally, it allows for the monitoring of impurities such as oxides and carbides that may be present from the manufacturing process or through exposure.

3.2.3 Digital profilometry

A Keyence VHX-1000 digital microscope was used to provide surface profilometry of the micro-architectured samples throughout testing. This system has the capability of rendering 3-dimensional images of the surface profile, as shown in Figure 3.4. The microscope operates by scanning in the vertical direction using a high magnification lens, which provides 3D depth information using the amount of out-of-focus blurring[1]. A 3-dimensional image can be resolved using an algorithm that tracks the focused planes of the surface. In addition, the system can provide surface height mapping to allow for the determination of quantitative roughness and profile measurements. For this research, roughness measurements were useful to track the effect of plasma exposure on micro-architectured samples over time.

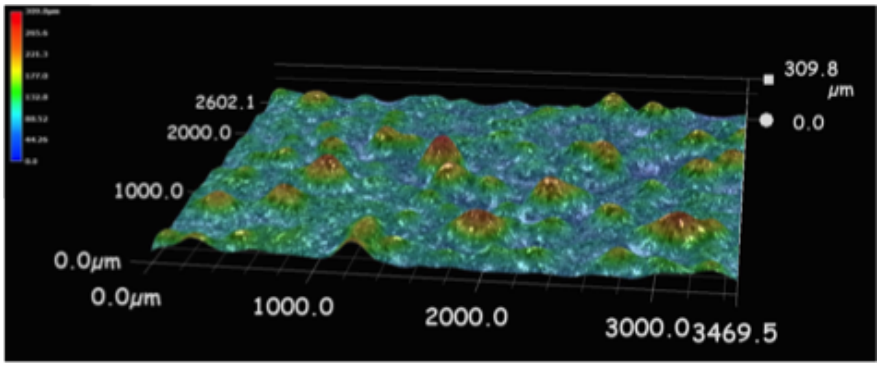

Figure 3.4: Surface height profile rendered from VHX-1000 digital microscope readings.

3.2.4 Quartz crystal microbalance (QCM)

The Pi facility is equipped with multiple diagnostics for measuring the properties of the plasma and sputtered particles. An extensive description of the Pi facility diagnostics rele-

vant to this study is provided in Reference [34], so only a brief description of the QCM is given here.

The QCM (setup shown in Figure 3.5) provides an output of the time-resolved sputtering rate of the target sample. As incoming sputtered atoms get deposited on the surface of the sensor, the resonance frequency of the piezoelectric quartz crystal sensor decreases. In turn, this correlates with the collected mass from the target sample, and hence the number of sputtered atoms from the target area[47]. Based on this frequency shift, the differential sputtering rate at a given location can be measured over a period of collection time. Polar measurements are obtained by mounting the QCM to a rotary stage with a moment arm of 25.4 ± 0.2 cm. The sputtering distribution is assumed to be axisymmetric because of the cylindrical nature of the incident plasma column, which allows the differential sputtering rate, measured in [ng cm$^{-2}s^{-1}$], to be considered a function of the polar angle only. To perform a polar scan, the QCM is rotated from $\alpha = 90°$ to $\alpha = 30°$ at 5° increments, pausing for a 1-minute duration at each angle to provide sufficient collection time, and thus reduce measurement uncertainty.

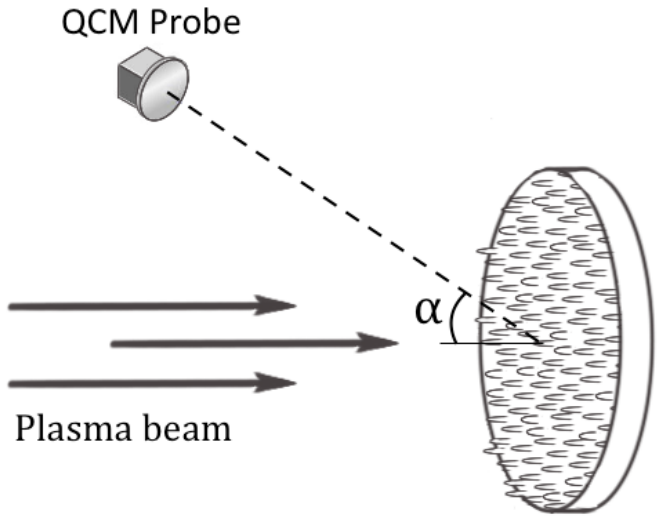

Figure 3.5: QCM Coordinate System

The differential sputtering rate provided by the QCM can be used to obtain a differential sputtering yield, which is then integrated over the hemisphere in front of the target to obtain

the total sputtering yield. This value is averaged over the QCM scan period. Since the time-scale of transient erosion is much longer than the QCM scan duration ($\tau_{\text{erosion}} \gg \tau_{\text{QCM}}$), QCM measurements will be shown to have good accuracy in resolving the transient sputtering yield.

3.3 Micro-architectured Surfaces

Micro-architectured material samples used in this research are produced by Ultramet Inc. using a CVD process using a variety of refractory metals. The details of these materials samples are outlined by Ghoniem et. al.[20]. The CVD fabrication method allows for high purity levels and controlled material parameters, including composition, density, and coating thickness. By controlling the pressure and temperature conditions of the CVD process, refractory metal dendrites, or nano-rods, may be grown from a substrate surface. The size parameters of these dendrites can be controlled to produce features of variable length, diameter, surface density, and vertical taper.

Dendritic rhenium is the most extensively produced sample type by Ultramet, as it is used widely in aerospace and semiconductor applications, however any other refractory metal can be deposited by CVD. Rhenium deposited onto a substrates results in the formation of dendrites with hexagonal symmetry in the cross-section. The CVD conditions allow for these to be grown uniformly or with a taper to form spear-like structures. Rhenium dendrites can then be used as scaffolds and coated with tungsten or molybdenum to produce layered nano-rods. These nano-rods can vary in diameter from 100-1000 nm, and possess aspect ratios of 5-20. Molybdenum is another material that has been used to create unique samples with fractal geometry, which have been used in this study to examine the transient yield properties of textured materials.

Textured material surfaces may be classified into three main categories, which are displayed in Figure 3.6.

1. *Reticulated structures (metallic foams)*

   Metallic foams are composed of a network of interconnected ligaments that form a

porous structure. Their surface area-to-volume ratio exceeds 20,000 m^2/m^3, which provides high rigidity to weight ratios and energy-absorbing properties[50]. The mechanical and thermal properties of foams can be tuned according to cell size and shape, offering a variety of possibilities depending on the application.

2. *Fractal structures*

   Certain surface texturing techniques produce self-similar structures of a fractal nature. These surfaces are usually characterized by larger features with a number of folds that introduce complexity to the plasma interaction process. The high degree of surface roughness causes ablated material to interact with adjacent structures and cause either secondary sputtering or deposition, depending on the particle energy.

3. *Dendritic structures*

   A widely used class of textured materials is described by the collection of fibrous surface structures protruding from the material surface. These structures can vary widely in their size and shape, ranging from needle-like nano-rods to wider pillars. In addition, the tips of these structures may possess prismatic caps or spear-like geometries that significantly determine their behavior when exposed to plasma conditions. Presence of dendritic structures typically results in geometric re-trapping of material, as well as enhanced thermal properties due to enhanced heat-transfer capabilities.

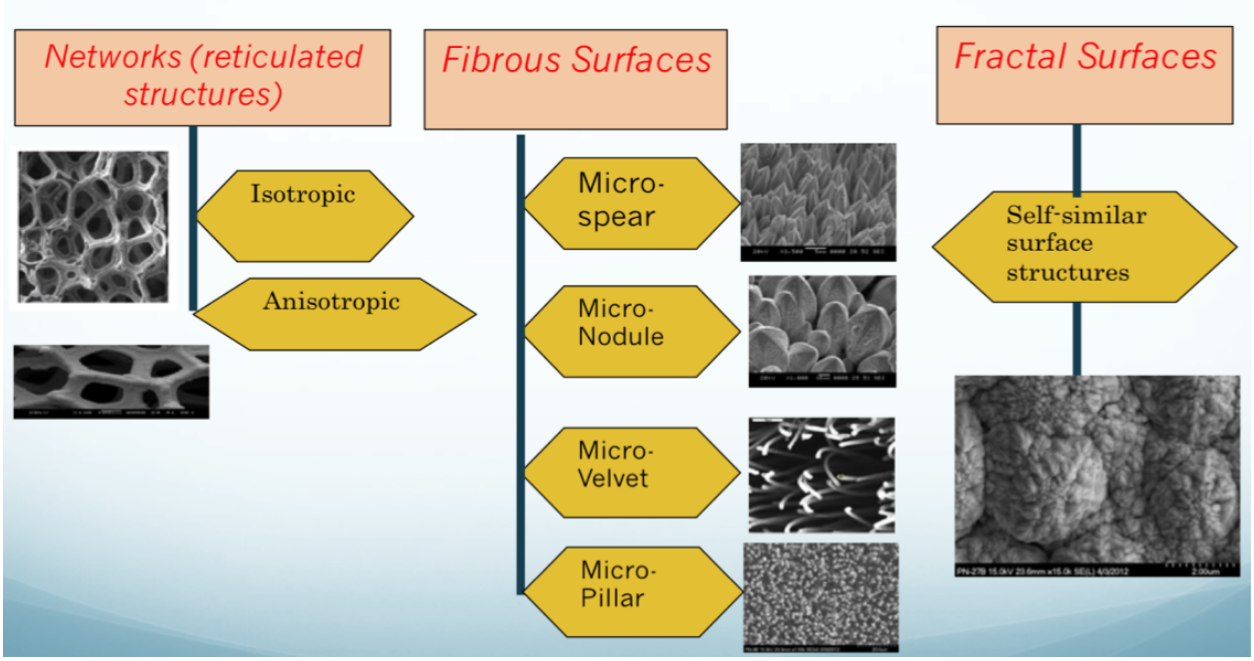

Figure 3.6: Classes of micro-architectured materials. Various categories of each class are pictured to show the diverse types of engineered material surfaces. Image from the MATRIX Laboratory website.

CHAPTER 4

Experimental results

The purpose of the experimental study was to examine the behavior of nano- and micro-architectured surfaces relative to that of planar samples. Various material samples were examined, and each underwent a variety of tests and characterization techniques to understand the physical mechanisms that determine surface evolution in plasma-facing materials. The following sections outline the results from this experimental study, beginning with low-fluence plasma exposures, leading to later experiments monitoring sputter yield.

4.1 Low-fluence tests

Testing began with low-fluence exposures on dual-composition textured samples to observe the early-stage plasma effects on the material surfaces. Two different samples, designated as "A" and "B", each possessed clearly distinct surface structures and were exposed in the Pi facility to incremented levels of plasma fluence. Sample A is heavy Mo over black Re, and Sample B is Heavy Mo over dendritic Re. Figure 4.1 displays SEM images of both of these samples at 1000x magnification prior to exposure. It can be seen that Sample A (Figure 4.1a) exhibits sharp, pyramid-like micro-spear structures protruding in different directions. Alternately, Sample B (Figure 4.1b) is characterized by cylindrical dendrites topped with smooth, uniform prismatic flat caps. The differing architectures are the result of different structures formed through the CVD process used to manufacture the samples.

Both samples were exposed to equal levels of fluence at various increments. Fluence testing began at a very low level, with an initial exposure of $5 \times 10^{17} \mathrm{cm}^{-2}$. The fluence was

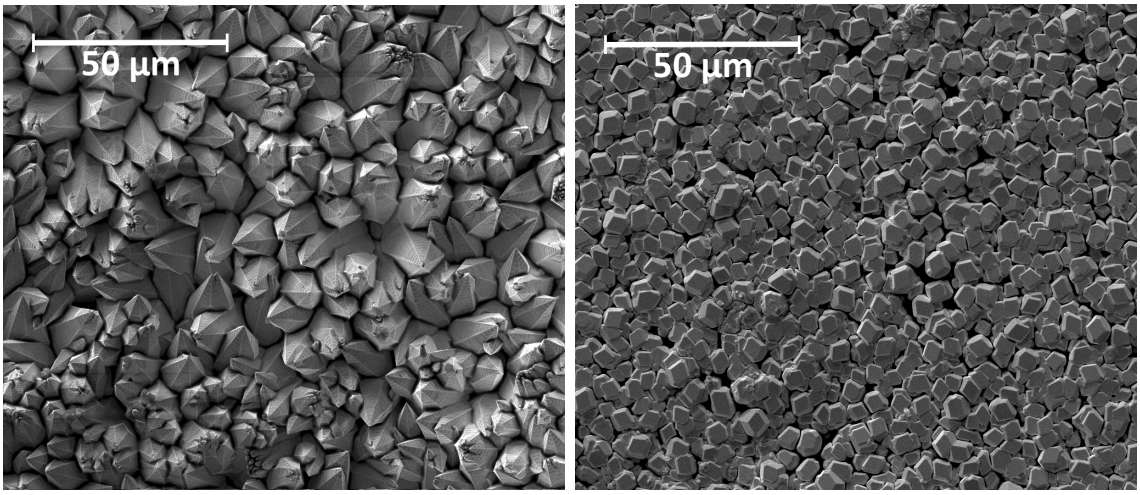

(a) (b)

Figure 4.1: (a) Sample A, 1000x. (b) Sample B, 1000x.

incremented for each successive exposure. Because of the prismatic caps on the dendrites of Sample B, there was little noticeable change in the surface structure at low levels of fluence. The caps provided protection from ion bombardment and displayed little erosion at these lower fluences. Sample A, however, exhibited changes on the surfaces of each of the dendrite facets with the emergence and aggregation of small bump-like structures as the plasma fluence was incremented. Figure 4.2 shows the nucleated structures that formed on the surface of the dendrites. This result phenomenologically demonstrates the growth of nucleated structures as fluence is increased, indicating the presence of deposition processes on the surface of these dendrites. It appears that these formations have nucleated from self-deposition as sputtered material from adjacent structures is deposited onto the dendrite faces. EDS tests on the sample before and after each exposure show the absence of oxidation or other types of deposits.

The development of the dendrite structures was analyzed across the various levels of fluence to quantify the effect of plasma exposure on the observed sputter deposition. The SEM images of the dendrite faces were analyzed using ImageJ processing software to count the number of "islands" that were visible on the surfaces at each fluence level. The results are plotted in Figure 4.3, where the density of the islands is calculated by dividing the number

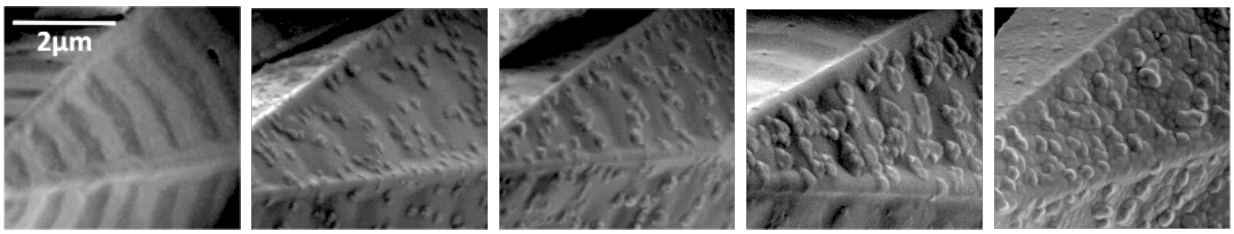

(a) (b) (c) (d) (e)

Figure 4.2: Sample A at 20,000x. (a) Pre-exposure, (b) $5 \times 10^{17}\text{cm}^{-2}$, (c) $1.5 \times 10^{18}\text{cm}^{-2}$, (d) $6.5 \times 10^{18}\text{cm}^{-2}$, (e) $1.15 \times 10^{19}\text{cm}^{-2}$

of islands by the effective area of the image. The results show that the density levels out as the total fluence compounds after an initially rapid increase in the number or islands.

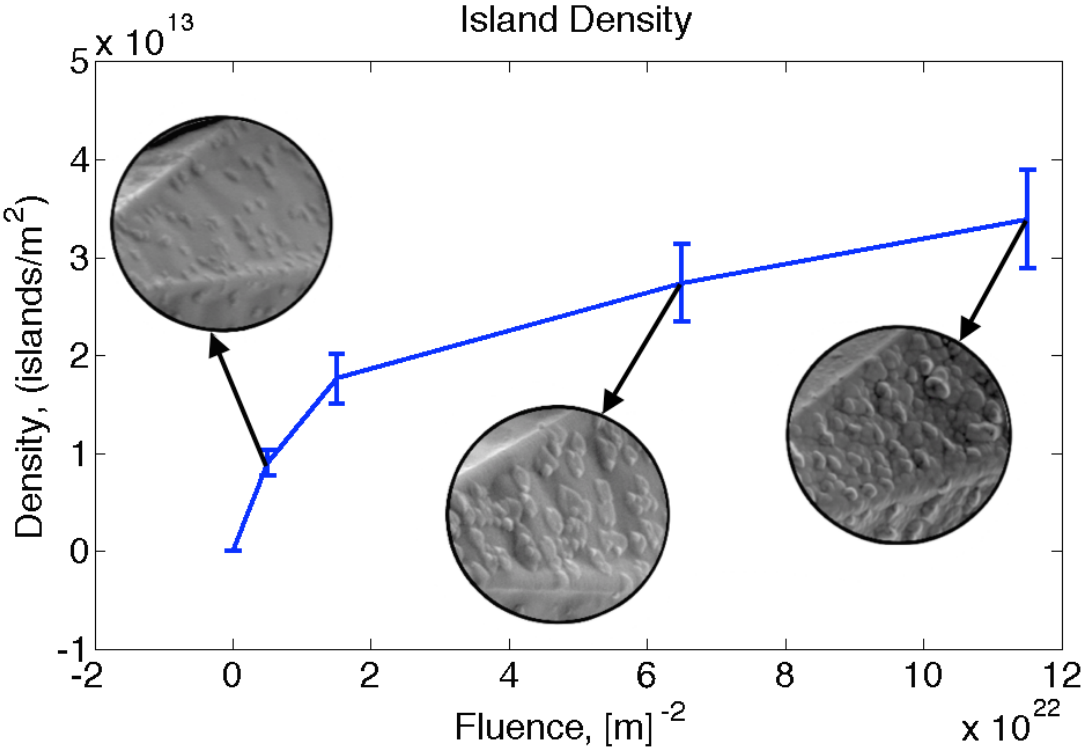

Figure 4.3: Density of island formation on dendrite faces observed over increasing fluence.

Further quantification is displayed in Figure 4.4. ImageJ was used again to measure the average radius of the islands displayed in each image, and the total spacing radius was determined according to the number of islands over the area of the dendrite face. These results were plotted against each other as shown to determine the coalescence point, where

the average island radius equals the spacing radius. At this point, the islands have completely covered the dendrite surfaces. The figure shows that this coalescence occurs at approximately 1×10^{23} m^{-2}. This result corresponds to the images, which show the original dendrite surface completely covered by deposited features after the exposure that exceeds this total fluence level.

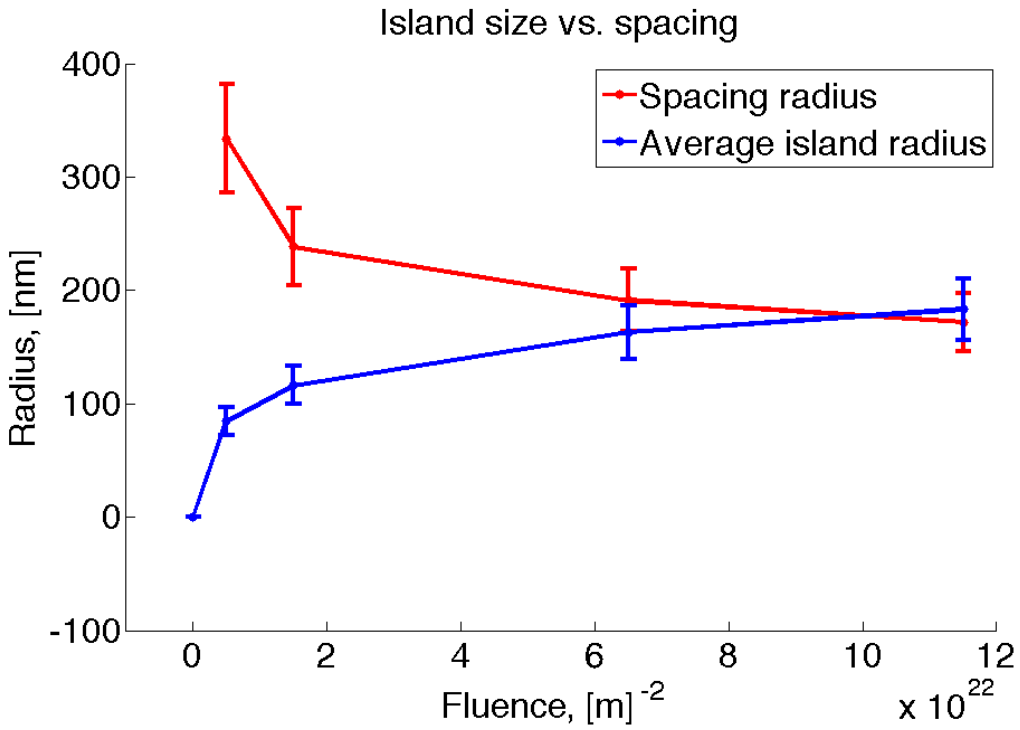

Figure 4.4: Radius of spacing between islands compared to the radius of islands themselves.

Figure 8.2 shows the nucleation sites of the sputter deposited material at various magnifications. What can be seen from these images is the dissimilar distribution of islands among the various faces of the dendrites. The non-uniformity of patterns between the faces indicates the geometrically dependent nature of the source of these islands, being line-of-sight sputter deposition. Additionally, 8.2c shows the detail of the formed structures at a higher magnification, on a face that experienced the highest amount of deposition.

Identifying the source of deposition is important in understanding the behavior of surface patterning that results from plasma exposure. Figure 4.6 illustrates the deposition processes that determine the source of the deposited material, according to the relevant conditions.

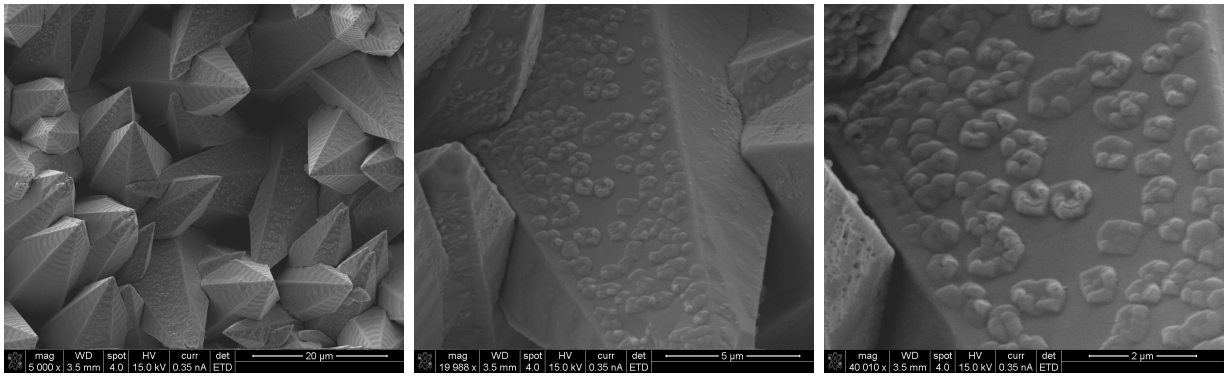

(a) (b) (c)

Figure 4.5: Sample A after exposure to a fluence of $6.5 \times 10^{18}\text{cm}^{-2}$. (a) 5,000x, (b) 20,000x, (c) 40,000x

The first process shown is characterized as "ballistic deposition", and results from line-of-sight trapping of sputtered atoms. In this case, ablated material sputtered from one structure is deposited onto adjacent structures. This is especially relevant in the case of micro-architectured materials, and it is believed that the formation of the islands observed on the surface of the dendrites of Sample A may be attributed to this process. Alternatively, deposition of material may be classified as "plasma-mediated redeposition". In this case, ablated material due to plasma exposure reenters the plasma stream, where it is ionized and deposited back onto the material surface. This process typically occurs under high plasma flux conditions. The exposures performed in the Pi facility used a very low ion flux that creates conditions insufficient to experience redeposition.

In consideration of these two deposition processes, it can be asserted that ballistic deposition is generally achieved through material design while redeposition is encountered through device design. The objective of this research is to improve the longevity and resilience of materials used in space electric propulsion, such that the material surfaces have self-healing properties under basic operating conditions. As demonstrated by the low-fluence results of Sample A, micro-architectured materials exhibit geometric trapping of material ablated through plasma exposure, which in turn establishes "self-healing" qualities when focusing on mass retention.

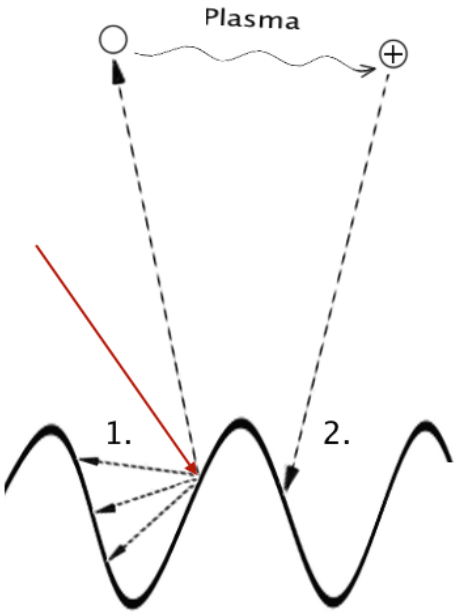

Figure 4.6: Possible deposition processes on the surface of a micro-architectured material. (1) ballistic deposition from sputtering of adjacent surfaces, (2) Plasma-mediated redeposition.

4.2 Surface structure changes from higher fluence exposure

After the initial low-fluence tests, higher fluence levels were given to both Samples A and B in order to observe how the larger-scale structures react at higher doses of ion bombardment. Figure 4.7 shows the changes in a particular formation found on Sample A over several exposures, where certain points on the feature have been identified with numbers to allow for comparison. This location on the surface of Sample A is a larger cluster of spears that likely formed at an impurity sight during the CVD process used to manufacture the sample. Examining this formation reveals the result of the deposition observed during the low-fluence tests, but on a larger scale, both in size and fluence. The image in 4.7a shows the cluster after the low-fluence tests, but prior to this higher-level fluence testing. It can be seen that the overall appearance of the cluster is relatively unaffected by the initial round of tests, as the dendrites have maintained a spear-like structure with clear edges. Successive tests show the development of the cluster as it erodes and experiences self-deposition effects. From the first test, it can be seen in 4.7b that the tips of the spears have begun to erode, revealing

the black rhenium core. In addition, the base of the dendrites can be compared to the previous image, 4.7a, to see that swelling has occurred as the perimeter of the structures has grown, and various crevices have filled in with material. Ostensibly, this may be attributed to the geometric re-trapping of sputtered material through line-of-sight deposition. The features continued to develop in this way for successive exposures, as seen in 4.7c-e. EDS measurements show that no contamination or oxidation is contributing to these results.

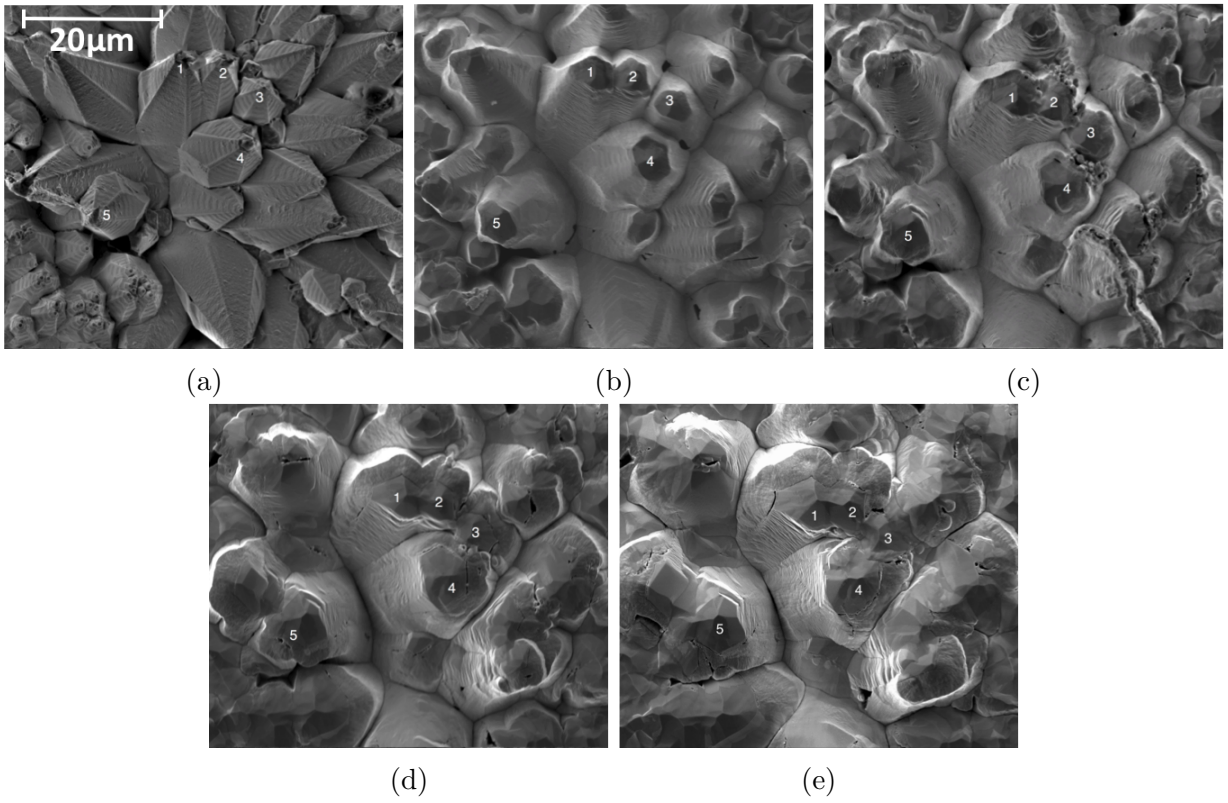

Figure 4.7: Sample A, 1000x (a) Surface after low-fluence tests, 6.8×10^{19} cm^{-2} (b) After first higher-fluence exposure, 2×10^{20} cm^{-2} (c) 2.5×10^{20} cm^{-2} (d) 3.1×10^{20} cm^{-2} (e) 3.6×10^{20} cm^{-2}

The images in Figure 4.7 were analyzed using ImageJ to quantify the growth of the surface features. The software was used to measure the base footprint of each of the spears see in the surface feature across each of the exposures. In addition, the area of the exposed rhenium core at the tip of the dendrites was measured to examine the erosion of the spear tips. Figure 4.8 displays the average growth of the spear footprints and exposed tips, respectively, relative to their original size prior to exposure. It can be seen that the relative increase of

the exposed tips is more rapid than that of the footprints. After the fourth exposure, the footprint areas had grown an average of approximately twice in size, while the area of the exposed rhenium at the tips had grown about three times in size. The error bars indicate the standard deviation among each of the dendrites, which increases as the dendrites expand and the tips of the spears erode.

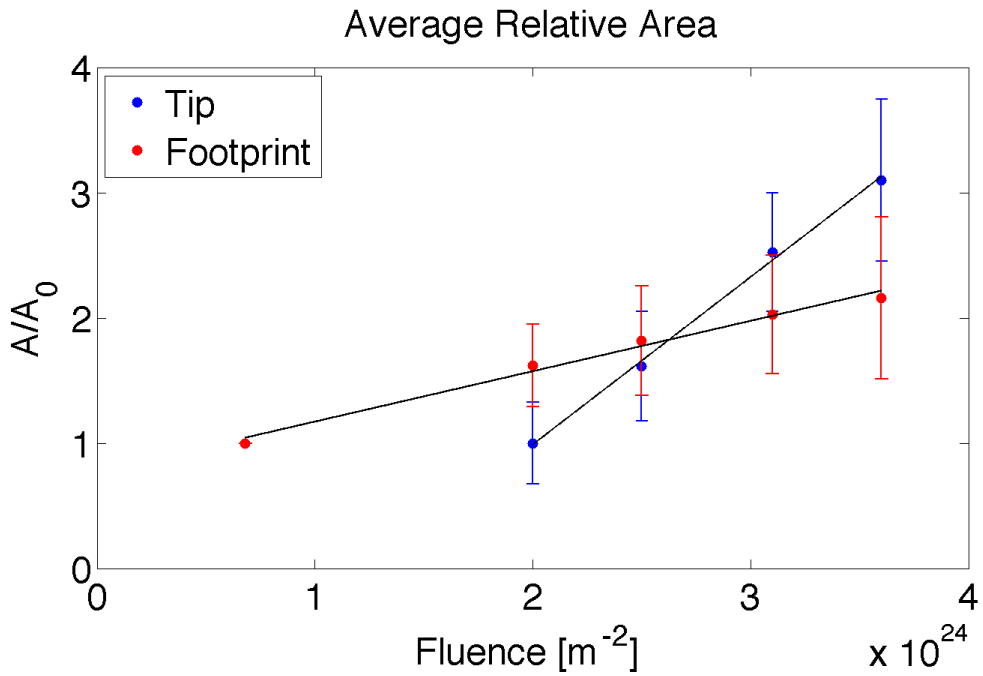

Figure 4.8: Average relative area increase of the spear footprints and exposed Re cores.

The self-healing mechanism is illustrated in Figure 4.9, whereby material is lost at the spear tips and ablated particles are deposited onto the sides of the dendrites. As previously observed at low fluences, the deposited particles form islands. These islands collect and coalesce at higher fluences to create layers of deposited material on the outer surface of the dendrites. The mass loss at the tips of the spears results in a shortening of the dendrite height and a widening of the top surface. The deposited material provided by adjacent faces and the sputtered tips causes the outward growth of the bases of the dendrites. The result is a widened footprint as the base swells.

Sample B has a distinct dendritic geometry from that of Sample A. At various points on the surface, impurities caused the formation of overgrown dendritic clusters. While these

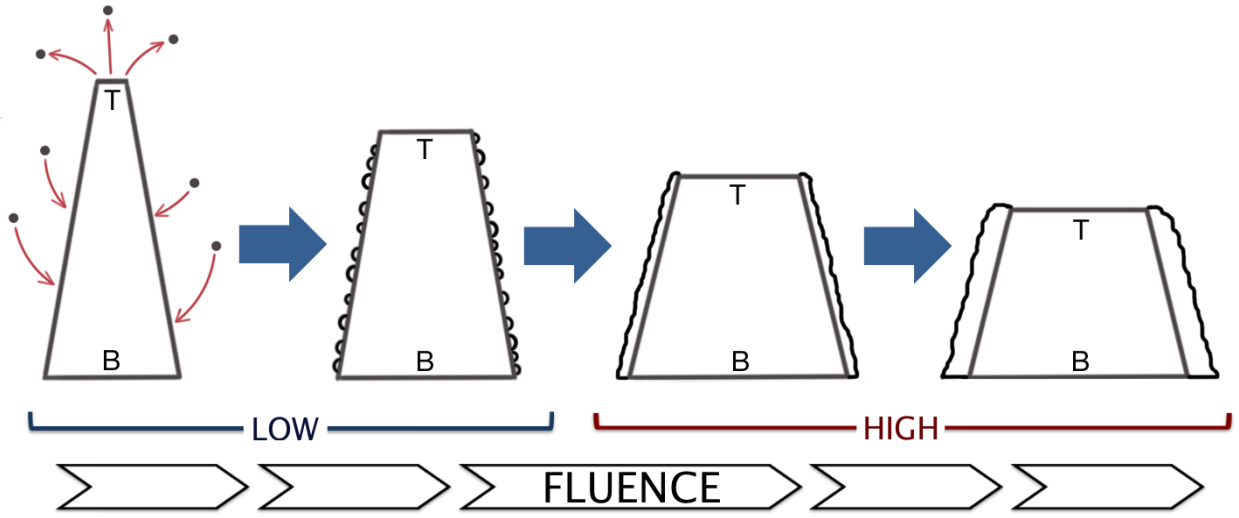

Figure 4.9: Self-healing process observed in Sample A.

protruded formations do not represent the general characteristics of the surface, important insight can be garnered from the effects of ion bombardment on these unique structures. The low-fluence testing produced little change in the surface of Sample B, as the prismatic caps protected the dendrites from experiencing significant wear, however the protruded formations exhibited some slight effects. Figure 4.10 shows the effects of the low-fluence exposure on the dendritic clusters. Figure 4.10a shows a wide image of a cluster protruding from the more uniform surface, while 4.10b displays a magnified view of some cluster dendrites that have remained relatively undamaged from plasma exposure. Figure 4.10c shows a grouping of these protruded dendrites that have experienced damage after exposure to a fluence of $6.5 \times 10^{18}\text{cm}^{-2}$.

The higher-fluence tests performed on Sample B produced results that were similar to those from Sample A. Figure 4.11 shows the development of a surface feature on Sample B at incremented levels of fluence exposure. After the initial low-fluence tests, the structure shown in 4.11a had little variation from its unexposed state. The structure after the initial higher-fluence exposure, seen in 4.11b, again demonstrates the erosion of the dendrite tips, exposing the inner rhenium core. Additionally, comparing the images shows that the dendrite stems have swelled and the spaces between them have filled in. This swelling effect may be due in

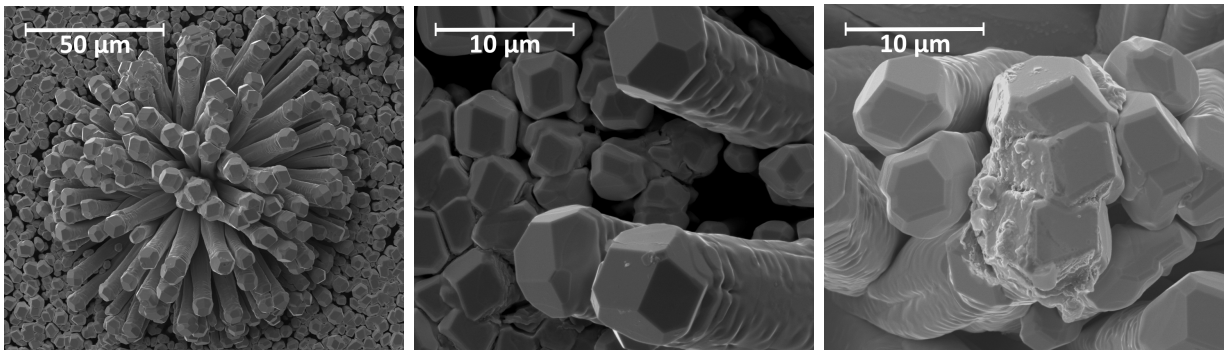

(a) (b) (c)

Figure 4.10: Sample B. (a) Wide shot of cluster at 1000x, (b) Undamaged cluster dendrites at 10,000x, (c) Dendrites that have experienced damage due to exposure at 10,000x

part to the material from the tip of the displayed feature, but is also likely due to deposited material eroded from the caps of the smaller uniform dendrites, which are clearly seen to erode in the images. The development of the surface feature continues to grow outward as the top erodes for successive exposures. Again, EDS confirms the absence of contaminants or oxidation affecting these results.

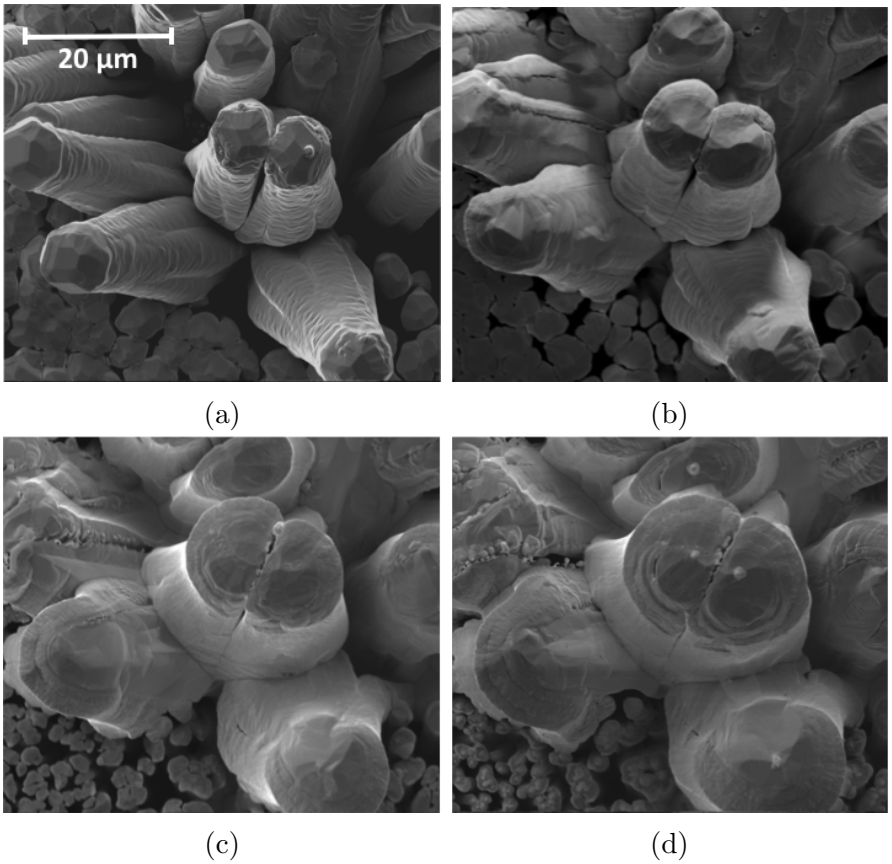

Figure 4.11: Sample B feature development at increasing levels of fluence. (a) 4.2×10^{19} cm^{-2}, (b) 9.2×10^{19} cm^{-2}, (c) 1.4×10^{20} cm^{-2}, (d) 1.9×10^{20} cm^{-2}

4.3 Measurements of Sputter Yield

4.3.1 Review of Planar Mo Measurements

Previous work has produced a range of experimentally determined yield values for the sputtering of planar Mo by Ar^+ at various ion energies[61, 68, 33]. Figure 4.12 shows the yield measurements of previous studies, and includes a curve displaying the empirical equation for sputter yields at normal incidence developed by Yamamura et. al.[65, 39] The test conditions of the present study used Ar plasma at 300 eV, which has shown yields between 0.39 and 0.58 atoms/ion in previous experimental studies. Low ion energies have produced notably indeterminate yield values for planar materials under ion bombardment. Therefore, in exploring the transient nature of sputter yields for nano- and micro-architectured surfaces,

there is no clear steady-state limit at which to expect the yield to level off.

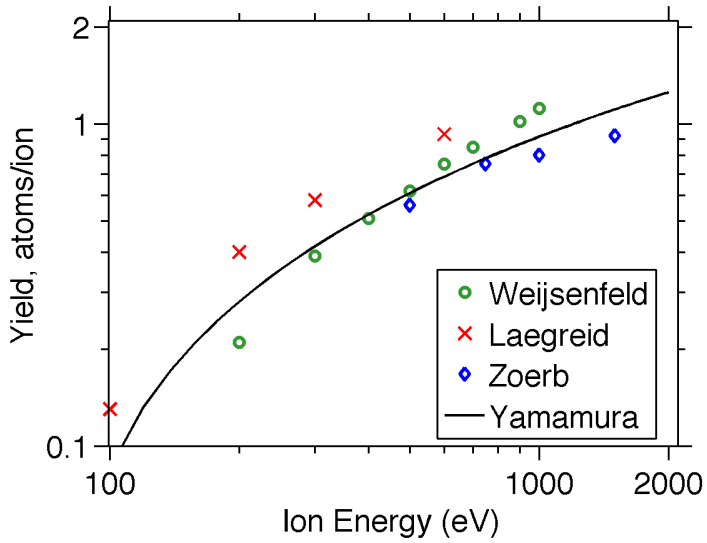

Figure 4.12: Yields for Ar^+ on Mo.

4.3.2 Micro-engineered Mo Samples

Two micro-architectured molybdenum samples, denoted as Samples "C" and "D", were used to measure the sputtering yield over increasing cumulative fluence. The samples were produced by Ultramet on 2-inch diameter disk substrates. The samples possessed similar textures, characterized by course fractal surface clusters, however they varied in the structure density. The first specimen, Sample C, was distinguished by a denser covering of course surface formations that generally ranged from 100 to 300 μm in diameter. The second specimen, Sample D, was covered with similar patterns, but had fewer large structures and a greater amount of rough, flat space between the structures. The morphological differences are seen in Figure 4.13, where the samples have not yet been exposed to plasma.

Because of the Gaussian plasma flux profile, the edges of the plasma-exposed portion of the samples displayed a gradient of erosion. Examining the outer boundaries of the plasma distribution allowed for characterization of the surface morphology at various levels of plasma exposure. Figure 4.14 shows the changes in the surface formations starting outside

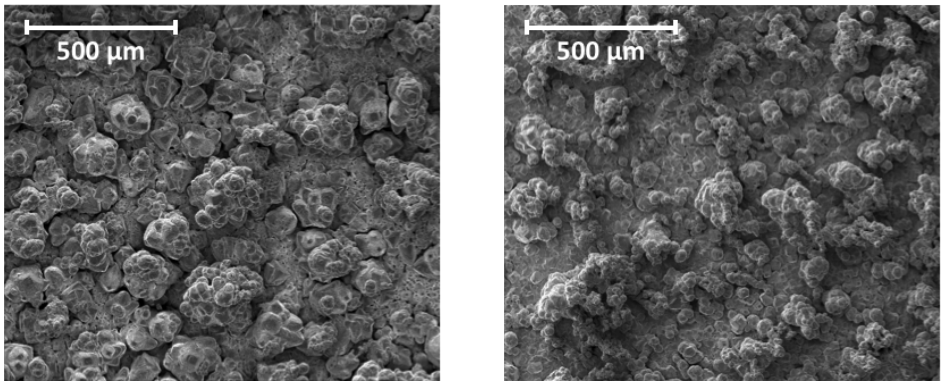

(a) (b)

Figure 4.13: Samples (a) C and (b) D surface morphologies prior to plasma exposure.

the plasma-exposed region and moving inward. Each location moving toward the center experienced a greater dose of fluence throughout the testing period, as the flux was most concentrated at the center. It can be seen that as fluence increases, the surface structures erode and are flattened. It can be noted in 4.14b that the structures appear to have swelled when compared to those in 4.14a, corresponding to the findings of the exposures performed on Samples A and B. The fully-eroded region is pictured in 4.14d, at a location that is close enough to the center that all recognizable surface features have been flattened.

(a) (b) (c) (d)

Figure 4.14: Sample C morphological changes at increasing levels of fluence from (a) to (d). As cumulative fluence increases, surface structures are eroded and flattened.

4.3.3 EDS results

Energy-dispersive X-ray spectroscopy (EDS) was performed on all the samples tested before and after ion irradiation. This data allowed for the presence of contaminants or oxidation to be easily detected. The surface composition data is presented in Table 4.1, which displays the weight percentage composition of the sample surfaces before plasma exposure and after testing was complete. The surface contaminants that were generally detected were carbon and oxygen, which were present on the surface prior to testing as a result of the manufacturing process. It was necessary to track the presence of these elements to assure the absence of oxidation or carbon deposits affecting the development of the surface morphology. It can be seen that in general, both the carbon and oxygen levels were less after exposure than prior to testing. This indicates that no contamination occurred throughout the tests, and the surfaces were actually cleaned of these elements through plasma exposure. A notable observation for Sample B is that post-exposure composition contained a significantly higher presence of rhenium as the outer molybdenum coating was removed during the tests. Figure 4.15 illustrates the EDS spectrum for Sample B. It can be seen that prior to exposure, oxide and carbide levels are present, which are lessened through subsequent plasma exposure. Additionally, the presence of Re in the spectrum becomes apparent as the Mo coating is sputtered away.

4.3.4 QCM results

Sample C was irradiated up to a total cumulative ion fluence of 1.61×10^{26} m^{-2} at an average flux of approximately $2.3 \times 10^{2}1$ $m^{-2}s^{-1}$ using 300 eV Argon plasma. QCM measurements were taken at multiple points throughout the exposure in order to calculate the sputter yield at various levels of fluence. The connection between sputter yield and fluence is attributed to changes in the surface morphology by the erosion and deposition processes clearly observed in previous experiments. It was expected that at early points in the irradiation, ballistic deposition of ablated material would be prevalent by geometric re-trapping of material.

Table 4.1: EDS measurements for surface composition, in weight percentage, of each sample before and after plasma exposure.

Sample No.	Elements	Weight % Pre-exposure	Weight % Post-exposure
Sample A	C	6.65%	2.55%
	O	3.95	0.33
	Re	89.41	97.12
Sample B	C	15.39%	0.52%
	O	10.52	2.45
	Mo	72.11	71.83
	Re	1.98	25.20
Sample C	C	0.0%	0.0%
	O	7.58	1.93
	Mo	92.42	98.07
Sample D	C	0.0%	0.0%
	O	5.43	1.41
	Mo	94.57	98.59

The yield would then be affected as the fluence compounded and the surface features were worn down. Figure 4.16 shows the QCM data taken for Sample C, prior to any bias error adjustments. It can be seen that there exists a transient region where the yield grows as the surface changes. At a certain fluence level, approximately 1.3×10^{26} m^{-2}, the yield value levels off and stops continuing to grow.

The test conditions were replicated on Sample D, which was also irradiated with 300 eV Argon plasma at a flux of approximately 2.3×10^{21} $m^{-2}s^{-1}$ to a total cumulative ion fluence of 1.72×10^{26} m^{-2}. The results again showed a transient yield region leading up to a fluence around 1.4×10^{26} m^{-2} where again the yield measurements no longer increase.

The QCM measurements were compared to mass scale measurements of weight loss over the course of testing. It was determined that the mass scale results indicated a greater weight loss than that calculated from the QCM data. This difference may be attributed to calibra-

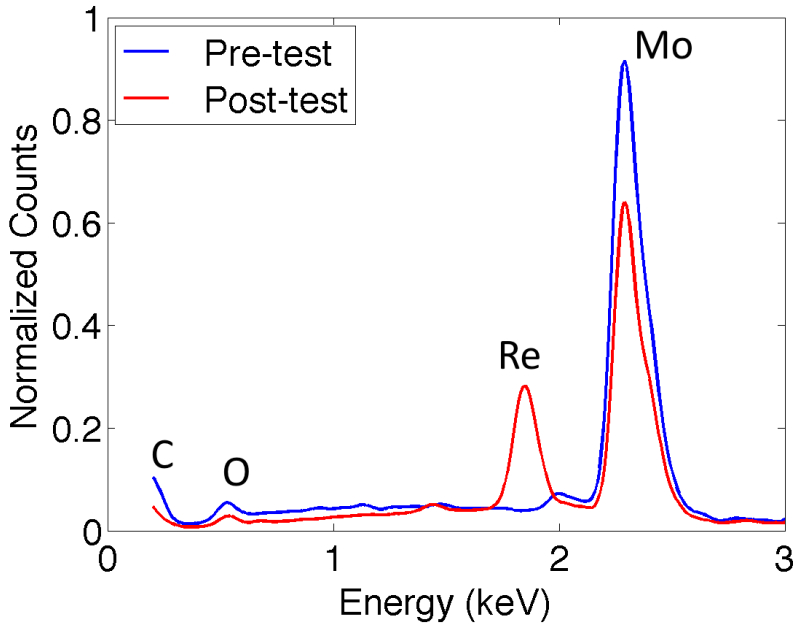

Figure 4.15: EDS spectrum for Sample B, before and after testing. The presence of the Re core is apparent in the spectrum as the Mo is eroded and both oxide and carbide surface layers are removed.

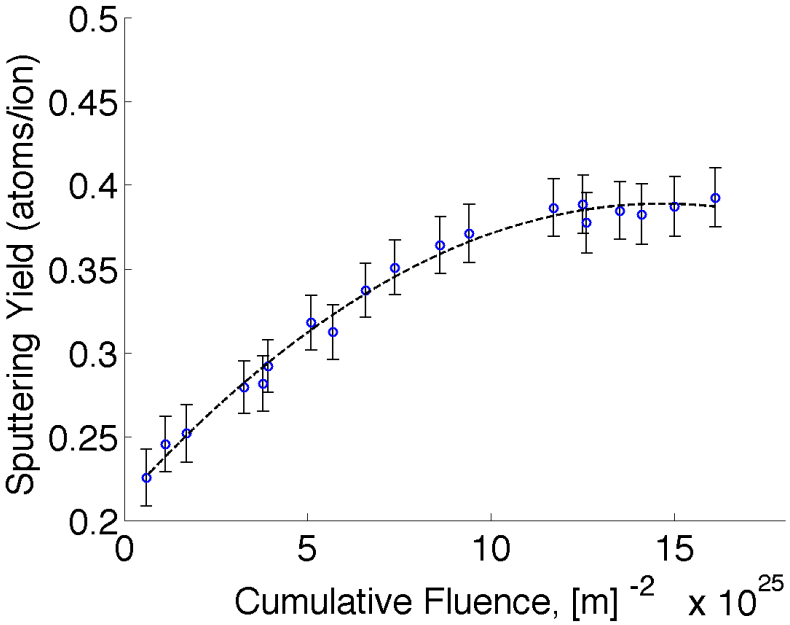

Figure 4.16: QCM measurements for Sample C prior to bias correction. The curve shows the dependence of the sputtering yield on ion fluence.

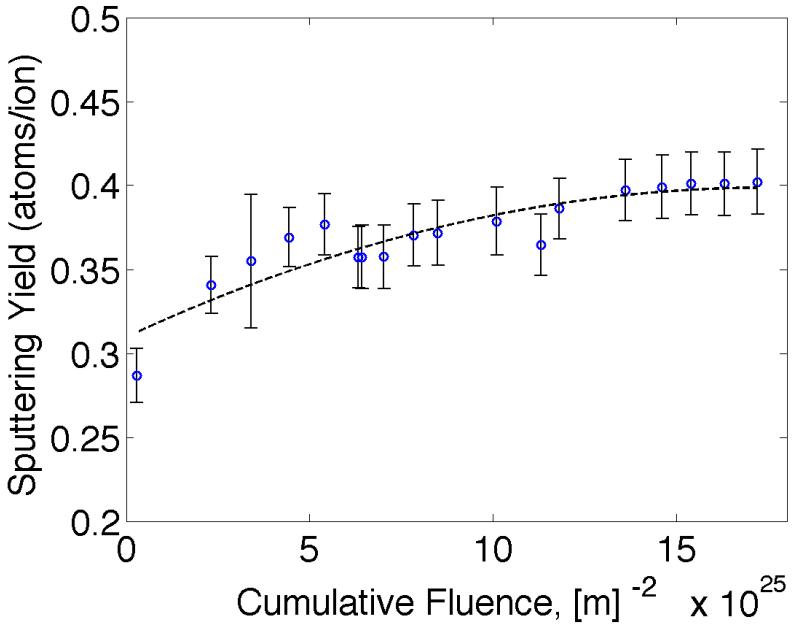

Figure 4.17: QCM measurements for Sample D prior to bias correction. The curve shows the dependence of sputtering yield on ion fluence, which experiences less variation than Sample C (Figure 4.16).

tion errors and assumptions made about the experimental setup, which affects calculations of the mass loss. Specifically, asymmetry in the sputter distribution can cause inaccuracies when the results are integrated over the hemisphere. Since the QCM probe only sweeps over one plane, an anisotropic sputter distribution would result in an underestimated mass loss if there is greater sputtering in other directions than the measured plane. This type of bias error attributed to the experimental setup would be consistent across the measurements, and the transient trend of the sputter yield at lower fluences would be unaffected. Assuming the true mass loss value to be reflected by the scale measurement, the magnitude of the bias may be determined for each test. For Sample D, the mass scale showed a loss of 2,060.9 mg, while the QCM estimated 2,360.7 mg, leaving a bias of about 13%. The mass scale had an accuracy of 1 mg, which accounts for a 0.3% error in the discrepancy between the two methods. For Sample C, the bias was measured at 8%. Correcting for this discrepancy allows for a closer comparison of the transient region.

Applying these corrections and plotting the data for both samples together in Figure 4.18,

it can be seen that there are differences between the samples in the yield magnitude over the transient region. The steady-state yield notably appears at approximately the same cumulative fluence, but the numbers leading up to that point diverge in the level of yield reduction. This difference can most likely be attributed to the morphological differences of the samples, where the less dense arrangement of surface formations on Sample D results in a lower amount of ballistic deposition and a higher rate of lost material than Sample C. Previous tests performed on planar molybdenum samples exposed to 300 eV Argon plasma have produced yields of approximately 0.4, which corresponds to the steady-state bound observed in these tests.

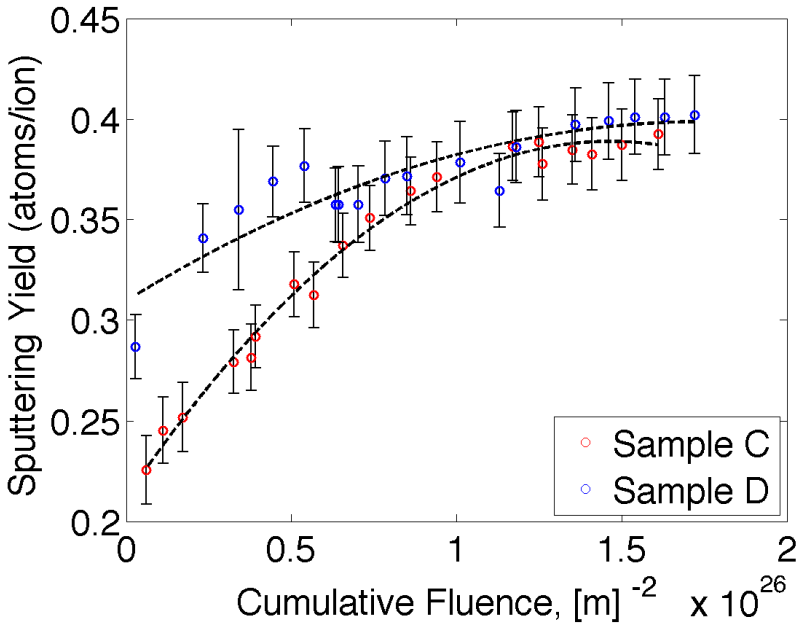

Figure 4.18: QCM yield measurements after correction for bias. The curves of Samples C and D are compared here to show the differences in yield dependence of their unique architectures.

4.4 Evolution of Surface Roughness

In the low fluence regime, Sample C was characterized between short exposures to track the morphological changes at early stages in the surface evolution. Profilometry was performed

on the sample using a Keyence VHX-1000 digital microscope to measure the surface roughness, ε, of the sample at each incremented level of fluence. In addition, the QCM provided corresponding yield measurements in the fluence range that was examined. Figure 4.19 shows the trends of the surface roughness and yield across the examined range of fluence. It can be seen that as the micro-architectured surface was eroded due to plasma exposure, the roughness value decreased and the yield value increased. The plot demonstrates how the yield increases in a linear fashion with fluence, which is the trend for the low fluence regime that was examined. At higher fluence scales, the transient curve emerges as previously presented. The surface roughness and sputtering yield are seen to be related linearly for the low fluence regime. This result demonstrates the morphological dependence of the sputtering yield, where the yield may be considered as a function of surface roughness.

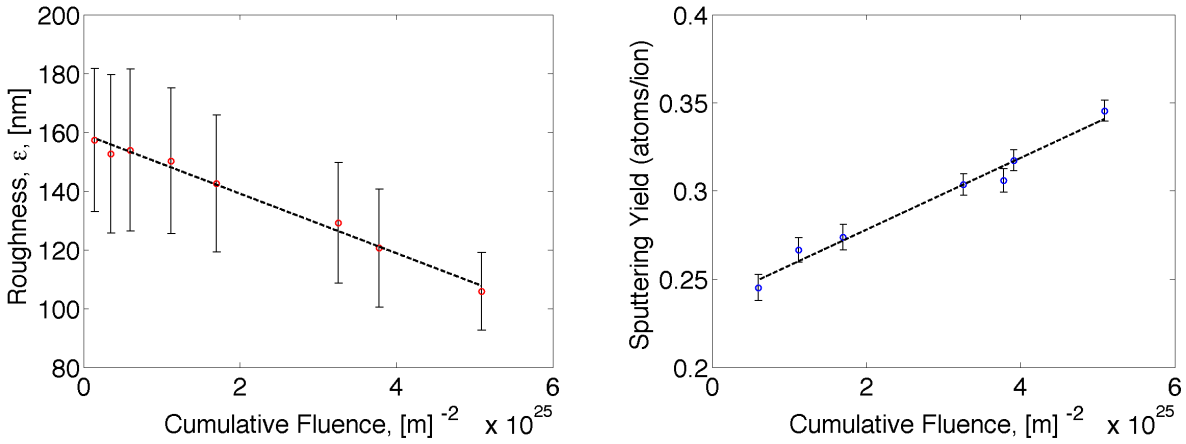

(a) (b)

Figure 4.19: Relationship between surface roughness and yield. (a) Evolution of surface roughness for low fluences. (b) Yield of material surface as roughness changes across low fluences.

4.5 Error considerations

Error due to noise was accounted for by calculating the standard deviation of the QCM rate measurements across the 1-minute collection time at each individual angle. In general, deviation in the measurements was found to be under 3%. Additional error can be attributed to

assumptions regarding the angular distribution of the sputter yield across the target. Since setup restrictions prevented measurements from being taken at angles below 30°, estimations were necessary at low angles to obtain an integrated yield number across the plane. Yamamura developed an empirical formula for the angular distribution of sputter yield that indicates a lessened rate of sputtering at lower polar angles[64, 63]. Therefore, there exist two bounds for the yield distribution. The first bound is assuming a yield of 0 normal to the target, and the second assumes there to be no decrease in the yield at lower angles by setting the yield at normal equal to that measured at 30°.

For micro-architectured materials, nonuniform orientations of the surface features cause incident ions to impinge the surface at oblique angles, and therefore the distribution cannot be accurately represented by Yamamura's fit. Figure 4.20 shows the angular sputter distribution at various levels of fluence. It can be seen that at the lowest fluence, when the surface is most textured, the distribution appears to have a flatter profile, likely matching more closely to the upper bound assumption. At the highest fluence where the surface is more planar, the distribution peaks near 40°, meaning that at lower angles the yield likely continues to decrease. These results indicate that the Yamamura formulation for angular dependence of the yield is not applicable to nano- and micro-architectured surfaces. With textured materials, the faces of the surface features are not consistently orientated to the QCM probe. The true angle for measuring the sputter rate is the average orientation of each of the surface features relative to where it is being measured. As the surface flattens, the measurements at each angle adjust to the expected sputtering angle, and the angular distribution follows the typical trend. A Yamamura fit is added to Figure 4.20 at lower angles to show the expected distribution according to that theory. The data presented in the plots is an averaged value of the upper and lower bounds. This results in an uncertainty error of approximately 5%.

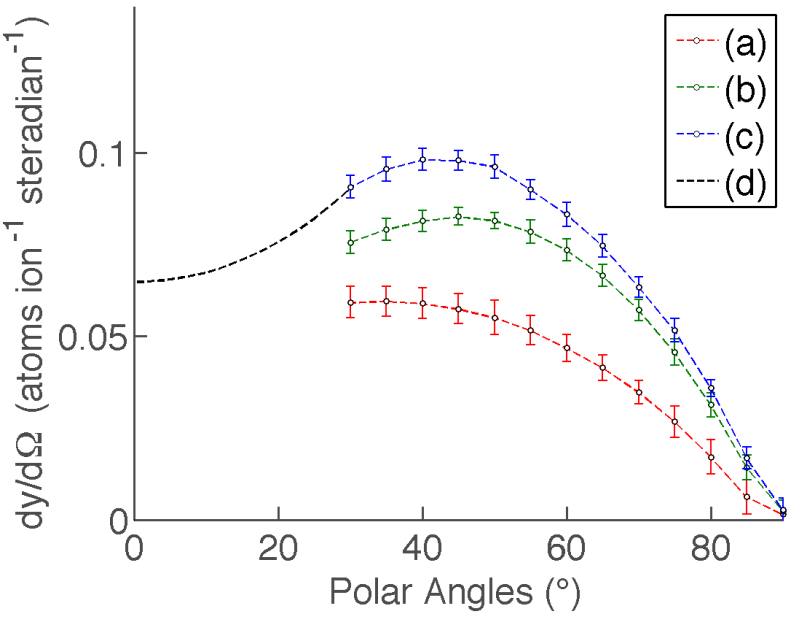

Figure 4.20: Measured QCM angular distribution at various fluence levels. (a) 5.99×10^{24} m^{-2} (b) 6.57×10^{25} m^{-2} (c) 1.61×10^{26} m^{-2} (d) Yamamura distribution curve for lower angle range. The curves show the evolution of angular sputter distribution at increasing levels of fluence.

4.6 Experimental Conclusions

This study has achieved a number of notable observations that provide insight into the various phenomena experienced during plasma sputtering. The fabrication of nano- and micro-architectured surfaces through a CVD process has allowed for an exploration of the effects of surface morphology on the sputtering rate of material surfaces under normal ion incidence. These material surfaces have been shown to have self-healing properties through their behavior under plasma irradiation.

The process of ballistic deposition has been observed through the tracking of spear-like and dendritic surface features across incremented levels of fluence. Sample A showed the appearance of deposition "islands," which grew in size and quantity through additional plasma exposure. The absence of plasma-mediated redeposition[35, 38] indicated the occurrence of ballistic deposition at the plasma fluxes used in these experiments. This phenomenon was

discerned at higher levels of fluence on both Samples A and B, in which larger surface formations were shown to possess qualities of both erosion and deposition. The tips of these features were shown to progressively deteriorate over increasing levels of plasma fluence, and the filling-in of crevices and widening of dendrite bases supported the hypothesis that the ablated surface material was deposited onto adjacent surfaces.

The sputtering yield of materials has been demonstrated to not only be a material property, but determined significantly by surface geometry. While the reduced sputtering yields of textured surfaces has been observed previously[20, 48, 67], this study established the transient nature of the sputtering yield. As plasma exposure affects the surface morphology over time, the sputtering yield will be altered according to the changes in surface geometry. This transience has can be quantified according to the plasma fluence, and has been shown to have different behavior depending on the initial surface structure. Differences in the texturing of Samples C and D showed that the rate of sputtering differed according to the density of surface features for the fractal-type textures used. Therefore, the rate of yield reduction throughout the transient sputtering regime is determined largely by the initial morphology of the material surface.

By integrating the curve-fit of the sputtering yield data for Sample C, it could be determined that a 16 percent reduction in the total number of sputtered atoms was experienced throughout the transient region. The textures examined for this study were a small representation of the variety of nano-architectured surfaces that can be produced. Therefore, the samples examined are likely not the optimal texture for yield reduction. Further exploration of other surface geometries may produce higher yield reduction, and provide further insight into the physical processes present during plasma exposure.

CHAPTER 5

Theoretical modeling of non-uniform surface evolution

Ion sputtering can lead to surface roughening, as well as the development of various types of surface features driven by erosive instabilities[37]. Experimental evidence shows that ion sputtering can result in the formation of periodic surface ripples[11, 24, 42, 49, 56]. The nature of these ripples, including their wavelength, amplitude, and orientation depends on a number of factors, such as ion energy, flux, angle of incidence, substrate temperature, and material properties. Considerable research has been done by a number of groups to examine the effects of these various parameters on the surface features that develop under ion bombardment.

The geometric effect of surface profiles on the erosion characteristics of ion-sputtered material surfaces offers great opportunity for further exploration. The development of nano- and micro-architectured surfaces introduces a new area of study, in which the effects of complex surface topography may alter the erosive development of a plasma-facing material surface. Practically speaking, understanding the nature of these textured geometries may offer the potential to design sputter-resistant surfaces. Surfaces of this variety may be characterized by a network of dendritic structures produced through a chemical vapor deposition (CVD) process. Experimental work has shown that these nano-textured surfaces demonstrate a decrease in the net sputter rate at normal ion incidence compared to planar surfaces.

The improved behavior of architectured dendritic surfaces may be attributed to several physical factors. Thermal stresses are reduced, resulting from the capability of fine surface features to withstand a greater level of distortion. Additionally, net sputtering erosion from the ion bombardment is minimized because of geometric trapping of re-deposited

atoms. Further, the higher surface area promotes better heat distribution, preventing localized overheating. While these material structures possess attributes that can improve the resilience and longevity of sputtered surfaces, there is much to be understood about their ability to withstand degradation according to traditional sputter erosion models. Therefore, it is desired to explore the effect of various surface structures on the erosive evolution of a material surface that is subjected to ion bombardment.

The present work aims to understand the relationship between initial architecture and pattern evolution of an ion-bombarded surface, focusing specifically on erosive processes. We begin by reviewing the framework used to explain the underlying erosion mechanisms controlling surface morphology, as well as theoretical attempts to model deposition. The interest here is to compare analytical theory to numerical simulations presented later, in order to reveal the role of nonlinear phenomena on pattern selection, stability, and long-term evolution.

5.1 Review of theoretical models

A number of theoretical approaches have been taken to physically model the evolving surface of an ion-exposed material. Koponen[30] used a Fourier transform method to show the development of surface ripples at various stages in the course of bombardment. The results of this simulation showed that ripples of a defined wavelength begin to grow after sufficient evolution time. Surface evolution has also been modeled at the atomic level using kinetic Monte-Carlo (KMC) methods. Bharathi et. al.[3] presented a KMC model that exhibited compositional changes in surface ripple patterns that formed as a result of ion sputtering. It was found that if the sputter yield of one alloy component was set higher than another, surface troughs showed lower presence of this component, indicating preferential erosion of the troughs. Additionally, when the diffusivity of component A was set higher than component B, and both components possessed equal sputter yields, the troughs showed a richer composition of component A, meaning that surface diffusion works against the erosive

effects of sputtering.

Chason et. al.[8] produced a KMC model that investigated the concurrent effects of temperature and ion flux on pattern formation by observing how the developed ripple wavelength changed according to these parameters. It was found that for higher temperatures, the ripple wavelength decreased more rapidly with increasing flux. The results indicated that at high temperature or low flux, thermal diffusion was the dominant mechanism determining pattern formation, while at lower temperatures or high flux, the morphology was determined largely by erosive effects.

Madi[36] and Norris[43] both performed molecular dynamics (MD) simulation to argue that ion impact-induced mass redistribution, rather than erosion, is the prominent cause of surface patterning and smoothening for various angles of incidence. This conclusion was not valid, however, for higher ion energies or rough surfaces, as the simulations were performed assuming smooth, planar surfaces. Therefore, the scope of understanding surface evolution as a mass redistribution problem is limited.

Recent work has considered the formation of surface patterns on ion-irradiated surfaces to be caused by a hydrodynamic mechanism. This approach proposes incompressible solid flow occurs in an amorphous layer, resulting in the formation of surface ripples at the amorphous-crystalline interface, thereby appearing on the free surface. This model is in contrast to the standard mechanisms proposed by Bradley and Harper, based on collision-based erosion and mass redistribution at the free surface.

Castro et. al.[7] proposed the generalized theoretical framework for the hydrodynamic method, where an induced stress from the ion beam acts as a "effective gravity," to induce solid flow. The effective gravity varies over the surface, determined largely by the local surface orientation relative to the ion beam. The theory begins with the conservation of momentum, expressed generally as follows in terms of the velocity field of the fluidized layer

$\boldsymbol{V}$:

$$\rho \frac{D\boldsymbol{V}}{Dt} \equiv \rho \left(\partial_t \boldsymbol{V} + \boldsymbol{V} \cdot \nabla \boldsymbol{V} \right) = \nabla \cdot \boldsymbol{T} \tag{5.1}$$

where $\boldsymbol{T}$ is the the stress tensor. Considering the amorphous layer as a highly viscous fluid, $\boldsymbol{T}$ may be expressed in the following way:

$$T_{ij} = -P\delta_{ij} + \mu \left(\partial_i u_j + \partial_j u_i \right) + T^s_{ij} \tag{5.2}$$

where T^s_{ij} represents the stress field terms not originating from hydrostatic pressure, P, or viscous flow. The components of the velocity field are expressed by $u_{1,2,3} = u, v, w$. The stress field contributes to a body force acting in the bulk of the fluid layer. This body force is thought of as the effective gravity. Therefore, determination of body forces originating from the effects of the ion beam will allow for the determination of the velocity field.

Kumar et. al.[31] presented the hypothesis that ripple formation originates at the amorphous-crystalline interface as a result of erosion and redeposition of material atoms undergoing solid flow, supported by experimental work using silicon surfaces. The incompressibility of the solid mass flow in the amorphous layer indicates that the structures formed at the interface are reflected on the free surface. Ripple wavelength is determined by the solid flow velocity of the amorphous layer, while the amplitude is controlled by the amount of material to be transported at the interface.

Additionally, the study of stress-induced instabilities examines the influence of surface roughening on material profiles. Asaro and Tiller[2] presented a diffusion-based theory for surface roughening, later expanded to generalized stressed solids by Srolovitz[55, 66]. The model demonstrates how an initially planar surface of a uniaxially stressed solid will develop an instability in which any perturbation will become increasingly amplified. This result is attributed to the principle of minimum potential energy, in which the lower elastic energy of rippled surfaces cause an instability to form in the absence of a stabilizing mechanism[44].

The free energy functional of the surface $\mathcal{F}[h]$ is minimized by the chemical potential μ by means of the variational derivative[37],

$$\mu = \frac{\delta \mathcal{F}[h]}{\delta h} \tag{5.3}$$

The chemical potential is given by

$$\mu = \mu_0 + \Delta W \Omega + \gamma \kappa \Omega \tag{5.4}$$

where μ_0 is the chemical potential of an unstressed surface, ΔW is the strain energy density, κ is the mean curvature, Ω is the atomic volume, and γ is the surface free energy.

Focusing on the surface kinetics of a material with geometric instabilities resulting from surface diffusion, it is known that the surface morphology is locally dependent on changes in the chemical potential. The velocity of surface deviations is determined by the flux of surface atoms, J, given by

$$J = -\frac{D_s}{kT} \nabla \mu \tag{5.5}$$

where D_s is the surface diffusivity, and kT is the thermal energy. The divergence of this atomic flux expression produces the change in the number of atoms per unit time into the volume element at the surface. Mass conservation leads to a height evolution equation when approximating the divergence in the x-direction[18].

$$\frac{dh}{dt} = -\frac{\rho_s \Omega D_s}{kT} \nabla_x^2 \mu \tag{5.6}$$

where ρ_s is the atomic surface density. If stress effects are ignored, the chemical potential from Equation (5.4) is simply a function of the surface curvature, κ. As the radius of curvature can be approximated as the second derivative of the surface height, the above

expression may be written as a fourth-order term[41]

$$\frac{dh}{dt} = -K\nabla^2(\nabla^2 h) \equiv -K\nabla^4 h \tag{5.7}$$

where

$$K = \frac{D_s \gamma \Omega^2 \rho_s}{kT} \tag{5.8}$$

The current work expands the scope of modeling surface evolution by considering a number of variables, including ion parameters, angle of ion incidence, and initial architecture. In addition, the effect of deposition will be considered as a factor that influences the evolution of a plasma-sputtered surface, in addition to erosive effects. An evolution equation will be derived in the following sections, and modeling efforts will focus on examining the influence of the various equation components to better understand their physical implications.

5.2 Theory of ion-induced erosion

5.2.1 General framework

The sputter yield Y_0 is defined as the average number of atoms ablated for each incident ion that bombards the surface of a material. This value is important in predicting the morphological development of a surface experiencing ion bombardment. Determining the sputter yield of a material begins with an understanding of the mechanisms that control the sputtering process. In Sigmund's theory of sputtering[52, 53], the average energy deposited by an ion within the bulk of a material is described by the Gaussian distribution:

$$E(r) = \frac{\epsilon}{(2\pi)^{3/2}\alpha\beta^2} \exp\left\{-\frac{Z'^2}{2\alpha^2} - \frac{X'^2 + Y'^2}{2\beta^2}\right\} \tag{5.9}$$

Here α is the parallel and β the perpendicular distribution width (Figure 5.1), and ϵ is the total energy deposited. Z' is the distance from point P to point O, projected along the

ion trajectory. X', Y', are measured in the plane perpendicular to it. The physical process involves an ion penetrating the surface a distance a, and lands at point P, where it releases its kinetic energy as a Gaussian with widths α and β. Surface geometries have a significant bearing on the consideration of Sigmund's model. Non-uniform profiles result in varying erosive effects, depending on the distance of a surface point from the center of the collision cascade, where an impinging ion releases its energy distribution (Figure 5.2).

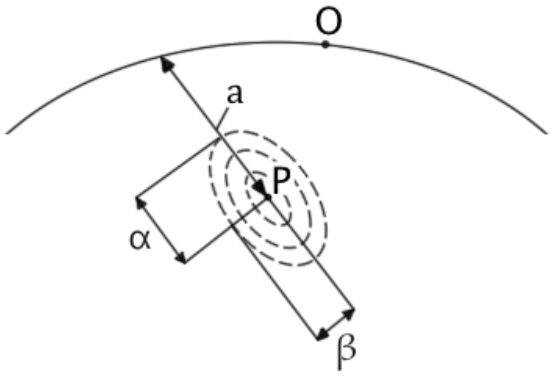

Figure 5.1: Energy distribution of an incident ion. a is the mean range of ion penetration, and α and β are the dimensions of the collision cascade.

When an obliquely-incident ion bombards the surface of a material, it initiates a collision cascade downstream, leading to the removal of atoms affected by the energy distribution. This process begins as the incoming ion embeds itself in the bulk of the material and transfers some of its energy to the atoms it comes in contact with. These atoms then may experience secondary collisions, producing the collision cascade. Some atoms will receive enough energy to be permanently displaced from their lattice sites. Those atoms close to the surface that receive enough energy to break their bonds will be sputtered. Figure 5.2 shows physically how the surface curvature affects the erosion. The collision cascade originating from an ion penetrating at P (P$'$) affects a point on the surface at O (O$'$). Here we see that the distance between the source of the collision cascade and O$'$ is much greater than it is to O. Therefore in the case of concave curvature, O will be more significantly affected than the case of convex curvature, O$'$, and more material will be removed[6].

The analytical description of sputtering developed by Sigmund is important in developing

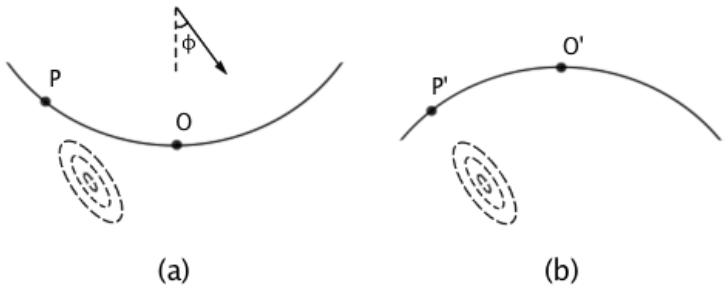

Figure 5.2: Illustration of the effect of the collision cascade on surface features of differing curvature

a quantitative model for surface evolution. Using the approximation for the average energy deposition, it can be shown that the yield depends on the curvature of the material surface.

Following Sigmund's theory[53], a theoretical model can be developed using the framework by Makeev et al.[37] to describe the evolution of surface ripples on an ion-sputtered surface. The model begins with the principle of conservation of energy, in which the energy deposited onto the surface by incoming ions is equivalent to the energy lost through the removal of material.

$$E_{in} = E_{out} \tag{5.10}$$

The former is accounted for by taking the product of the ion flux $\Phi(\boldsymbol{r})$ with the average energy deposited per incoming ion, described by Equation (5.9). The quantity is then integrated over the region $\mathcal{R}$, where energy is deposited by incoming ions. This expression is equivalent to the flux of removed particles, J_{out}, multiplied by the surface binding energy, U_0.

$$\int_{\mathcal{R}} \boldsymbol{dr}\Phi(\boldsymbol{r})E(\boldsymbol{r}) = J_{out} \cdot U_0 \tag{5.11}$$

The particle flux may be expressed as the atomic density of ablated particles, n_{out}, mul-

tiplied by the local erosion velocity normal to the surface, v_n.

$$= n_{out} \cdot v_n \cdot U_0 \tag{5.12}$$

$$= \frac{4\pi^2}{3} N C_0 \cdot U_0 v_n \tag{5.13}$$

Where C_0 is proportional to the square of the effective radius of the interatomic interaction potential, and N is the atomic density. The normal erosion velocity is therefore proportional to the energy deposited by incoming ions in the following way[37]:

$$v_n = p \int_{\mathcal{R}} \boldsymbol{dr} \Phi(\boldsymbol{r}) E(\boldsymbol{r}) \tag{5.14}$$

The material constant p facilitates the determination of the normal velocity resulting from the energy distribution of incoming ions, as it is inversely dependent on the surface binding energy.

$$p = \frac{3}{4\pi^2} \frac{1}{N U_0 C_0} \tag{5.15}$$

In the above derivation, $\Phi(\boldsymbol{r})$ is the correction to the ion flux in the normal direction to the local surface orientation:

$$\Phi(\boldsymbol{r}) \simeq J_{in} \left(\cos\varphi + (\partial_x Z) \sin\varphi\right) \tag{5.16}$$

For further explanation of the derivation of the normal erosion velocity, refer to Appendix A. This form of the equation allows for an understanding of the geometrically dependent erosion instability, in which the curvature terms either contribute to or resist an increase in the magnitude of the erosion velocity, depending on the sign of the curvature. This physical phenomenon is previously discussed, and illustrated in Figure 5.2.

Next, a transformation must be done between the local and laboratory coordinates (see Figure 5.3) to relate the normal velocity of erosion v_n to the velocity of erosion along the h

axis[12].

$$\frac{\partial h}{\partial t} = -v_n\sqrt{g} \tag{5.17}$$

Here $g \equiv 1 + (\partial_x h)^2 + (\partial_y h)^2$, so that $\sqrt{g}$ is the magnitude of the vector normal to the surface. The negative sign is needed to reflect the rate at which the hight decreases, as v_n is simply the erosion velocity. For further notes on this projection, refer to Appendix B.

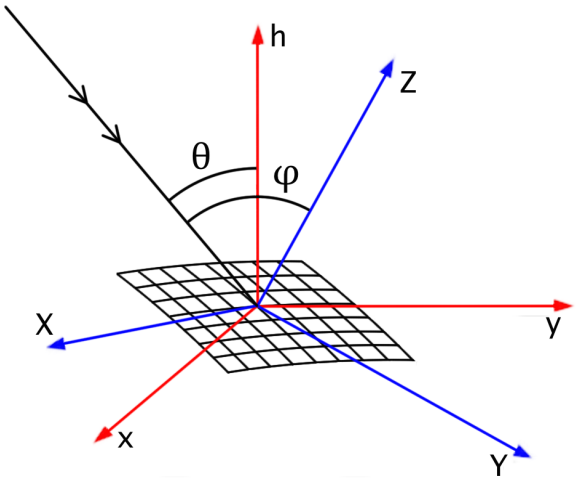

Figure 5.3: Illustration of the local reference frame (X, Y, Z) relative to the laboratory frame (x, y, h). θ is the angle between the h-axis and the ion trajectory, and φ is the angle between the local normal, Z, and the ion trajectory.

Additionally, the effect of surface diffusion acts as a stabilizing mechanism to the equation, and is joined into the theory by the inclusion of an additional term.

$$\frac{\partial h}{\partial t} = -v_n\sqrt{g} - K\nabla^4 h \tag{5.18}$$

The surface diffusion is temperature-induced, with coefficient K given by:

$$K = \frac{D_s \gamma \Omega^2 \nu}{kT} \tag{5.19}$$

where D_s is the surface diffusivity, γ is the surface free energy density, Ω is the atomic volume, ν is the number of atoms per unit volume, k is Boltzmann's constant, and T is the

absolute temperature.

The Taylor series expansion of the first term in Equation (5.18) was approximated to third order by Makeev et. al.[37] to produce:

$$\begin{aligned}\frac{\partial h}{\partial t} =& - v_0 + \gamma\frac{\partial h}{\partial x} + \xi_x\left(\frac{\partial h}{\partial x}\right)\left(\frac{\partial^2 h}{\partial x^2}\right) + \xi_y\left(\frac{\partial h}{\partial y}\right)\left(\frac{\partial^2 h}{\partial y^2}\right) + \nu_x\frac{\partial^2 h}{\partial x^2} + \nu_y\frac{\partial^2 h}{\partial y^2} \\ &+ \Omega_1\frac{\partial^3 h}{\partial x^3} + \Omega_2\frac{\partial^3 h}{\partial x\partial y^2} - D_{xy}\frac{\partial^4 h}{\partial x^2\partial y^2} - D_{xx}\frac{\partial^4 h}{\partial x^4} - D_{yy}\frac{\partial^4 h}{\partial y^4} - K\nabla^4 h \\ &+ \frac{\lambda_x}{2}\left(\frac{\partial h}{\partial x}\right)^2 + \frac{\lambda_y}{2}\left(\frac{\partial h}{\partial y}\right)^2 + \eta(x,y,t) \end{aligned} \tag{5.20}$$

This expansion produces an equation form that corresponds to similar efforts at modeling surface evolution. Three different such instances are examined following the above expansion: Bradley-Harper, Kardar-Parisi-Zhang, and Kuramoto-Sivashinsky. Each of these equation forms may be used to model the height evolution of a surface.

5.2.2 Bradley-Harper (BH) Theory

Bradley and Harper[6] developed an approximation for an expansion similar to that of equation (5.18) by deriving an equation to model surface erosion under ion bombardment according to the ion parameters and surface geometry. The following equation expresses the erosive velocity relative to the local normal of the surface:

$$v_n = \frac{J\epsilon pa}{\sqrt{2\pi}\alpha\beta}\exp\left(-\frac{a_\alpha^2}{2} + \frac{A^2}{2B_1}\right)\frac{1}{\sqrt{B_1}}\left[\cos\varphi + \Gamma_X\frac{a}{2}\left(\frac{\partial^2 Z}{\partial X^2}\right) + \Gamma_Y\frac{a}{2}\left(\frac{\partial^2 Z}{\partial Y^2}\right)\right] \tag{5.21}$$

where $a_\alpha = a/\alpha$ and the coefficients Γ_X and Γ_Y are functions of the collision cascade and angle of incidence:

$$\Gamma_X = \left\{ -\frac{2A}{B_1}\sin\varphi + \frac{B_2}{B_1}\left[1 + \frac{A^2}{B_1}\right]\cos\varphi + \frac{2AC}{B_1^2}\left[3 + \frac{A^2}{B_1}\right]\cos\varphi \right\} \tag{5.22a}$$

$$\Gamma_Y = \left\{ \frac{2}{a_\beta^2}\cos\varphi\left(\frac{B_2}{2} + \frac{AC}{B_1}\right) \right\} \tag{5.22b}$$

and for an isotropic energy distribution ($\alpha = \beta$) the variables are defined as:

$$A = a_\alpha^2 \sin\varphi \tag{5.23a}$$

$$B_1 = a_\alpha^2 \tag{5.23b}$$

$$B_2 = a_\alpha^2 \cos\varphi \tag{5.23c}$$

$$C = 0 \tag{5.23d}$$

This produces the following coefficients:

$$\Gamma_X = -2\sin^2\varphi + \left(1 + a_\alpha^2 \sin^2\varphi\right)\cos^2\varphi \tag{5.24a}$$

$$\Gamma_Y = \cos^2\varphi \tag{5.24b}$$

This result can be written more simply in terms of the yield, $Y_0(\varphi)$, and the radius of curvature in the X and Y direction, R_X and R_Y, understanding that the second derivative of the height is equivalent to the curvature.

$$v_n(\varphi, R) = \frac{J}{n} Y_0(\varphi)\left[\cos\varphi - \Gamma_X(\varphi)a/R_X - \Gamma_Y(\varphi)a/R_Y\right] \tag{5.25}$$

where the yield is written as:

$$Y_0(\varphi) = \frac{\epsilon pan}{\sqrt{2\pi}\alpha\beta} \exp\left(-\frac{a^2}{2\alpha^2} + \frac{A^2}{2B_1}\right) B_1^{-1/2} \tag{5.26}$$

The local erosion velocity equation is then projected to the laboratory frame to produce a height evolution equation, as shown in Equation 5.17. Additionally, a term is added to account for temperature-induced surface diffusion effects.

$$\frac{\partial h}{\partial t} = -v_0 + \gamma\frac{\partial h}{\partial x} - \frac{Ja}{n} Y_0(\theta)\left[\Gamma_X(\theta)\left(\frac{\partial^2 h}{\partial x^2}\right) + \Gamma_Y(\theta)\left(\frac{\partial^2 h}{\partial y^2}\right)\right] - K\nabla^4 h \tag{5.27}$$

The result is a linear equation that describes the formation of surface ripples on an ion-

bombarded surface.

5.2.3 Surface evolution described by Kardar-Parisi-Zhang (KPZ) and Kuramoto-Sivashinsky (KS) Equations

Aside from ion patterning models, it is important to understand the equation forms used for various continuum theories to describe kinetic roughening. These theories help to develop a physical understanding of the morphological changes taking place in ion bombardment. The theoretical approaches used to model the evolution of surface morphologies are an important part of deciphering the parameters that control surface evolution.

The Kardar-Parisi-Zhang (KPZ) equation, presented to describe the profile of a growing interface[28], can be used for the time evolution of the surface height profile, taking into account random height increases as well as local smoothing[21].

$$\frac{\partial h}{\partial t} = \nu \nabla^2 h + \frac{\lambda}{2}(\nabla h)^2 + \eta \tag{5.28}$$

The first term can be considered as a relaxation term, where ν is the effective surface tension[37]. The height progression can be solved exactly by the deterministic portion of the equation, excluding the stochastic term. A linear version of this equation was explored by Edwards and Wilkinson[15], which describes surface fluctuations of a growing interface under equilibrium conditions, where the profile develops to minimize its area. The nonlinear term is necessary to sufficiently describe the growth properties, where lateral growth is present.

Considering anisotropy of the substrate introduces directional variations to the equation, and better describes the process of oblique ion bombardment, where ions impinge the surface directed along a particular plane.

$$\frac{\partial h}{\partial t} = \nu_x \partial_x^2 h + \nu_y \partial_y^2 h + \frac{\lambda_x}{2}(\partial_x h)^2 + \frac{\lambda_y}{2}(\partial_y h)^2 + \eta(x, y, t) \tag{5.29}$$

The anisotropic form of the KPZ equation was introduced by Villain[57] to describe crystal growth by ion beams at different length scales. In the case that $\nu_x = \nu_y$ and $\lambda_x = \lambda_y$, the anisotropic form (5.29) follows the original form (5.28).

The Kuramoto-Sivashinsky (KS) equation is a deterministic, nonlinear equation originally developed to describe chemical turbulence[32] and laminar flame fronts[54].

$$\frac{\partial h}{\partial t} = -|\nu|\nabla^2 h - K\nabla^4 h + \frac{\lambda}{2}(\nabla h)^2 \tag{5.30}$$

The KS equation has been shown to offer a similar analytical description of the surface as the KPZ equation[37]. The equation itself exhibits unstable behavior, with the second order term accountable for instability at long scales. The fourth order term providing damping at short scales, and characterizes the dissipative nature of the equation as it provides a smoothing effect.

In addition, a damping term may be added to produce the Damped Kuramoto-Sivashinsky (DKS) equation.

$$\frac{\partial h}{\partial t} = -\alpha h - |\nu|\nabla^2 h - K\nabla^4 h + \frac{\lambda}{2}(\nabla h)^2 \tag{5.31}$$

The damping term results in smoothing of all spatial frequencies, thereby inhibiting kinetic roughening[29]. Its presence in the continuum equation for ion-bombarded surfaces has been used to account for redeposition of sputtered material[17], although this hypothesis has been disputed.

5.2.4 Proposed evolution equation

Using the generalized framework shown, the selected equation follows the theory outlined by the BH model[6], while possessing elements of the KPZ and KS equation forms. The resulting equation contains a second order term to account for geometric effects, a nonlinear term, and a fourth order stabilizing term to model temperature-induced surface diffusion.

The equation is an outgrowth of the presented framework, and is expressed in the following way:

$$\partial_t h = -v_0 + \frac{Fa}{2}\left[\nu_x\left(\frac{\partial^2 h}{\partial x^2}\right) + \nu_y\left(\frac{\partial^2 h}{\partial y^2}\right)\right] + \frac{Fa_\alpha^2}{2}\left[\lambda_x\left(\frac{\partial h}{\partial x}\right)^2 + \lambda_y\left(\frac{\partial h}{\partial y}\right)^2\right] - K\nabla^4 h \tag{5.32}$$

where the coefficients are defined as

$$\nu_x = 2s^2 - c^2 - a_\alpha^2 s^2 c^2 \tag{5.33a}$$

$$\nu_y = -c^2 \tag{5.33b}$$

$$\lambda_x = 3s^2 c - c^3 - a_\alpha^2 s^2 c^3 \tag{5.33c}$$

$$\lambda_y = -c^3 \tag{5.33d}$$

with $c = \cos\varphi$ and $s = \sin\varphi$. In the expressions the following notation is defined as:

$$F = \frac{J\epsilon p a_\alpha^2 e^{-a_\alpha^2/2}}{2(2\pi)^{1/2}} \tag{5.34}$$

Equation (5.32) is the time evolution equation of the surface in the laboratory frame. This expression has been simplified for normal ion incidence ($\theta = 0$), and by assuming an isotropic, or spherical energy distribution for the collision cascade (i.e. $\alpha = \beta$).

5.2.5 Proposed evolution equation with deposition

It has been proposed that self-deposition can be modeled for normal incidence ion bombardment by the addition of a nonlinear term to the equation of motion[5]. Developing this expression begins by considering the atomic flux between these points, which is determined by the fraction of sputtered particles that are reaching a point of interest on the surface from a source point. Bradley shows that this fraction can be approximated according to

the distance between them, resulting in a nonlinear term. This quantity can be integrated over the surface area to obtain the change in height per unit time attributed to deposition of sputtered particles at a particular point on the surface.

While the nonlinear effect presented by Bradley is useful to account for geometric proximity of sputtered particles, it presents challenges in its computational cost. Additionally, the expression possesses a singularity for close-proximity points, which limits its use for numerical modeling. Alternatively, it has been proposed that redeposition may be more simply modeled by amending the evolution equation to include linear damping with the addition of a simple term, $-\alpha h$ [17, 29]. For numerical simulations, however, the evolution equation requires translational invariance, which is violated by the damping term. This can be addressed by replacing the damping term with an adjusted term, $-\alpha h_s$, calculated using a standardized height profile $h_s = (h - h_A)$, where h_A is the average surface height at the particular time step. The result draws from the form of the DKS equation, where the damping term acts as a stabilizing mechanism, which suppresses secondary instabilities within a particular range of values and prevents kinetic roughening[29].

$$\frac{\partial h}{\partial t} = -\alpha h_s - v_0 + \frac{Fa}{2}\left[\nu_x\left(\frac{\partial^2 h}{\partial x^2}\right) + \nu_y\left(\frac{\partial^2 h}{\partial y^2}\right)\right] + \frac{Fa_\alpha^2}{2}\left[\lambda_x\left(\frac{\partial h}{\partial x}\right)^2 + \lambda_y\left(\frac{\partial h}{\partial y}\right)^2\right] - K\nabla^4 h \tag{5.35}$$

Surface evolution can be modeled using the above final equation form with the stabilizing effects of the damping term, and compared to the results obtained without linear damping.

The damping term depends directly on the surface position, h, rather than its derivatives, indicating that its effect goes exceeds the scope of Sigmund's theory of sputtering[53]. The influence of this term on the surface morphology may be explained as the self-deposition of sputtered material resulting from ion bombardment[17]. When patterning is present, a significant amount of material may be deposited due to line-of-sight interaction of the

ablated material with the adjacent surface features. This effect is more significant in the surface troughs rather than the peaks, thereby producing a damping effect to the curvature instabilities described in the Bradley-Harper model[6].

5.3 Linear stability analysis

Linear stability of the evolution equation is examined by submitting the system to small perturbations and observing the behavior. For small perturbations, the nonlinear terms may be eliminated from the governing equation[58]. Performing a Galilean transformation, a non-dimensionalized form of Equation (5.35) may be written:

$$\frac{\partial \bar{h}}{\partial \tau} = -\bar{\alpha}\bar{h}_s + \bar{\nu}_x \left(\frac{\partial^2 \bar{h}}{\partial X^2}\right) + \bar{\nu}_y \left(\frac{\partial^2 \bar{h}}{\partial Y^2}\right) - \bar{K}\left(\frac{\partial^4 \bar{h}}{\partial X^4} + \frac{\partial^4 \bar{h}}{\partial X^2 \partial Y^2} + \frac{\partial^4 \bar{h}}{\partial Y^4}\right). \tag{5.36}$$

where $\bar{h} = \frac{a_\alpha^2}{a}\, h$, $X = \frac{2a_\alpha}{a}\, x$, $\tau = \frac{2Fa_\alpha^2}{a}\, t$, $\bar{\alpha} = \frac{a}{2Fa_\alpha^2}\, \alpha$, $\bar{K} = \frac{8a_\alpha^2}{Fa^3}\, K$. Equation (5.36) may be written in Fourier transform as follows:

$$\sigma_\tau \bar{h} = \left[-\bar{\alpha} + \left(-\bar{\nu}_x q_x^2\right) + \left(-\bar{\nu}_y q_y^2\right) - \bar{K}\left(q_x^2 + q_y^2\right)^2\right] \bar{h}. \tag{5.37}$$

Considering the magnitude of the coefficients only, and dividing out $\bar{h}$ leads to an evolution equation for the amplitude of the spatial mode $\vec{q}$ where $q^2 = q_x^2 + q_y^2$.

$$\sigma_\tau = -\bar{\alpha} + |\bar{\nu}_x| q_x^2 + |\bar{\nu}_y| q_y^2 \; - \bar{K}\left(q_x^2 + q_y^2\right)^2 \tag{5.38}$$

A critical wavenumber is defined as $q_c^2 = \frac{|\bar{\nu}_x|}{2\bar{K}}$, leading to the following expression:

$$\sigma_\tau = \left(-\bar{\alpha} + |\bar{\nu}_x| q^2 - \bar{K} q^4\right) - \left(|\bar{\nu}_x| - |\bar{\nu}_y|\right) q_y^2 \tag{5.39}$$

$$= \epsilon - \bar{K}\left(q^2 - q_c^2\right)^2 - \left(|\bar{\nu}_x| - |\bar{\nu}_y|\right) q_y^2 \tag{5.40}$$

where $\epsilon = \frac{\bar{\nu}_x^2}{4\bar{K}} - \bar{\alpha}$. For positive values of ϵ, where $\bar{\alpha}$ is less than $\frac{\bar{\nu}_x^2}{4\bar{K}}$, spatial modes with $\vec{q} = \pm q_c \vec{1}_x$ are unstable, that is $\vec{q} = \pm\sqrt{\frac{|\bar{\nu}_x|}{2\bar{K}}}\vec{1}_x$.

Alternately, for $\bar{\alpha} = \frac{\bar{\nu}_y^2}{4\bar{K}}$ the modes with $\vec{q} = \pm\sqrt{\frac{\bar{\nu}_y}{2\bar{K}}}\vec{1}_y$ become unstable in the y-direction.

$$\sigma_\tau = \frac{\bar{\nu}_x^2 - \bar{\nu}_y^2}{4\bar{K}} - \bar{K}\left(q^2 - q_c^2\right)^2 - \left(|\bar{\nu}_x| - |\bar{\nu}_y|\right) q_y^2 \tag{5.41}$$

$$= \frac{\bar{\nu}_x^2}{4\bar{K}} - \frac{\bar{\nu}_y^2}{4\bar{K}} - \bar{K} q_y^4 + q_y^2|\bar{\nu}_x| - \frac{\bar{\nu}_x^2}{4\hat{K}} - q_y^2|\bar{\nu}_x| + q_y^2|\bar{\nu}_y| \tag{5.42}$$

$$= -\frac{\bar{\nu}_y^2}{4\bar{K}} - q_y^2\left(\bar{K} q_y^2 - |\bar{\nu}_y|\right) \Rightarrow q_y = \sqrt{\frac{\bar{\nu}_y}{2\bar{K}}} \tag{5.43}$$

The selected wavelength is determined from the most unstable wave vector, solved using the dispersion relation:

$$\lambda_i = \frac{2\pi}{q_i} = 2\pi\left(\frac{2\bar{K}}{|\bar{\nu}_x|}\right)^{\frac{1}{2}} \tag{5.44}$$

The resulting wavelength expression is very parameter sensitive, meaning that the scale of the selected wavelength depends significantly on the variables that determine the diffusive coefficient $\bar{K}$ and the erosive coefficient $\bar{\nu}_x$. Figure 5.4 illustrates the wavelength scale at various values of temperature, which is inversely proportional to $\bar{K}$, as well as increasing values of ion flux, J, which is directly proportional to the erosive coefficient. It can be seen that the scale ranges from nanometer to millimeter in scale, depending on the magnitude of ion flux and temperature. Other parameters, including ion energy ϵ, penetration depth a, and the dimensions of the collision cascade likewise affect the erosive contribution, while material properties such as the surface diffusivity and atomic density affect the diffusive contribution. Similarly, consideration of stress effects in developing the evolution equation will have a significant bearing on the size of ripples that form.

The range of size scale of ripples observed in plasma-facing materials has been well documented. As previously reviewed, nano-ripples were observed on glass substrates early on by Navez, et. al.[42]. In addition, ripple formations have been seen to develop on

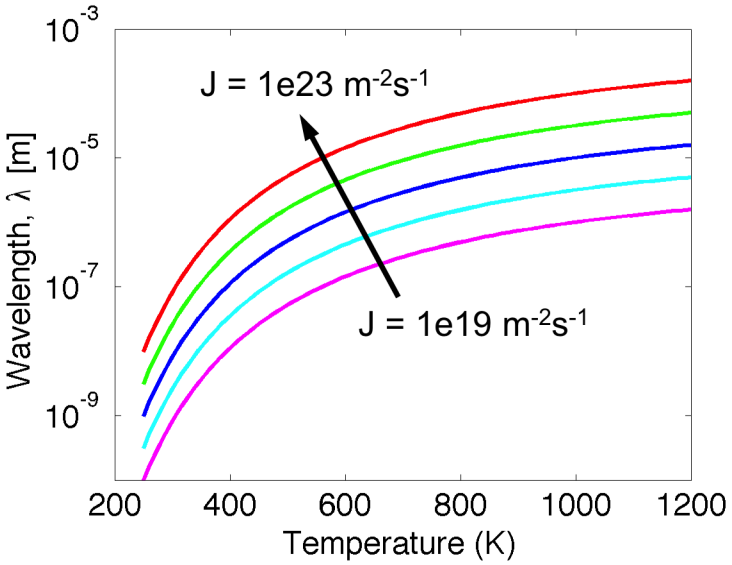

Figure 5.4: Wavelength scale for different values of K and J.

the insulator rings of Hall thrusters at the mm-scale[14]. The latter case likely involved the influence of stress effects due to plasma bombardment and thermal conditions. These experimental observations demonstrate the variety of size scales that may result from plasma exposure as surface features develop.

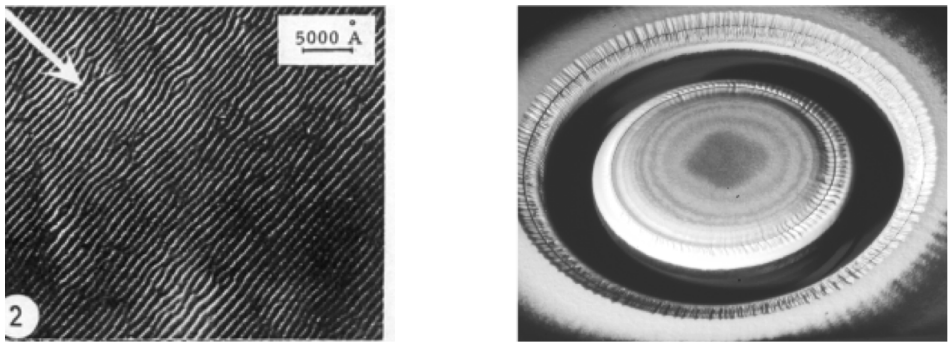

(a) (b)

Figure 5.5: Comparison of ripple formations observed on plasma-facing materials. (a) nm-scale ripples from Navez, et. al.[42] (b) mm-scale ripples found in a BPT-4000 Hall thruster, 25 cm in diameter, after 10,400 hours of operation[14].

5.4 Phenomenological Model of Rough Surface Evolution

In modeling the evolution of rough surfaces, experimental results presented in Section 4.4 lead to two main assumptions regarding the relationship between surface roughness and fluence:

1. $d\varepsilon \propto \varepsilon \cdot d\Phi$
2. $dS \propto d\varepsilon$

Under the first assumption, the change in roughness $d\varepsilon$ is proportional to the roughness itself multiplied by the change in fluence, where the fluence is $\Phi = \phi t$. This relationship can be expressed using a linear constant λ, which leads to a differential equation that may be solved to express the roughness as a function of fluence.

$$d\varepsilon = -\lambda\varepsilon d\Phi \tag{5.45}$$

$$\frac{d\varepsilon}{d\Phi} = -\lambda\varepsilon \tag{5.46}$$

$$\Rightarrow \varepsilon = \varepsilon_0 e^{-\lambda\Phi} \tag{5.47}$$

The second assumption indicates that the change in sputtering yield dS is proportional to the change in roughness. This relationship leads to an expression mediated by a constant K, which can be differentiated with respect to the fluence and solved to produce and equation for the sputtering yield.

$$dS = K d\varepsilon \tag{5.48}$$

$$\frac{dS}{d\Phi} = K\frac{d\varepsilon}{d\Phi} = K\left(-\lambda\varepsilon_0 e^{-\lambda\Phi}\right) \tag{5.49}$$

$$\int_{S_0}^{S} dS = -\lambda K \varepsilon_0 \int_0^{\Phi} e^{-\lambda\Phi} d\Phi \tag{5.50}$$

$$S - S_0 = +\lambda \frac{K\varepsilon_0}{\lambda} \left(1 - e^{-\lambda\Phi}\right) \tag{5.51}$$

$$S = S_0 + K\varepsilon_0 \left(1 - e^{-\lambda\Phi}\right) \tag{5.52}$$

Therefore, the sputtering yield as a function of plasma fluence for a particular micro-architectured surface may be modeled as a saturation curve.

5.5 Modeling of Sputtering Yield Transience

Equation (5.52) may be used to fit a transient yield curve to the experimentally observed data in this study. The saturation curve is fit to the data by defining $K = S_\infty - S_0$, where S_0 is the initial sputtering yield of the textured surface, and the S_∞ is the value at which the curve converges, which corresponds to the yield of a flat surface of the material.

$$S(\phi t) = S_0 + \varepsilon_0(S_\infty - S_0)(1 - e^{-\phi t/\tau_0}) \tag{5.53}$$

Here τ_0 is a parameter that uniquely quantifies the particular surface texture.

This model is displayed in Figure 5.6 with the plotted yield data points for Sample C at various fluence levels. It can be seen that this curve, calculated using the simulated roughness at the corresponding fluence, can be fit quite well to the data.

The height evolution of a surface that experiences ballistic deposition can be simply modeled using a relaxation contribution from a linear damping term, which simulates ballistic deposition through the filling in of troughs and the erosion of the dendrite tips, along with an additional erosive term corresponding to the net sputtering yield.

$$\frac{\partial h}{\partial t} = -\alpha h_s - \beta S(\varepsilon) \tag{5.54}$$

The damping coefficient, α, is multiplied by the standardized height profile, $h_s = h - h_{average}$.

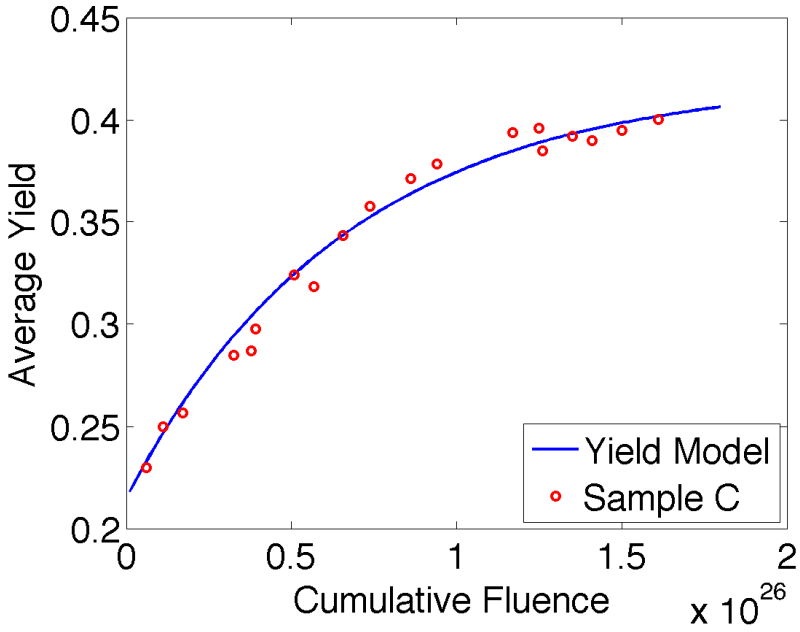

Figure 5.6: Yield data for Sample C and model curve fit.

Figure 5.7 shows the simulated surface profile evolution of an initially rough surface, modeled as dendritic bumps. It can be seen that as the roughness decreases, more rapid erosion is apparent through the spacing at successive time steps, which is expected with an erosion term that is inversely proportional to the roughness. Physically, this represents the decreased rate of ballistic deposition as the surface features are flattened through erosion.

The relationship between fluence and surface roughness allows the transient yield equation to be recast in terms of roughness ε as $S(\varepsilon) = S_0 + (S_\infty - S_0)(1 - e^{-\tau(\varepsilon)/\tau_0})$, where $\tau(\varepsilon) = \frac{1}{\varepsilon}$. Calculating the RMS roughness of the simulated surface profile allows the roughness evolution to be compared to the yield evolution to observe their relationship, seen in Figure 5.8. It can be seen that roughness progresses in an inversely proportional manner to the fluence, while the yield exhibits an exponential saturation curve as the surface features are eroded and roughness decreases.

The fitting parameter τ_0 can be determined from the roughness evolution curve by obtaining the x-intercept of the line tangent to the early portion of the roughness curve. This value corresponds to the fluence that may be used for τ_0 in equation (5.53). Therefore, tracking the

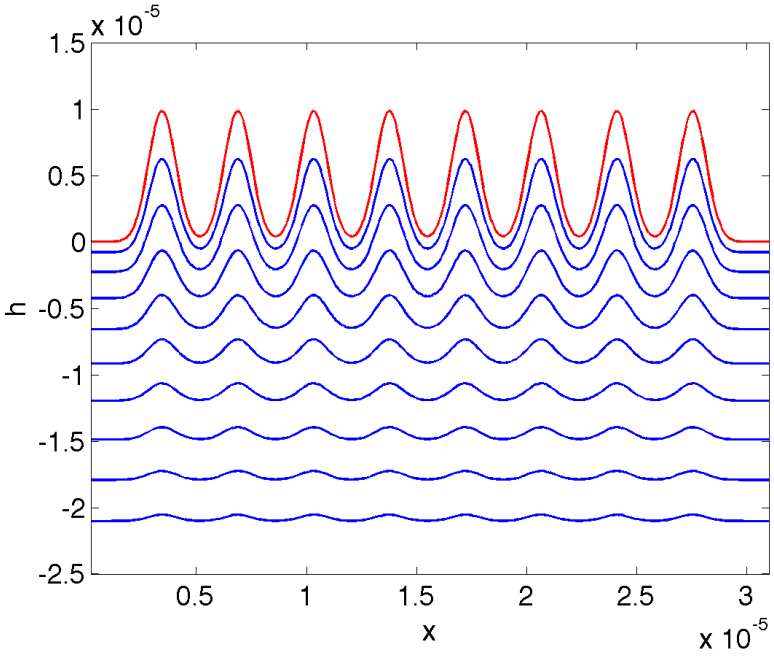

Figure 5.7: Evolution of the surface using simplified height evolution model.

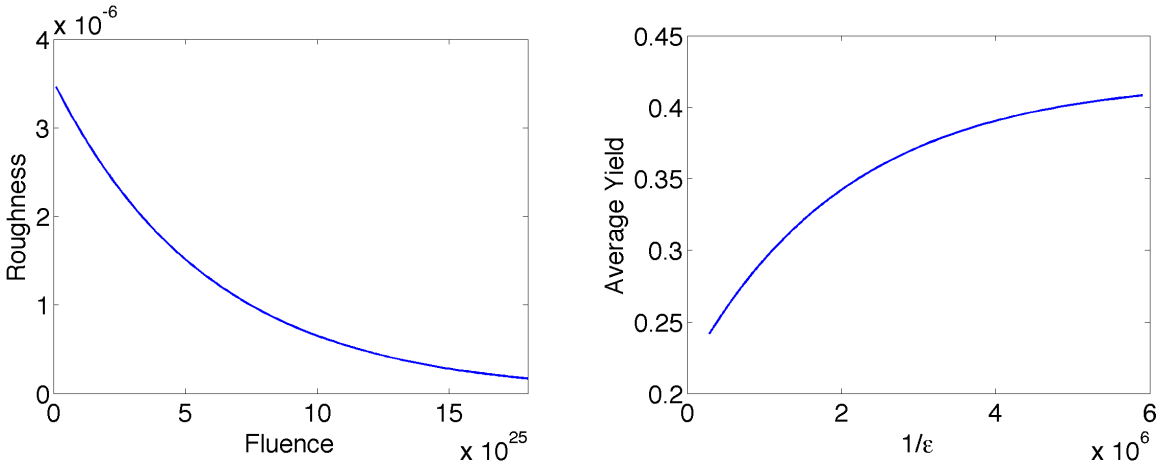

(a) (b)

Figure 5.8: (a) Roughness evolution. (b) Yield as a function of roughness.

roughness evolution can provide an important characterization tool for micro-architectured materials. The quantification of surface evolution for material surfaces offers an avenue for future research that can provide a better understand how surface architecturing improves the behavior of a material under plasma bombardment.

CHAPTER 6

Numerical simulations of surface erosion

6.1 Front-tracking with splines

6.1.1 Geometric Surface Modeling

The surface of a material may be expressed as a parametric curve, modeled using cubic splines. This begins by selecting an initial nodal configuration to express the unexposed surface of a material, perhaps with some initial perturbation to induce evolution, such as a sine wave. In this case, cubic Hermite splines are used, with parameter u ranging from 0 to 1 for each segment between nodes. The equation of a curved surface segment is represented as follows:

$$\boldsymbol{r}_i(u) = (2u^3 - 3u^2 + 1)\boldsymbol{P}_i + (-2u^3 + 3u^2)\boldsymbol{P}_{i+1} + (u^3 - 2u^2 + u)\boldsymbol{T}_i + (u^3 - u^2)\boldsymbol{T}_{i+1} \quad (6.1)$$

where $\boldsymbol{P}_i$ is the i^{th} node of the segment and $\boldsymbol{T}_i$ is the tangent vector at $\boldsymbol{P}_i$. The composite cubic spline curve represents the surface profile, and is used to simulate the evolution of the surface geometry as it evolves from the energy of incoming ions.

To model the surface, a cubic Hermite spline, $\boldsymbol{r}(u)$, is defined over the unit interval $u \in [0, 1]$, by the following polynomial, given a segment starting point, P_k, and tangent, T_k,

as well as the ending point, P_{k+1}, and tangent, T_{k+1}:

$$[\boldsymbol{r}(u)] = \begin{bmatrix} u^3 & u^2 & u & 1 \end{bmatrix} \begin{bmatrix} 2 & -2 & \gamma_k & \gamma_k \\ -3 & 3 & -2\gamma_k & -\gamma_k \\ 0 & 0 & \gamma_k & 0 \\ 1 & 0 & 0 & 0 \end{bmatrix} \begin{bmatrix} P_k \\ P_{k+1} \\ T_k \\ T_{k+1} \end{bmatrix} \tag{6.2}$$

where γ is a parameter determined by the chord length, c.

$$\gamma_k = c_k^{\alpha} \qquad \alpha = \begin{cases} 0 & \text{uniform} \\ 0.5 & \text{centripetal} \\ 1 & \text{chordal} \end{cases} \tag{6.3}$$

The chordal and centripetal implementations prevent self intersections.

Its derivatives with respect to the parameter are found as follows:

$$\boldsymbol{r}_{,u}(u) = \begin{bmatrix} 3u^2 & 2u & 1 \end{bmatrix} \begin{bmatrix} 2 & -2 & \gamma_k & \gamma_k \\ -3 & 3 & -2\gamma_k & -\gamma_k \\ 0 & 0 & \gamma_k & 0 \end{bmatrix} \begin{bmatrix} P_k \\ P_{k+1} \\ T_k \\ T_{k+1} \end{bmatrix} \tag{6.4}$$

$$\boldsymbol{r}_{,uu}(u) = \begin{bmatrix} 6u & 2 \end{bmatrix} \begin{bmatrix} 2 & -2 & \gamma_k & \gamma_k \\ -3 & 3 & -2\gamma_k & -\gamma_k \end{bmatrix} \begin{bmatrix} P_k \\ P_{k+1} \\ T_k \\ T_{k+1} \end{bmatrix} \tag{6.5}$$

$$\boldsymbol{r}_{,uuu}(u) = [6]\begin{bmatrix} 2 & -2 & \gamma_k & \gamma_k \end{bmatrix}\begin{bmatrix} P_k \\ P_{k+1} \\ T_k \\ T_{k+1} \end{bmatrix} \tag{6.6}$$

6.1.2 Spline Design

It is desired to produce a spline with C^2 continuity. Using the Hermite segment, the tangents at the end nodes are chosen such that the second parametric derivative is continuous.

Continuity of the second parametric derivative at the k^{th} node is achieved by setting $\boldsymbol{r}_{,uu}(u_k)$ for the two adjacent segments equal in the following way:

$$[6 \;\; 2]\begin{bmatrix} 2 & -2 & \gamma_{k-1} & \gamma_{k-1} \\ -3 & 3 & -2\gamma_{k-1} & -\gamma_{k-1} \end{bmatrix}\begin{bmatrix} P_{k-1} \\ P_k \\ T_{k-1} \\ T_k \end{bmatrix} = [0 \;\; 2]\begin{bmatrix} 2 & -2 & \gamma_k & \gamma_k \\ -3 & 3 & -2\gamma_k & -\gamma_k \end{bmatrix}\begin{bmatrix} P_k \\ P_{k+1} \\ T_k \\ T_{k+1} \end{bmatrix} \tag{6.7}$$

Rearranging the relation separates the tangent and position vectors for each set.

$$[\gamma_{k-1} \;\; 2(\gamma_k + \gamma_{k-1}) \;\; \gamma_k]\begin{bmatrix} T_{k-1} \\ T_k \\ T_{k+1} \end{bmatrix} = 3[1 \;\; 0 \;\; -1]\begin{bmatrix} P_{k-1} \\ P_k \\ P_{k+1} \end{bmatrix} \tag{6.8}$$

Using the above relation, global matrices may be assembled as follows to solve for the necessary tangents needed to achieve C^2 continuity across the spline. The point positions are

given, so the tangents are the only unknowns.

$$\begin{bmatrix} \gamma_0 & 2(\gamma_1+\gamma_0) & \gamma_1 & \dots & 0 & 0 & 0 \\ 0 & \gamma_1 & 2(\gamma_2+\gamma_1) & \gamma_2 & \dots & 0 & 0 \\ \dots & & & & & & \\ 0 & 0 & 0 & \dots & \gamma_{n-2} & 2(\gamma_{n-1}+\gamma_{n-2}) & \gamma_{n-1} \end{bmatrix} \begin{bmatrix} T_0 \\ T_1 \\ T_2 \\ \dots \\ T_{n-2} \\ T_{n-1} \\ T_n \end{bmatrix}$$

$$= 3 \begin{bmatrix} 1 & 0 & -1 & \dots & 0 & 0 & 0 \\ 0 & 1 & 0 & -1 & \dots & 0 & 0 \\ \dots & & & & & & \\ 0 & 0 & 0 & \dots & 1 & 0 & -1 \end{bmatrix} \begin{bmatrix} P_0 \\ P_1 \\ P_2 \\ \dots \\ P_{n-2} \\ P_{n-1} \\ P_n \end{bmatrix} \tag{6.9}$$

The obtained tangents may then be used with the known points to generate the complete Hermite spline with curvature continuity. These values are applied to generate $\boldsymbol{r}(u)$ according to Equation (6.2).

The arc length s along the curve may be expressed as a function of the parameter u at a time t. Therefore, the arc length of the entire segment (i.e., $u = 1$) is found as follows:

$$s(1,t) = \int_0^1 \sqrt{\boldsymbol{r}_{,u}(u,t) \cdot \boldsymbol{r}_{,u}(u,t)}\, du \tag{6.10}$$

The jacobian of the transformation between u and s, along with its derivatives with respect

to the parameter are:

$$\mathbb{J} = \frac{\partial s}{\partial u} = \sqrt{\boldsymbol{r}_{,u}(u,t) \cdot \boldsymbol{r}_{,u}(u,t)} \tag{6.11}$$

$$\mathbb{J}_{,u} = \frac{\boldsymbol{r}_{,u} \cdot \boldsymbol{r}_{,uu}}{\mathbb{J}} \tag{6.12}$$

$$\mathbb{J}_{,uu} = \frac{1}{\mathbb{J}} \left[\boldsymbol{r}_{,uu} \cdot \boldsymbol{r}_{,uu} + \boldsymbol{r}_{,u} \cdot \boldsymbol{r}_{,uuu} - \mathbb{J}_{,u} \right] \tag{6.13}$$

$$\mathbb{J}_{,uuu} = \frac{1}{\mathbb{J}} \left[3\boldsymbol{r}_{,uu} \cdot \boldsymbol{r}_{,uuu} + \boldsymbol{r}_{,u} \cdot \boldsymbol{r}_{,uuuu} \right] - \frac{2\mathbb{J}_{,uu}}{\mathbb{J}} \tag{6.14}$$

The derivatives of a curve with respect to the parameter is not equivalent to its derivative with respect to arc length. The latter is found by dividing the former by the jacobian of the curve. Derivatives with respect to the arc length are obtained by chain rule:

$$\boldsymbol{r}_{,s} = \frac{\boldsymbol{r}_{,u}}{\mathbb{J}} \tag{6.15}$$

$$\boldsymbol{r}_{,ss} = \frac{\boldsymbol{r}_{,uu}}{\mathbb{J}^2} - \mathbb{J}_{,u} \frac{\boldsymbol{r}_{,u}}{\mathbb{J}^3} \tag{6.16}$$

$$\boldsymbol{r}_{,sss} = \frac{\boldsymbol{r}_{,uuu}}{\mathbb{J}^3} - \frac{\boldsymbol{r}_{,u}\mathbb{J}_{,uu}}{\mathbb{J}^4} - 3\frac{\mathbb{J}_{,u}}{\mathbb{J}^2} \left(\frac{\boldsymbol{r}_{,uu}}{\mathbb{J}^2} - \mathbb{J}_{,u} \frac{\boldsymbol{r}_{,u}}{\mathbb{J}^3} \right) \tag{6.17}$$

$$\boldsymbol{r}_{,ssss} = \frac{\boldsymbol{r}_{,u}}{\mathbb{J}^5} \left[\frac{10}{\mathbb{J}} \mathbb{J}_{,u}\mathbb{J}_{,uu} - \frac{15}{\mathbb{J}^2} \mathbb{J}_{,u}^3 - \mathbb{J}_{,uuu} \right] + \frac{\boldsymbol{r}_{,uu}}{\mathbb{J}^5} \left[\frac{15}{\mathbb{J}} \mathbb{J}_{,u}^2 - 4\mathbb{J}_{,uu} \right] \tag{6.18}$$

$$- \frac{6}{\mathbb{J}^5} \mathbb{J}_{,u} \boldsymbol{r}_{,uuu} + \frac{\boldsymbol{r}_{,uuuu}}{\mathbb{J}^4} \tag{6.19}$$

The magnitude of the geometric curvature, κ, is equal to the magnitude of the second geometric derivative, $\boldsymbol{r}_{,ss}$.

6.1.3 Differential Geometry

From the results in the preceding section, differential geometry may be used to determine important quantities used to describe the surface and calculate its evolution. In particular, the surface normal and surface curvature must be known to calculate the normal velocity according to the evolution equation. Describing the surface in two dimensions as a parametric

curve, $\boldsymbol{r}(t)$, the following relations may be obtained:

$$\dot{\boldsymbol{r}} = \frac{d\boldsymbol{r}}{du} = \frac{d\boldsymbol{r}}{ds}\frac{ds}{du} = \overline{T}\dot{s} \tag{6.20}$$

Therefore it can be seen that $\|\dot{\boldsymbol{r}}\| = \dot{s}$. The unit tangent vector, $\overline{T}(u)$, is defined as follows:

$$\overline{T}(u) = \lim_{\Delta u \to 0} \frac{\Delta \boldsymbol{r}(u)}{\|\Delta \boldsymbol{r}(u)\|} = \lim_{\Delta u \to 0} \frac{\Delta \boldsymbol{r}(u)}{\Delta s} = \frac{d\boldsymbol{r}}{ds}\frac{\dot{\boldsymbol{r}}}{\|\dot{\boldsymbol{r}}\|} \tag{6.21}$$

$$\dot{\overline{T}}(u) = \frac{d\overline{T}}{du} = \frac{d\overline{T}}{ds}\frac{ds}{du} = \kappa\overline{N}\dot{s} \tag{6.22}$$

since

$$\frac{d\overline{T}}{ds} = \left\|\frac{d\overline{T}}{ds}\right\| \overline{N} = \kappa(u)\overline{N} \tag{6.23}$$

Therefore

$$\ddot{\boldsymbol{r}} = \frac{d\left(\dot{s}\overline{T}\right)}{du} = \ddot{s}\overline{T} + \dot{s}\frac{d\overline{T}}{ds}\frac{ds}{du} = \ddot{s}\overline{T} + \dot{s}\kappa\overline{N}\dot{s} = \ddot{s}\overline{T} + \dot{s}^2\kappa\overline{N} \tag{6.24}$$

Taking the cross product:

$$\dot{\boldsymbol{r}} \times \ddot{\boldsymbol{r}} = \left(\dot{s}\overline{T}\right) \times \left(\ddot{s}\overline{T} + \dot{s}^2\kappa\overline{N}\right) = \dot{s}^3\kappa\overline{B} \tag{6.25}$$

Where $\overline{B}$ is the bi-normal vector, forming an orthogonal triad with $\overline{N}$ and $\overline{T}$. From Equation (6.25), it is known that $\overline{B}$ is a unit vector in the direction of $\dot{\boldsymbol{r}} \times \ddot{\boldsymbol{r}}$. Therefore:

$$\overline{B} = \frac{\dot{\boldsymbol{r}} \times \ddot{\boldsymbol{r}}}{\|\dot{\boldsymbol{r}} \times \ddot{\boldsymbol{r}}\|} \implies \dot{s}^3\kappa = \|\dot{\boldsymbol{r}} \times \ddot{\boldsymbol{r}}\| \tag{6.26}$$

Solving for κ:

$$\kappa = \frac{\|\dot{\boldsymbol{r}} \times \ddot{\boldsymbol{r}}\|}{\dot{s}^3} = \frac{\|\dot{\boldsymbol{r}} \times \ddot{\boldsymbol{r}}\|}{\|\dot{\boldsymbol{r}}\|^3} \tag{6.27}$$

Knowing that $\overline{B}$ forms an orthogonal tried with $\overline{N}$ and $\overline{T}$, the normal vector can be determined in terms of the curve, $\boldsymbol{r}(t)$:

$$\overline{N}(u) = \overline{B} \times \overline{T} = \frac{\dot{\boldsymbol{r}} \times \ddot{\boldsymbol{r}}}{\|\dot{\boldsymbol{r}} \times \ddot{\boldsymbol{r}}\|} \times \frac{\dot{\boldsymbol{r}}}{\|\dot{\boldsymbol{r}}\|} = \frac{\dot{\boldsymbol{r}} \times \ddot{\boldsymbol{r}} \times \dot{\boldsymbol{r}}}{\|\dot{\boldsymbol{r}} \times \ddot{\boldsymbol{r}} \times \dot{\boldsymbol{r}}\|} \tag{6.28}$$

6.1.4 Spline Evolution

The normal velocity expressed by equation (5.25) is a function of the approach angle of incoming ions, φ, and the curvature, κ. It can be expressed for a 1-D surface as follows:

$$v_n(\varphi, \kappa) = \frac{J}{n} Y_0(\varphi)[\cos\varphi - \kappa\Gamma(\varphi)a] \tag{6.29}$$

More simply, this may be expressed as the product of the flux and yield vectors. The normal velocity is found as follows:

$$v_n = \vec{J} \cdot \vec{Y}(u) \tag{6.30}$$

Where J is the flux of the incoming ions normal to the surface, and $\vec{Y}(u)$ is the sputtering yield in the normal direction, taking into account curvature effects:

$$\vec{Y}(u) = \frac{Y_0(\varphi)}{n} \left(\overline{N} - a\Gamma(\varphi)\vec{\kappa}\right) \tag{6.31}$$

Y_0 is the yield of a flat surface, and therefore dependent only on the ion energy and angle of incidence. Therefore, it follows that:

$$v_n = \frac{Y_0}{n} \left(\vec{J} \cdot \overline{N} - a\Gamma \vec{J} \cdot \vec{\kappa}\right) = \frac{JY_0}{n} \left(\cos\varphi - \frac{a\Gamma(\varphi)}{R}\right) \tag{6.32}$$

This result comes from the fact that the magnitude of the curvature vector is the inverse of the radius of curvature:

$$|\vec{\kappa}| = \frac{1}{R} \tag{6.33}$$

The curvature vector, $\vec{\kappa}$, points in the direction of the radius of curvature, while the normal vector $\overline{N}$ points in the positive z direction. This distinction allows for the erosive contribution of the incoming ions along the surface normal, as well as the separate curvature contribution. To determine the velocity of the curve at each time step, a finite element approximation is

Figure 6.1: Curvature and Normal vector orientation

implemented. Integrated over the arc length, the weak form may be expressed as follows:

$$\int_0^1 v_n(u)\tilde{v}_n(u)\left|\frac{ds}{du}\right| du = \int_0^1 \vec{J}\cdot\vec{Y}(u)\tilde{v}_n(u)\left|\frac{ds}{du}\right| du \tag{6.34}$$

$$\int_0^1 v_n(u)\tilde{v}_n(u)\mathbb{J}du = \int_0^1 \vec{J}\cdot\vec{Y}(u)\tilde{v}_n(u)\mathbb{J}du \tag{6.35}$$

Where $v_n(u)$ is the trial function and $\tilde{v}_n(u)$ is the test function.

$$v_n(u) = N(u)\cdot W = \begin{bmatrix} 1-u & u \end{bmatrix}\begin{bmatrix} W_0 \\ W_1 \end{bmatrix} \tag{6.36}$$

$$\tilde{v}_n(u) = N(u)\cdot \widetilde{W} = \begin{bmatrix} 1-u & u \end{bmatrix}\begin{bmatrix} \widetilde{W_0} \\ \widetilde{W_1} \end{bmatrix} \tag{6.37}$$

Where $N(u)$ is the shape function matrix, posessing linear functions, and W is the nodal velocity matrix.

The relation may therefore be expressed in the following way:

$$\begin{bmatrix}\widetilde{W}_0 & \widetilde{W}_1\end{bmatrix}\int_0^1 \begin{bmatrix}1-u \\ u\end{bmatrix}\begin{bmatrix}1-u & u\end{bmatrix}\mathbb{J}(u)du\begin{bmatrix}W_0 \\ W_1\end{bmatrix} = \tag{6.38}$$
$$\begin{bmatrix}\widetilde{W}_0 & \widetilde{W}_1\end{bmatrix}\int_0^1 \begin{bmatrix}1-u \\ u\end{bmatrix}\vec{J}\cdot\vec{Y}(u)\mathbb{J}(u)du$$

Gauss-Legendre quadrature may be used to evaluate the integrals. Therefore, the relation may be computed as the summation over the quadrature points:

$$\begin{bmatrix}\widetilde{W}_0 & \widetilde{W}_1\end{bmatrix}\begin{bmatrix}W_0 \\ W_1\end{bmatrix}\sum_q \begin{bmatrix}1-u_q \\ u_q\end{bmatrix}\begin{bmatrix}1-u_q & u_q\end{bmatrix}|\boldsymbol{r}_{,u}(u_q)|\,w_q = \tag{6.39}$$
$$\begin{bmatrix}\widetilde{W}_0 & \widetilde{W}_1\end{bmatrix}\sum_q \begin{bmatrix}1-u_q \\ u_q\end{bmatrix}\vec{J}\cdot\vec{Y}(u_q)\,|\boldsymbol{r}_{,u}(u_q)|\,w_q$$

The integrals correspond to the stiffness K and force F matrix, respectively. The expression may be written as:

$$\widetilde{W}KW = \widetilde{W}F \tag{6.40}$$

$$KW = F \tag{6.41}$$

Solving for the nodal velocities:

$$W = K^{-1}F \tag{6.42}$$

These velocities may be used to evolve the original set of nodal points:

$$dP = Wdt \tag{6.43}$$

$$P_{new} = P_{old} + dP \tag{6.44}$$

The new nodal positions may be used to solve for the necessary tangents for C^2 continuity, and subsequently generate the spline at the new time step.

6.1.5 Results

A program was generated in MATLAB to plot a spline that represents the surface profile of a material under ion bombardment. The evolution equation for the normal velocity was then applied to the spline over multiple time steps to illustrate the evolution of the surface. Figure 6.2 shows the result of this numerical implementation over a short time span, with generally positive results. It can be seen that smooth evolution occurs, and greater erosion is apparent in troughs relative to the crests, which is consistent to the theory. Extending

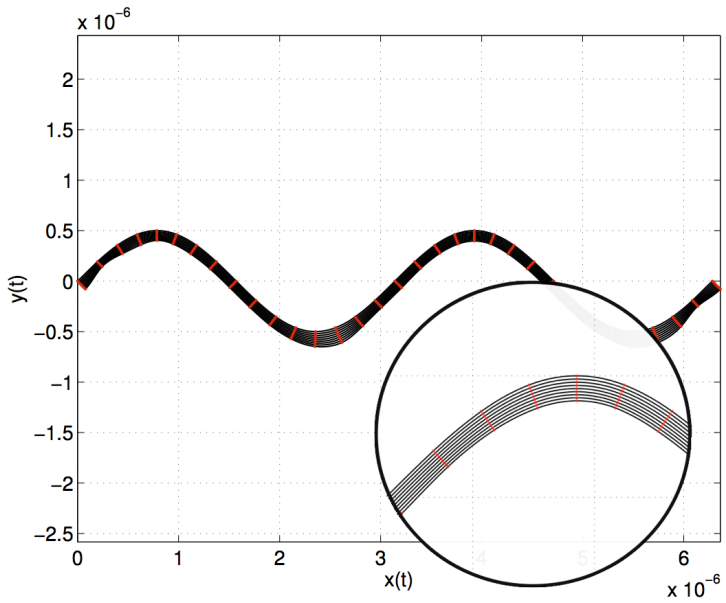

Figure 6.2: Plot of spline evolution for a short time span, with zoomed inset. Smooth evolution is observed for the sinusoidal profile.

the timeframe of evolution to longer spans, however, introduced some problems. As the time step increased, small perturbations arose at the nodes, which began to cause kinks to occur in the profile. Because of the nature of cubic splines, small irregularities can cause instabilities to quickly propagate. Figure 6.3 shows the unstable development of the surface profile. The evolution begins smoothly, but as irregularities come about in the contours, the

spline becomes unstable very quickly. Because of this stability issue, it became apparent that

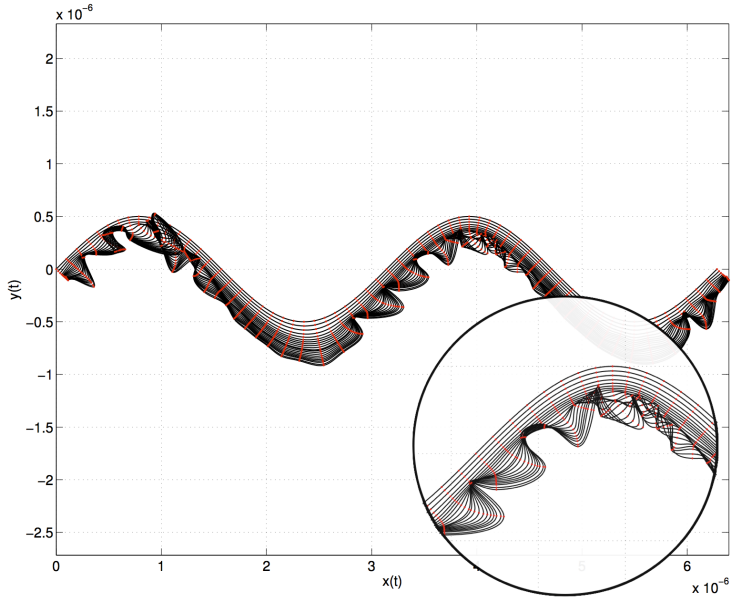

Figure 6.3: Plot of spline evolution for a longer time span, with zoomed inset. Unstable spline behavior occurs at higher time steps, after initially smooth evolution.

cubic splines were not the most effective method for modeling surface evolution over long time spans. The Fast Fourier Transform (FFT) method to numerically model surface profiles was a favorable option, as it allowed for simple implementation of the evolution equation with the ability to provide stable time stepping.

6.2 Fast Fourier Transform (FFT)-based methods

To address the stability issues encountered by the spline-modeling technique, an alternate method of modeling the surface was explored. Additionally, the spline-based method was limited to 1-dimension and was computationally expensive, so it was desired to produce a model that possessed fewer limitations in modeling the surface profile evolution. The following sections introduce the FFT numerical method used for the simulations, in which a defined surface profile is evolved in Fourier space according to the governing equation.

When looking at perturbations of the uniform profile

$$h(x,y,t) = -v_0 t + \bar{h}(x,y,t) \tag{6.45}$$

the height equation for a surface may be expressed as the erosion term and the contribution $\bar{h}$. By means of a Galilean transformation, the velocity term may be absorbed in the temporal derivative. To simplify notation, the expression is considered for normal ion incidence such that the generalized height evolution may be written as follows[59]:

$$\frac{\partial \bar{h}}{\partial t} = -\alpha \bar{h}_s - \frac{Fa}{2}\nabla^2 \bar{h} - \frac{Fa_\alpha}{2}\left(\nabla \bar{h}\right)^2 - K\nabla^4 \bar{h} \tag{6.46}$$

Omitting the nonlinear term, the general form of the damped linear equation is written as follows[9]:

$$\frac{\partial \bar{h}}{\partial t} = -\alpha \bar{h}_s - \frac{Fa}{2}\nabla^2 \bar{h} - K\nabla^4 \bar{h} \tag{6.47}$$

It is desired to convert this equation to Fourier space. If $u(x)$ is a function sampled at n discrete points $x_i \in h, 2h, ..., ih, ..., 2\pi - h, 2\pi$ and $h = 2\pi/n$ in real space, then the Fast Fourier Transform (FFT) is expressed as:

$$\mathrm{FFT}\left(u_j\right) \equiv \hat{u}_k \qquad \text{where } k \in \frac{-n}{2} + 1, ..., \frac{n}{2} \tag{6.48}$$

This operation may be carried out using MATLAB's FFT function. The Fourier transform of derivatives can easily be found subsequently from $\hat{u}_k$:

$$\mathrm{FFT}\left(\frac{\partial^\nu u_j}{\partial x^\nu}\right) \equiv (ik)^\nu \hat{u}_k \tag{6.49}$$

Therefore, differentiation in real space becomes multiplication in Fourier space. After performing this operation, taking the inverse fast Fourier Transform (IFFT) produces the

solution in real space, which may also be performed using MATLAB's IFFT function.

The numerical method was initially applied for the 1-dimensional case in order to simplify the calculations. Once this was accomplished, the 2-dimensional case was considered. The following outlines the numerical method for the 2-dimensional case. Applying the generalized linear form of Equation (6.47) in 2-dimensions results in the following equation:

$$\frac{\partial \bar{h}}{\partial t} = -\alpha \bar{h}_s - \frac{Fa}{2}\left(\bar{h}_{xx} + \bar{h}_{yy}\right) - K\left(\bar{h}_{xxxx} + \bar{h}_{yyyy} + 2\bar{h}_{xxyy}\right) \tag{6.50}$$

The surface height is converted to Fourier space in MATLAB using the FFT2 function for 2-dimensional space. To model the directional dependence of the expression, it is necessary to introduce the indices k_x and k_y, as the derivatives are applied across both dimensions. The result is expressed as the product of $\hat{h}$ and powers of the index k:

$$\frac{\partial \hat{h}}{\partial t} = -\alpha(\hat{h} - h_A) - \frac{Fa}{2}\left((ik_x)^2\hat{h} + (ik_y)^2\hat{h}\right) - K\left((ik_x)^4\hat{h} + (ik_y)^4\hat{h} + 2(ik_x)^2(ik_y)^2\hat{h}\right) \tag{6.51}$$

The linear equation may be solved in Fourier space using the Backward Euler method, which numerically solves the ordinary differential equation implicitly. In MATLAB, the result may be calculated in Fourier space for each time step, then converted back to real

space using the IFFT2 function.

$$\frac{\hat{h}^{n+1}-\hat{h}^{n}}{\Delta t}=-\alpha\left(\hat{h}^{n+1}-h_{A}\right)-\frac{Fa}{2}\left[(ik_{x})^{2}+(ik_{y})^{2}\right]\hat{h}^{n+1} - K\left[(ik_{x})^{4}+(ik_{y})^{4}+2(ik_{x})^{2}(ik_{y})^{2}\right]\hat{h}^{n+1} \tag{6.52}$$

$$\hat{h}^{n+1}\left[1+\Delta t\alpha+\Delta t\frac{Fa}{2}\left[(ik_{x})^{2}+(ik_{y})^{2}\right] + \Delta tK\left[(ik_{x})^{4}+(ik_{y})^{4}+2(ik_{x})^{2}(ik_{y})^{2}\right]\right]=\hat{h}^{n}+\Delta t\alpha h_{A} \tag{6.53}$$

$$\hat{h}^{n+1}=\frac{\left[\hat{h}^{n}+\Delta t\alpha h_{A}\right]}{\left[1+\Delta t\alpha+\Delta t\frac{Fa}{2}\left[(ik_{x})^{2}+(ik_{y})^{2}\right]+\Delta tK\left[(ik_{x})^{4}+(ik_{y})^{4}+2(ik_{x})^{2}(ik_{y})^{2}\right]\right]} \tag{6.54}$$

Adding the nonlinear term to the evolution equation, the generalized nonlinear form of Equation (6.46) can be expressed in two dimensions as follows:

$$\frac{\partial\bar{h}}{\partial t}=-\alpha h_{s}-\frac{Fa}{2}\left(\bar{h}_{xx}+\bar{h}_{yy}\right)-\frac{Fa_{\alpha}^{2}}{2}\left(\bar{h}_{x}+\bar{h}_{y}\right)^{2}-K\left(\bar{h}_{xxxx}+\bar{h}_{yyyy}+2\bar{h}_{xxyy}\right) \tag{6.55}$$

The expanded expression can be converted to Fourier space using the same method as the previously described, by introducing the directional indices. The nonlinear term computed by taking the convolution integral in Fourier space.

$$\frac{\partial\hat{h}}{\partial t}=-\alpha(\hat{h}-h_{A})-\frac{Fa}{2}(ik)^{2}\hat{h}-\frac{Fa_{\alpha}^{2}}{2}\left(\left[(ik_{x})+(ik_{y})\right]\hat{h}*\left[(ik_{x})+(ik_{y})\right]\hat{h}\right) - K\left((ik_{x})^{4}\hat{h}+(ik_{y})^{4}\hat{h}+2(ik_{x})^{2}(ik_{y})^{2}\hat{h}\right) \tag{6.56}$$

It should be noted that the convolution of two vectors in Fourier space is equal to the Fourier transform of their element-wise product in real space.

$$\left((ik)\hat{h}^{n}*(ik)\hat{h}^{n}\right)=\mathrm{FFT}(\nabla\bar{h}\cdot\nabla\bar{h}) \tag{6.57}$$

To solve for $\nabla\bar{h}$, we must first transform $\bar{h}$ to Fourier space, then take the derivative in

Fourier space before transforming it back to real space:

$$\hat{h} = \mathrm{FFT}(\bar{h}) \tag{6.58}$$

$$\nabla\bar{h} = \mathrm{IFFT}\left((ik)\hat{h}\right) \tag{6.59}$$

This result may be used in Equation (6.57) to express the nonlinear term in Equation (6.56). This method is applied to the nonlinear term of the evolution equation to solve the ODE at each time step.

The nonlinear term requires the solution of the ODE to be performed using a hybrid implicit/explicit method. The Backward Euler (implicit) method cannot be performed because the nonlinear term prevents $\hat{h}^{n+1}$ from being factored out. To solve this problem, all terms are written implicitly except the nonlinear term, which is written explicitly. Applying this to the equation, the following solution is found:

$$\begin{aligned}\frac{\hat{h}^{n+1}-\hat{h}^{n}}{\Delta t} =& -\alpha\left(\hat{h}^{n+1}-h_A\right)-\frac{Fa}{2}\left[(ik_x)^2+(ik_y)^2\right]\hat{h}^{n+1}\\ &-\frac{Fa_\alpha^2}{2}\left(\left[(ik_x)+(ik_y)\right]\hat{h}^{n}*\left[(ik_x)+(ik_y)\right]\hat{h}^{n}\right)\\ &-K\left[(ik_x)^4+(ik_y)^4+2(ik_x)^2(ik_y)^2\right]\hat{h}^{n+1}\end{aligned} \tag{6.60}$$

$$\hat{h}^{n+1} = \frac{\left[\hat{h}^{n}+\Delta t\alpha h_A-\Delta t\frac{Fa_\alpha^2}{2}\left(\left[(ik_x)+(ik_y)\right]\hat{h}^{n}*\left[(ik_x)+(ik_y)\right]\hat{h}^{n}\right)\right]}{\left[1+\Delta t\alpha+\Delta t\frac{Fa}{2}\left[(ik_x)^2+(ik_y)^2\right]+\Delta tK\left[(ik_x)^4+(ik_y)^4+2(ik_x)^2(ik_y)^2\right]\right]} \tag{6.61}$$

This result may be calculated in MATLAB for all time steps, and converted back to real space using the IFFT2 function. The operation is performed over many time steps to simulate the evolution of the surface profile over a specified span.

CHAPTER 7

Numerical Modeling Results

Numerical simulations performed using the FFT numerical method produced a number of useful results that offer insight into the effects of various characteristics of the governing equation. The necessary erosion conditions provided inputs for the evolution equation. The simulations produced contour plots, which depict the surface morphology of an eroded material surface. The contour plots provide a visual representation of the surface patterns that form, as determined from stability requirements of the evolution equation. Additionally, spectral analysis was performed on the surface profile using an FFT, which allowed for a determination of the dominant frequencies present in the surface morphology. A dispersion relation then could be used to identify the dominant wavelengths of the surface features before and after evolution. This analysis allowed for a quantified tracking of the surface features, and an understanding of the stable patterns that emerge over a particular timeframe.

7.1 System behavior in the linear regime

The numerical simulations produced results that could be compared to the analytical results determined according to linear stability analysis. By examining the evolution of the surface under the linear equation, it can be observed how the surface morphology takes on the patterning expected according to linear stability analysis. Figure 7.1 shows the surface contour plots of an initially randomized profile before and after undergoing linear evolution. It can be observed that the evolved surface demonstrates the emergence of an organized ripple pattern.

Taking the FFT of a surface profile provides us with a quantified spectral analysis of the wavelengths that emerge in the surface patterning. This technique was performed on the initial and numerically evolved profiles to observe how linear evolution affects the dominant wavelength of the morphology. Figure 7.2 shows the wavelength spectrum of the initial profile plotted against the evolved profile in both the x and y directions. A black vertical line was added to the plots indicate the analytical solution determined according to stability analysis. It can be seen that in both directions, the initial profile was erratic and had no clear emergence of a dominant wavelength, but as the profile evolved under the linear erosion equation, a peak clearly approaches the analytically determined wavelength.

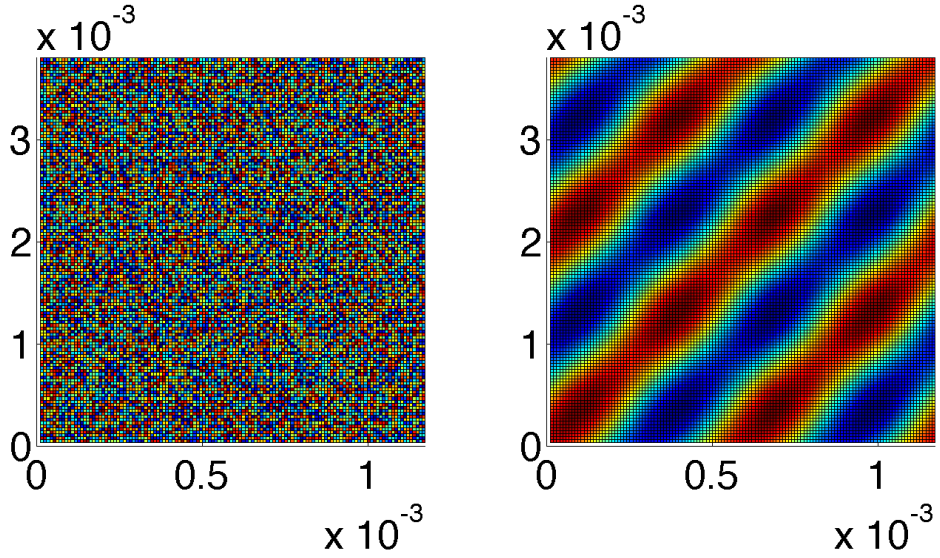

(a) (b)

Figure 7.1: Comparison of evolved surfaces for an initially randomized surface. (a) Original Surface (b) Linear Evolution. $\theta = 45°$.

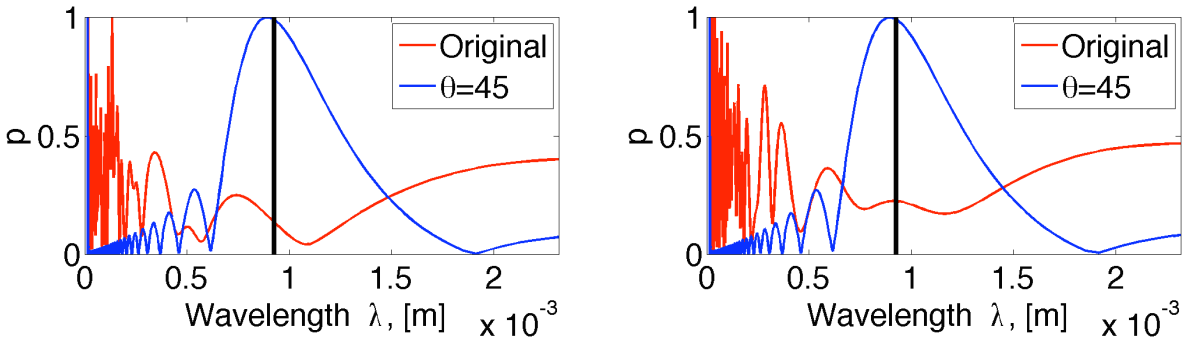

(a) (b)

Figure 7.2: FFT Spectral analysis for linear evolution of a random initial profile, $\theta = 45°$. (a) x-direction (b) y-direction.

7.2 Effects of nonlinearities

The nonlinear form of the equation produces contrasting results to the linear form of the equation, with the nonlinear term excluded. Figure 7.3a shows the 1-dimensional evolution of a particular surface for both the linear and nonlinear case. It can be seen that the nonlinear plot possesses similar periodicity to the linear plot, but with additional undulations in the final profile. This nonlinear patterning is explained visually in Figure 7.3b. The top plot shows the initial pattern, characterized by 4 gaussian "bump" formations, with the next plot down showing the periodic pattern of the evolved surface profile, with a wavelength that corresponds to linear stability analysis of the evolution equation. The next plot down shows the isolated nonlinear term, which clearly has twice the frequency of the linearly evolved profile. With this nonlinear contribution, it can be seen how the patterning of the nonlinear evolution comes about.

The spectral analysis shown in Figure 7.4 corresponds to the evolution shown in Figure 7.3. It can be seen that prior to evolution, the original surface possesses a distinct pattern, which disappears after evolution, performed over 5000 time steps, in both the linear and nonlinear case. Under linear evolution, it can be seen that a peak exists close to the analytically expected result for linear stability, denoted by the black vertical line. A notable observation is that the evolved geometry for the nonlinear case has a dominant wavelength

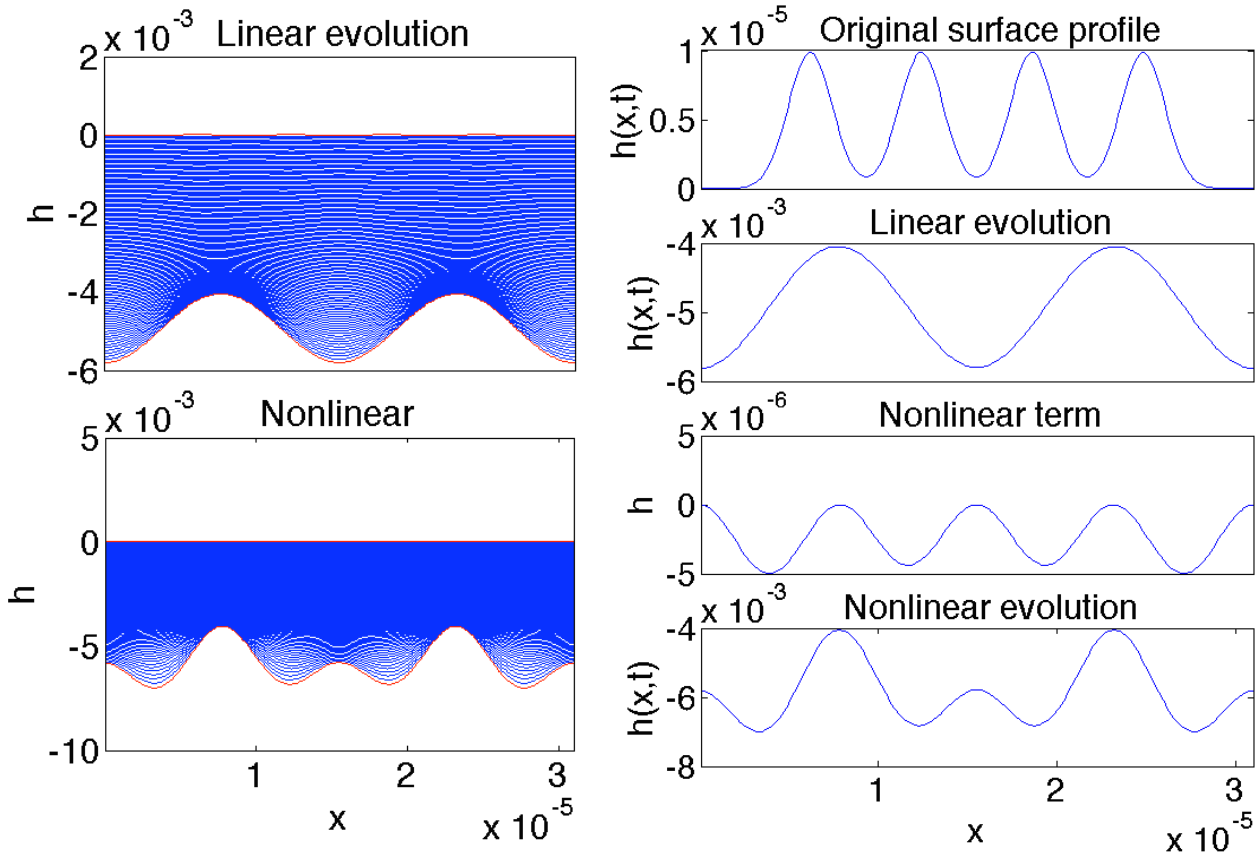

(a) (b)

Figure 7.3: (a) Evolution of a gaussian bump surface profile, linear and nonlinear. (b) Comparison of final surface profiles with the original, with nonlinear term plotted

present that is approximately half the size of the analytical result. There also exists a peak on the nonlinear plot near the analytical result, indicating the presence of the linear morphology in the final patterning, as can be observed in the plot from Figure7.4. An intermediate wavelength spectrum is also displayed, taken after 1680 time steps, and from this it can be observed that the dominant wavelength for both linear and nonlinear evolution were identical, close to the analytical result. This indicates that at earlier time steps, the nonlinear term has little effect, as it has not grown sufficiently to influence the morphology.

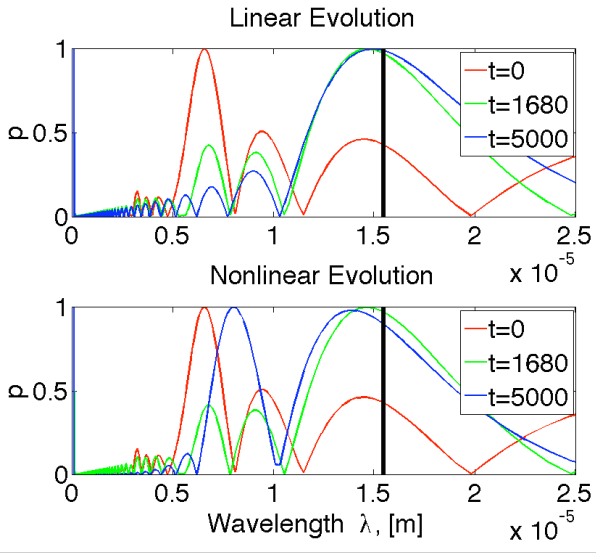

Figure 7.4: Wavelength stability of surface evolution for linear and nonlinear cases

Figure 7.5 shows the deformation of an initially random surface after both linear and nonlinear evolution. The morphologies of both the surfaces show striations that have formed after evolution, however the wavelengths differ in scale. It can be seen that the nonlinear evolution produced wavelengths that are noticeably smaller in size than the linear evolution.

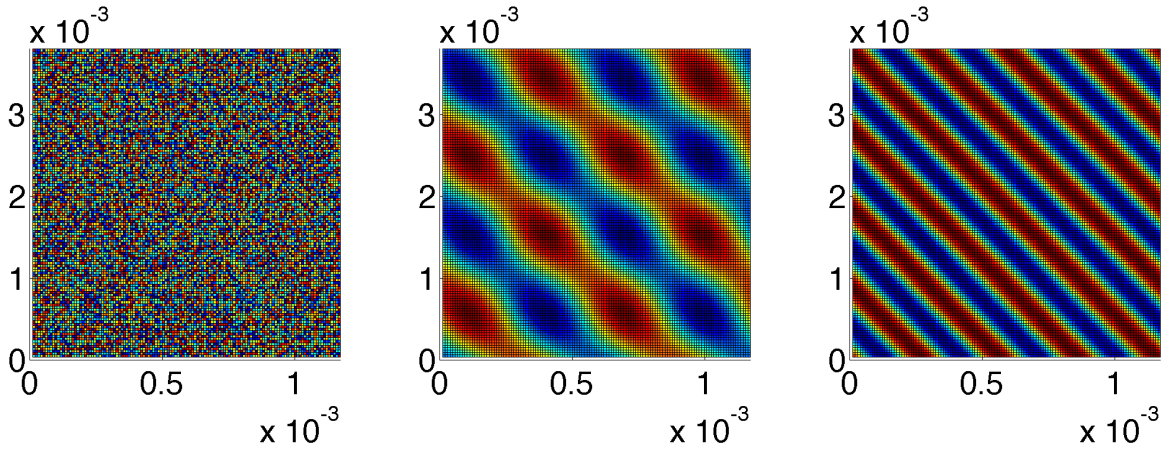

(a) (b) (c)

Figure 7.5: Comparison of evolved surfaces for an initially randomized surface. (a) Original Surface (b) Linear Evolution (c) Nonlinear Evolution. Normal incidence.

The spectral analysis displayed in Figure 7.6 is helpful to quantify the results shown in

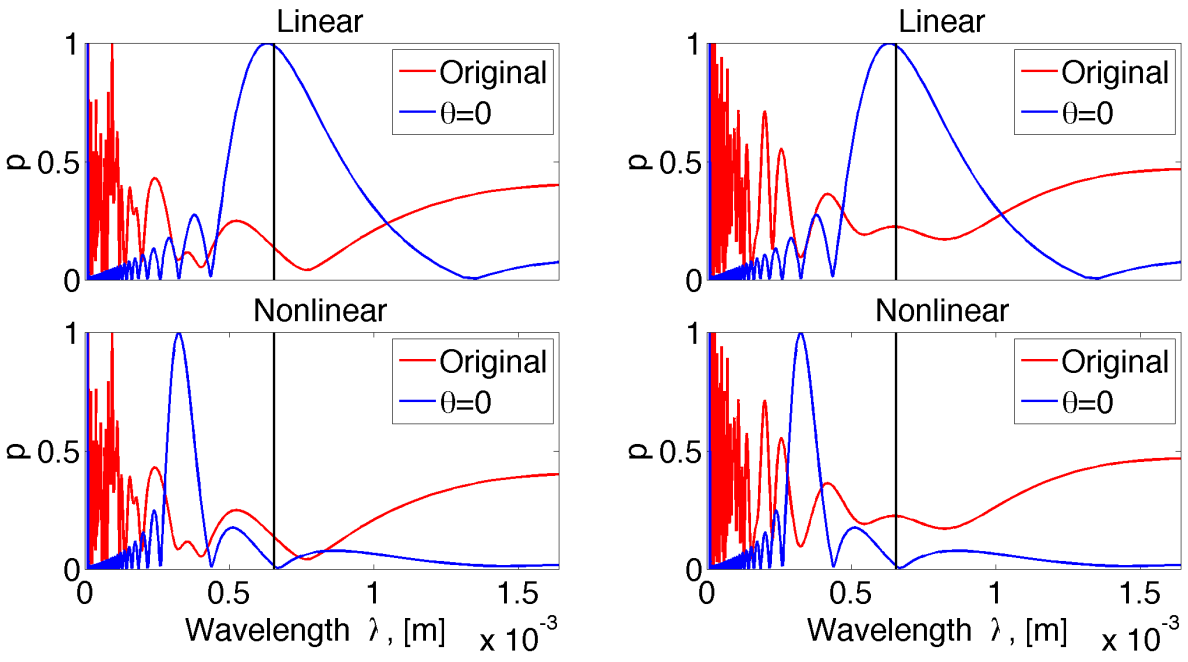

(a) (b)

Figure 7.6: FFT Spectral analysis for random initial profile, $\theta = 0°$. (a) x-direction (b) y-direction.

Figure 7.5. The left column shows the wavelength spectrum in the x-direction while the right column corresponds with the y-direction. The linear evolution plot for each direction is shown on top and the nonlinear on bottom, and the analytically determined stable wavelength according to linear stability analysis is indicated by the vertical black line in each plot. Both the x- and y-directions show similar results in that the linear evolution produces a dominant wavelength, shown by the tallest peak, which is consistent with the analytical result. Alternately, the nonlinear evolution produces a dominant wavelength that appears to be half the length of the analytically determined pattern. This may be attributed to the trend explained by Figure 7.3b, in which the nonlinear term possesses a wavelength twice that of the linearly stable pattern. The result from this simulation indicates that under evolution over long timeframes, the nonlinear term dominates the pattern selection.

7.3 Influence of initial surface architecture

The numerical simulations of this study show that the initial surface architecture of a material under ion bombardment influences its long-term evolution, depending on the angle of ion incidence. Under such conditions, the morphology is said to evolve according to the "templated regime," where the initial surface architecture impacts the final structure. Beginning with a pattern described as a 4 by 4 grid of Gaussian-shaped "bumps", the surface was eroded at various incident angles for both the linear and nonlinear cases. The results showed a point within a range of angles of incidence in which the evolution transitioned from the "self-organized" regime to the "templated" regime. This transition angle occurs between $\theta = 50°$ and $\theta = 55°$, and is an occurrence that has shown to be consistent over various initial architectures.

Figure 7.7 displays the contour plots of the surface profile before and after the transition point. For the full angular spectrum of surface contour plots and the corresponding FFT spectral analysis plots, see Appendix C. It can be seen that prior to the transition at an angle of incidence of $\theta = 50°$, the evolved surface is self-organized and possesses a pattern that is unrelated to the initial Gaussian bump form for both the linear and nonlinear cases. After the transition, at an incident angle of $\theta = 55°$, the pattern in the x-direction shows a templated structure that correlates with the bumps of the initial profile, while in the y-direction the structure is consistent with the result prior to the transition. The difference between the linear and nonlinear results is demonstrated by the topography of the surface features. The nonlinearly evolved profile shows individual peaks, where the linear profile displays peaks that alternate in direction along rows following the y-axis.

The spectral analysis of the contour plots demonstrates the trends clearly by showing how the dominant wavelength changes for the evolved surface across the transition point. Figure 9.7 shows the results at $\theta = 50°$, prior to the transition point, where in both the x and y directions the surface wavelength under nonlinear evolution is half that of the linear result. In Figure 9.8, the result after the transition angle is displayed. It can be seen

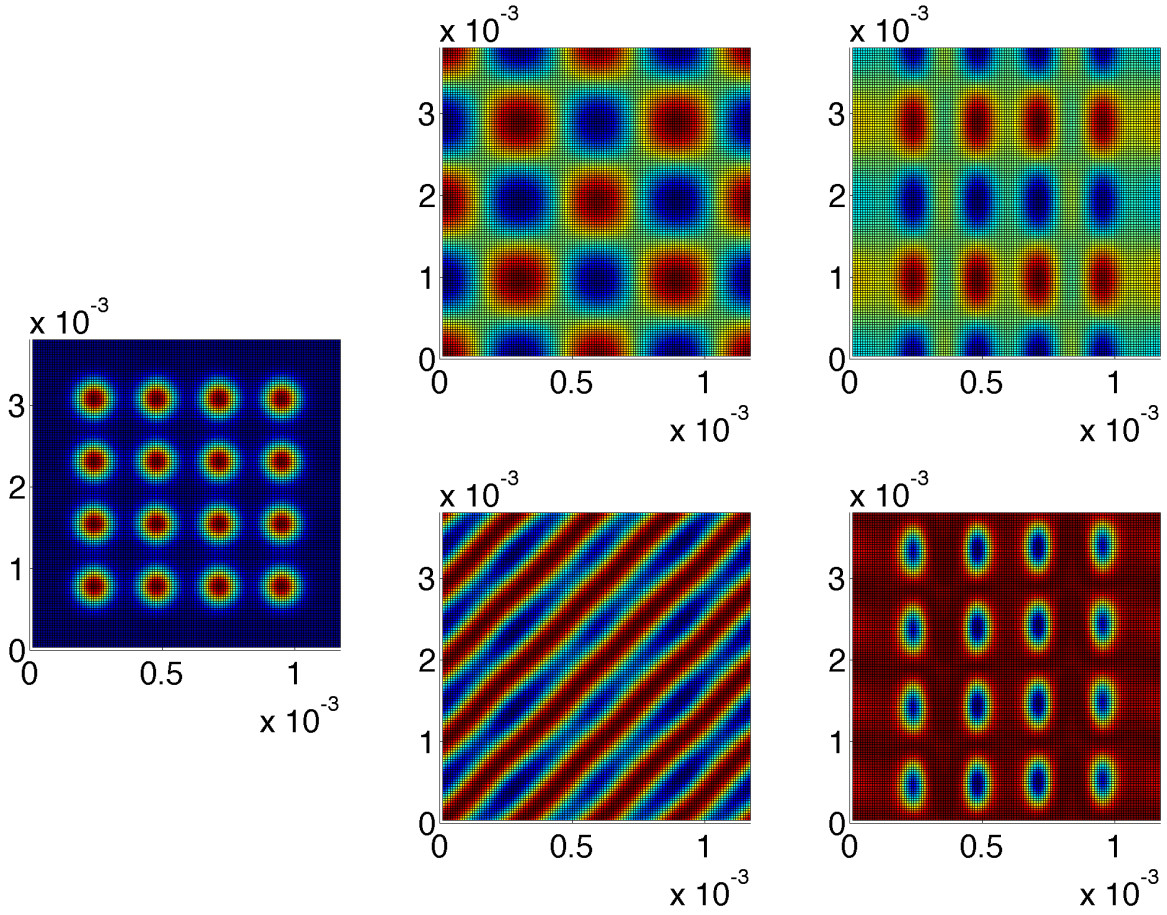

Figure 7.7: Comparison of evolved surfaces for initial profile of 4x4 gaussian bumps (a). Figure shows (b) $\theta = 50°$ and (c) $\theta = 55°$.

that the wavelength results in the y-direction match the findings from the spectral analysis prior to the transition. In the x-direction, however, the outcome is unique. Under linear evolution, the dominant wavelength of the final surface morphology matches that of the initial wavelength. For the nonlinear case, it can be seen that the dominant wavelength does not become apparent when compared to the initial profile. From the contour plots, it can be seen that this result is attributed to the formation of individual troughs that correspond to the Gaussian bumps of the initial architecture.

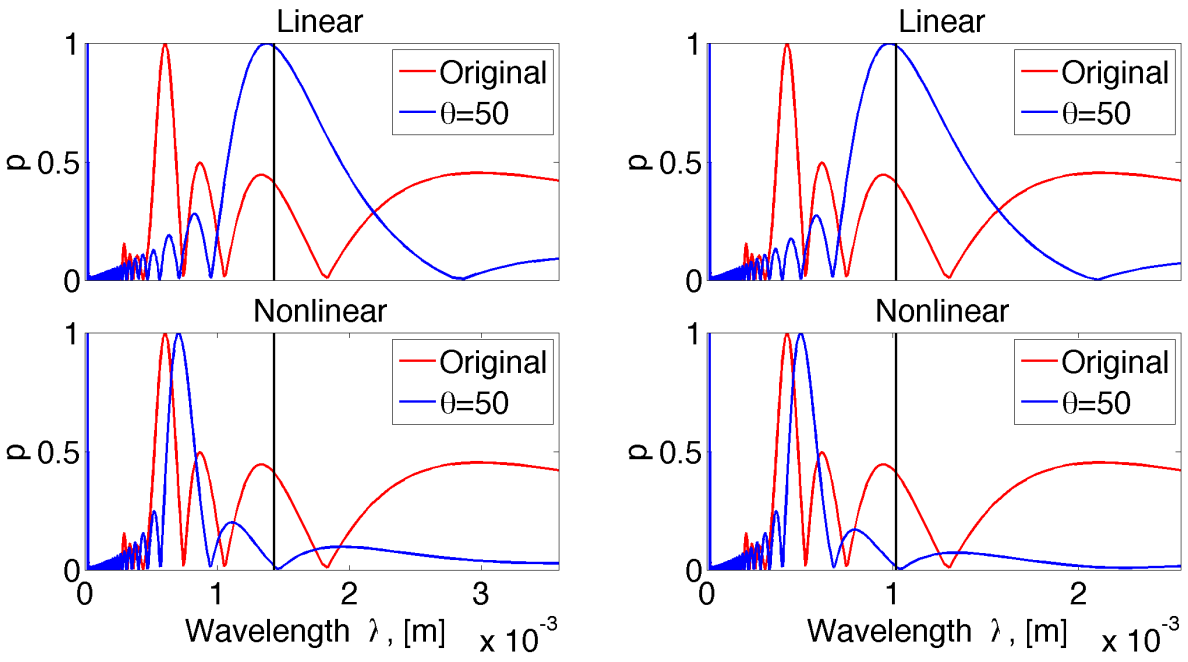

(a) (b)

Figure 7.8: FFT Spectral analysis for initial profile of 4x4 gaussian bumps, $\theta = 50°$. (a) x-direction (b) y-direction.

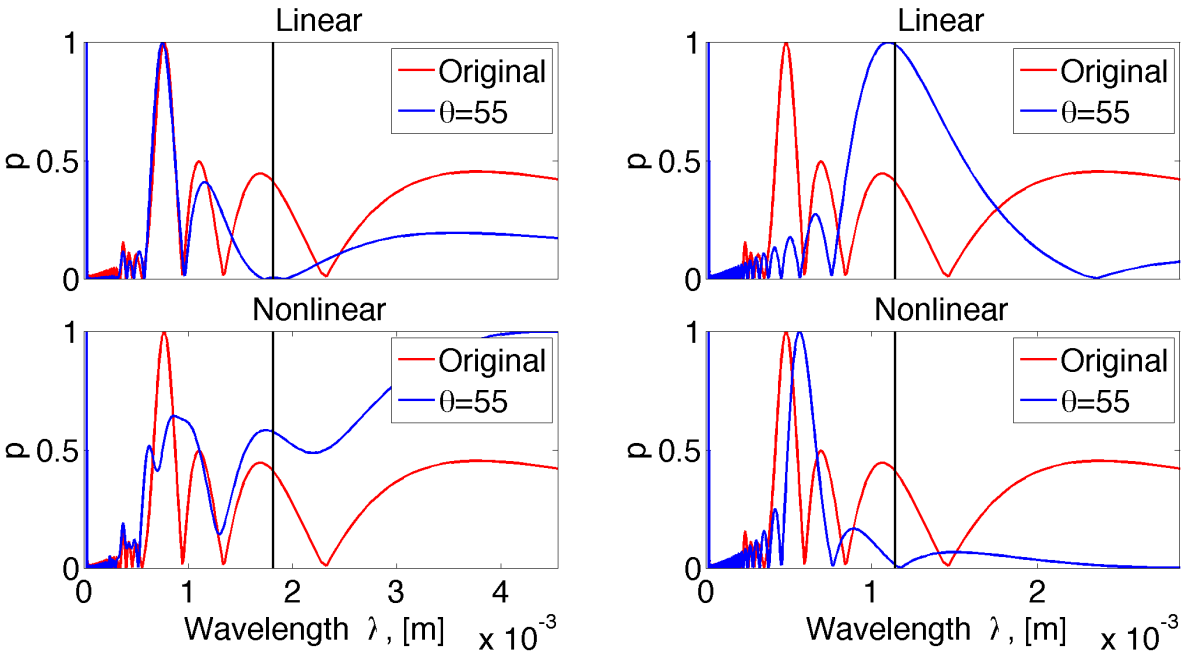

(a) (b)

Figure 7.9: FFT Spectral analysis for initial profile of 4x4 gaussian bumps, $\theta = 55°$.

7.4 Effects of damping

The role of redeposition is considered through the additional relaxation effect offered by introducing a damping term to the evolution equation. The results showed that the effect of damping varies depending on the angle of ion incidence and presence of the nonlinear term in the evolution equation. See Appendix D for the full angular spectrum of damped and undamped evolution for both the linear and nonlinear case, as well as the corresponding spectral analysis plots. Figure 7.10 shows the numerical results for normal ion incidence with and without the damping effect. It can be seen that in the nonlinear case, the morphological differences between damped and undamped are much more significant than for the linear case. It can be understood from this result that at normal incidence, the nonlinear term is in competition with the linear term such that the presence of both produces a unique surface pattern.

The spectral analysis of the surface under normal incidence is shown for the damped and undamped cases in Figures 9.13 and 9.23, respectively. As expected, the undamped case shows that in both directions the dominant wavelength tends close to linear stability under linear evolution, and possesses half that wavelength for nonlinear evolution. For the damped case, however, all evolved surfaces have taken on wavelengths that correspond to linear stability analysis. The difference is most noticeable for the nonlinear case, where the profile does not naturally take on this pattern without the damping term. The conclusion to be drawn from this simulation is that at low angles of incidence, the damping term most significantly affects nonlinear evolution.

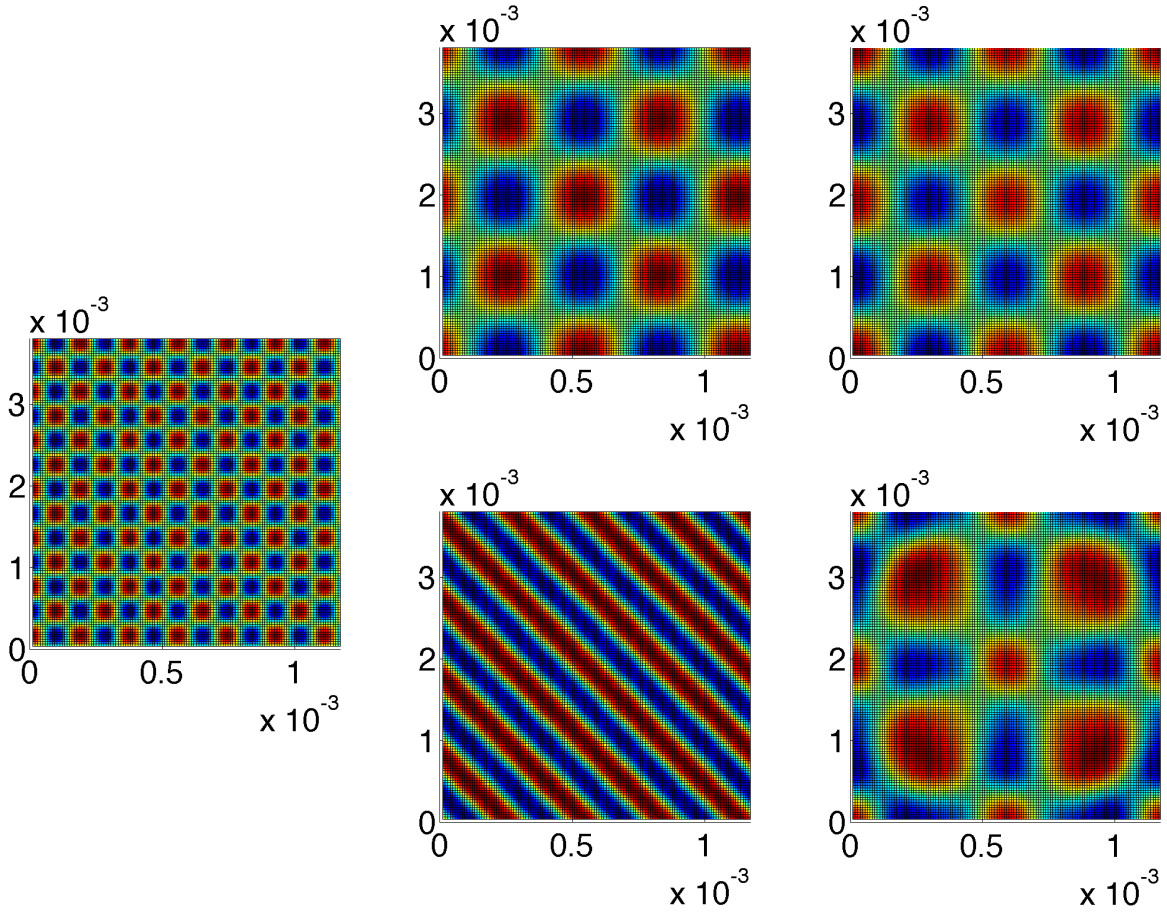

(a) (b) (c)

Figure 7.10: Comparison of evolved surfaces for the (b) undamped and (c) damped case. (a) Original surface: $h = \sin(\omega x)\cos(\omega y)$, $\omega = 3.2$, $\theta = 0°$.

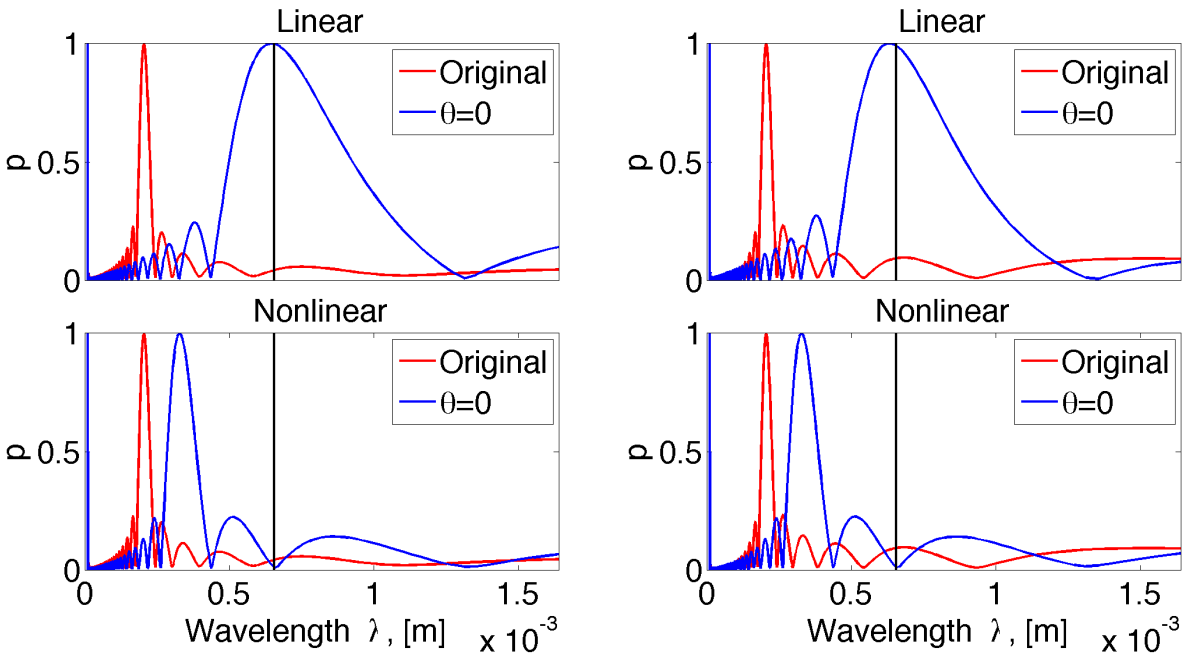

(a) (b)

Figure 7.11: FFT Spectral analysis for initial profile h =sin(ωx)cos(ωy), $\theta = 0°$, undamped evolution. (a) x-direction (b) y-direction.

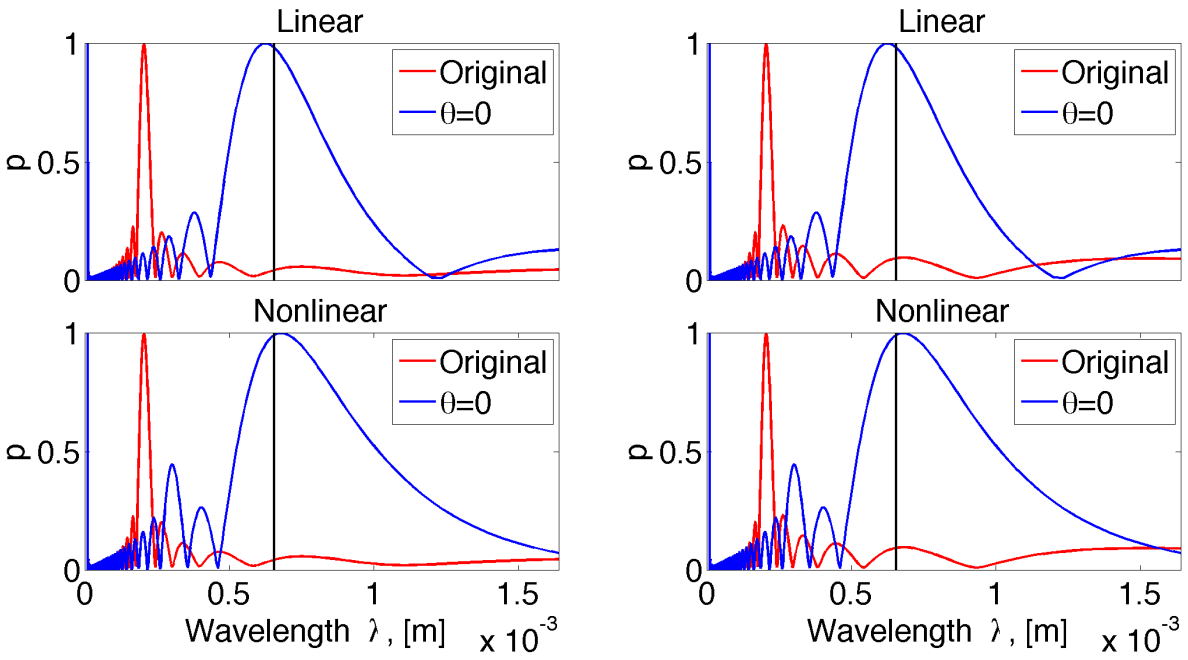

(a) (b)

Figure 7.12: FFT Spectral analysis for initial profile h =sin(ωx)cos(ωy), $\theta = 0°$, damped evolution. (a) x-direction (b) y-direction.

It has been found that at an angle of incidence of $\theta = 45°$, the evolved morphology in both the linear and nonlinear case has no directional tendency, as is the case for both lower and higher angles. By introducing a damping term, Figure 7.13 shows that there appears to be no visible effect of damping on the shaping of surface features.

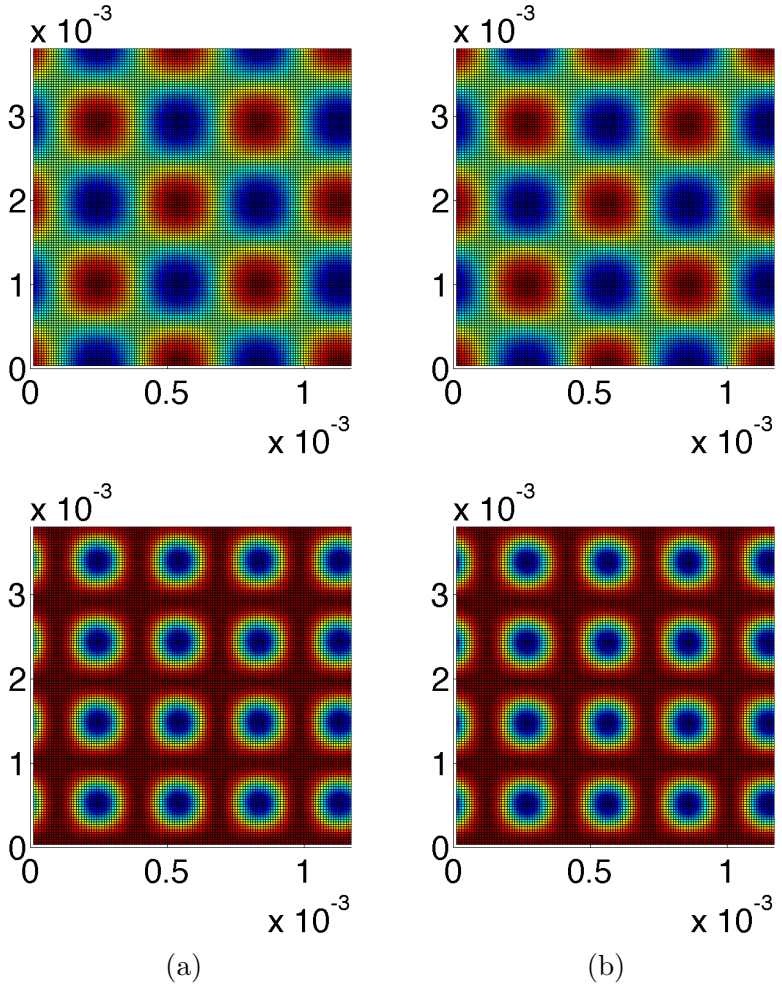

Figure 7.13: Comparison of evolved surfaces for the (a) undamped and (b) damped case. Original surface: $h = \sin(\omega x)\cos(\omega y)$, $\theta = 45°$.

Figures 9.16 and 9.26 show the spectral analysis of the undamped and damped evolution, respectively. The results follow the qualitative observations seen in the contour plots, where the damping has no observable influence on the dominant wavelength of the evolved surface profiles. The conclusion to be drawn from this result is that for transitional angles of incidence, the evolution is driven largely by erosive instabilities that overcome the influence

of damping.

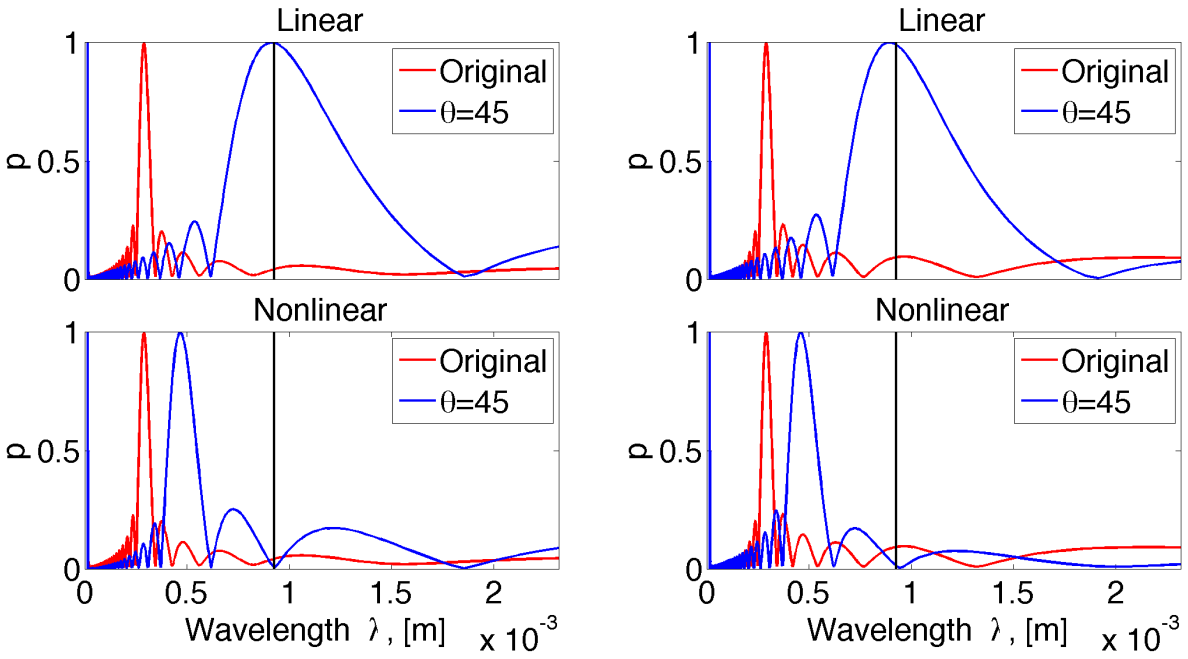

(a) (b)

Figure 7.14: FFT Spectral analysis for initial profile h =sin(ωx)cos(ωy), $\theta = 45°$, undamped evolution. (a) x-direction (b) y-direction.

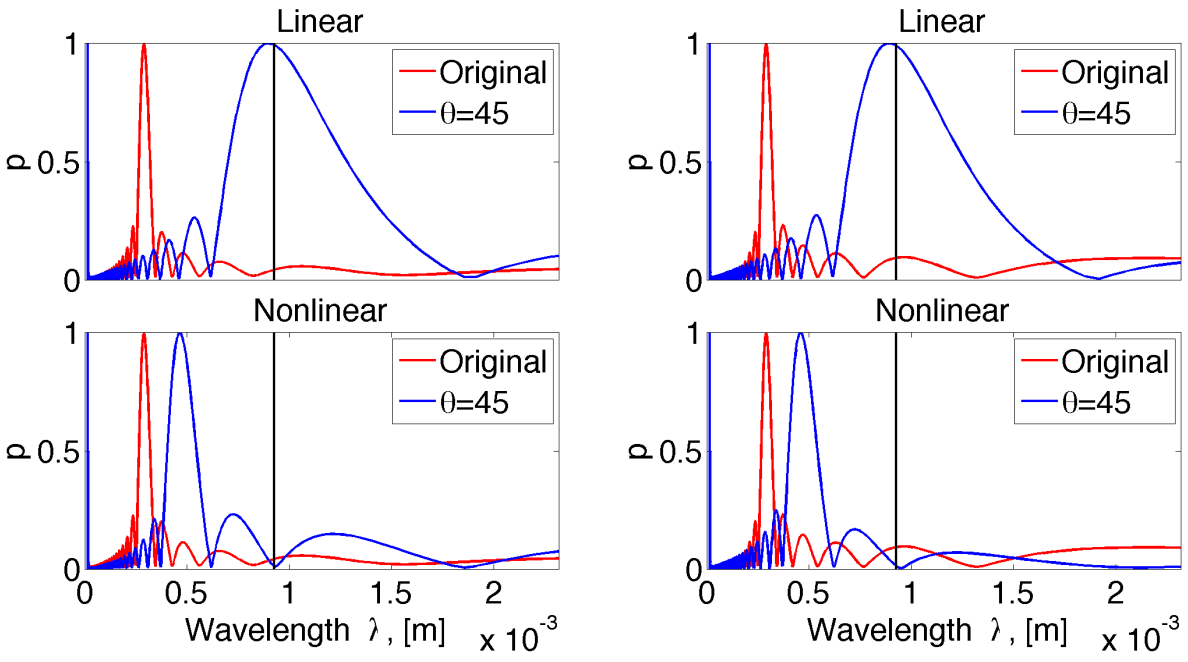

Figure 7.15: FFT Spectral analysis for initial profile h =sin(ωx)cos(ωy), $\theta = 45°$, damped evolution. (a) x-direction (b) y-direction.

At high angles of incidence, it has been observed that the initial architecture plays a significant role in determining the morphology of the evolved surface. Figure 7.16 shows the contour plots of the previously examined surface exposed to ion bombardment at an incident angle of $\theta = 70°$ for both the damped and undamped case. The results show that for both the linear and nonlinear cases, damping strongly affects the evolved profile of the surface. The resulting topography is similar for both the linear and nonlinear cases, indicating that the nonlinear effect is less significant at higher angles of incidence.

The corresponding spectral analysis for the undamped case is shown in Figure 9.20. This shows that in the x-direction, the initial architecture is very influential in determining the evolved profile, whereas the wavelength in the y-direction corresponds closely with linear stability analysis. The spectral analysis for the damped case is seen in Figure 9.30, and demonstrates a significant effect from damping when compared to the undamped results. It can be seen that the final morphology in the x-direction possesses a wavelength that tends

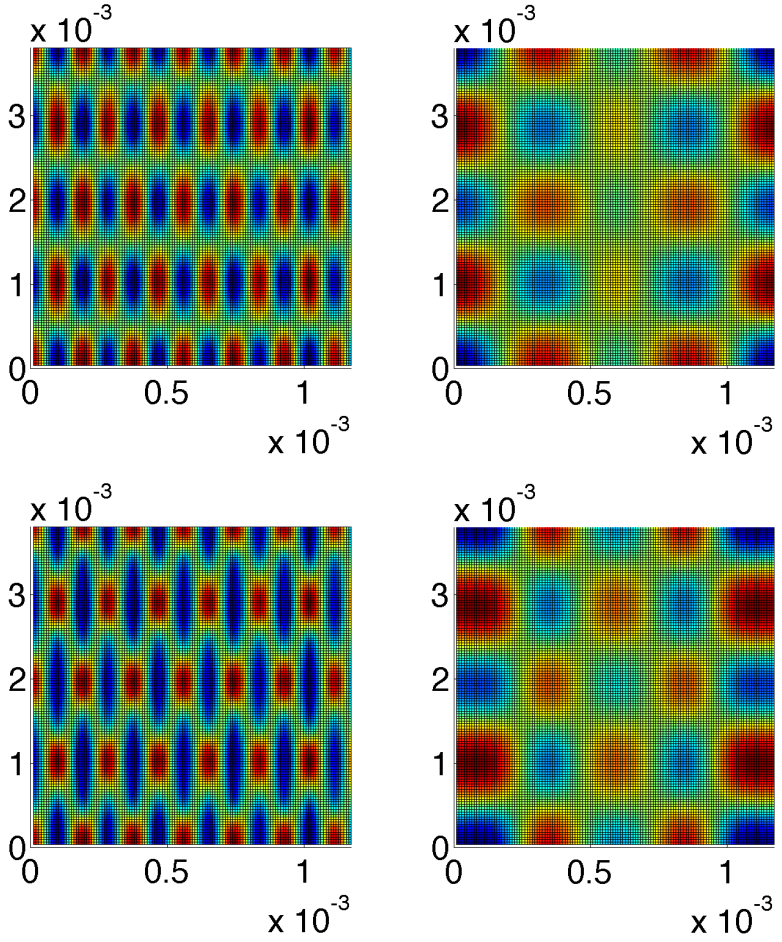

Figure 7.16: Comparison of evolved surfaces for the (a) undamped and (b) damped case. Original surface: $h = \sin(\omega x)\cos(\omega y)$, $\theta = 70°$.

much closer to that of linear stability, although it can be observed that it does not match the analytical result exactly. This disparity may be attributed to the sustained effect of initial architecture on the evolved patterning. The conclusion to be drawn from these results is that at high angles of ion incidence, damping plays a significant role in the development of the evolved profile.

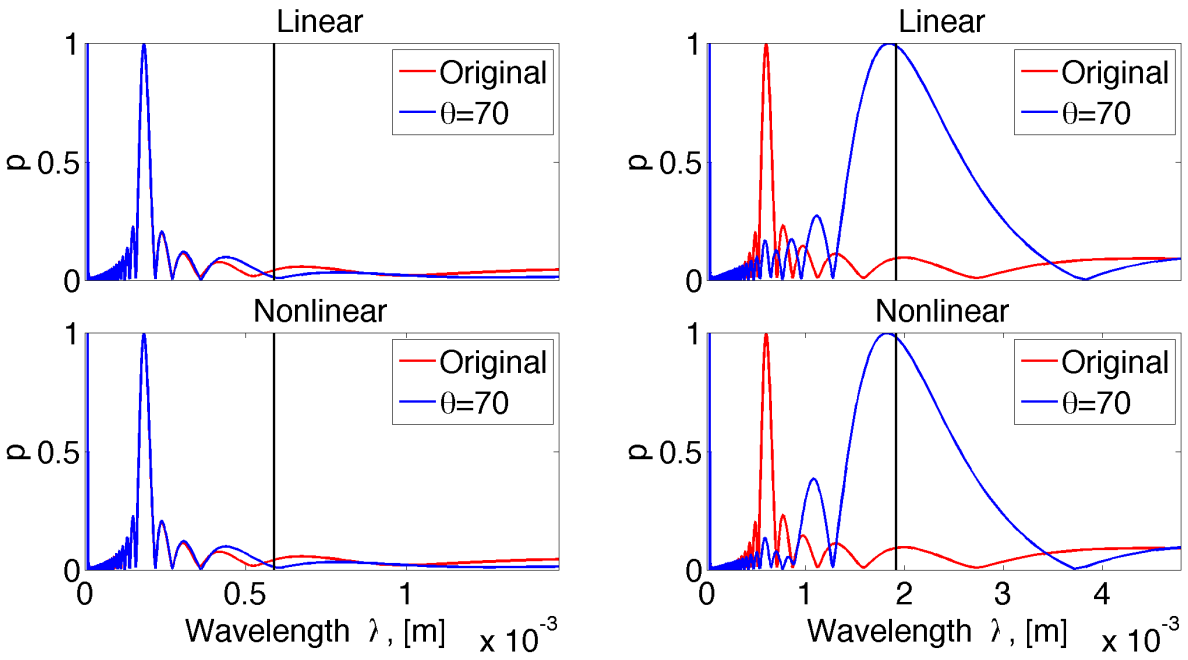

(a) (b)

Figure 7.17: FFT Spectral analysis for initial profile h =sin(ωx)cos(ωy), $\theta = 70°$, undamped evolution. (a) x-direction (b) y-direction.

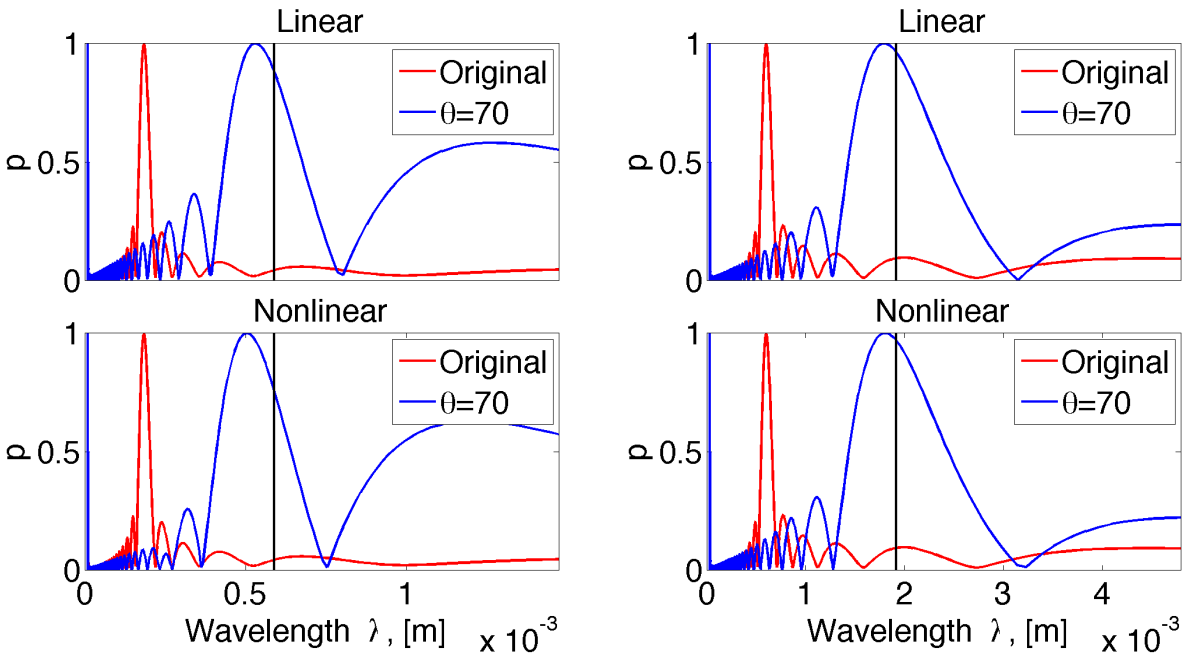

(a) (b)

Figure 7.18: FFT Spectral analysis for initial profile h =sin(ωx)cos(ωy), $\theta = 70°$, damped evolution. (a) x-direction (b) y-direction.

7.5 Modeling Conclusions

The FFT-based numerical method used in this study has allowed for the examination of a number of variable conditions for producing simulations of ion bombarded surfaces. These studies were extended to three main categories related to the evolution equation: the role of nonlinearities, the effect of initial surface architecture, and the presence of a damping term. For each of these categories, the role of the angle of ion incidence was noted. These simulations allow for a number of important conclusions to be drawn.

Simulations performed using the linear erosion equation produced numerical results that demonstrated the formation of surface ripples. Performing spectral analysis on the profiles showed that they closely matched the analytical calculations for stable ripple formation. By introducing the nonlinear term to the evolution equation, it was found that the effect of the nonlinearities is significant over long time spans. Spectral analysis as well as qualitative results show that at short time frames, the nonlinear term has little effect on the morphology of the surface profile. After a sufficient number of time steps, however, the nonlinear term grows rapidly and dominates the evolution equation. The nonlinear influence manifests itself by producing surface ripples with a wavelength that is half that of what is expected according to linear stability.

The evolution of a number of initial surface profiles was considered across incremented angles of incidence. It was found that the angle at which ions approached the material surface determined the influence of the initial architecture on the evolved morphology. Only at high angles of incidence, closer to grazing, is the initial profile preserved in the evolved profile. The transition between the self-organized profile regime and the templated regime has been found to occur between angles of ion incidence of 50° and 55°. Prior to this point, no clear remnant of the initial pattern exists on a fully evolved surface, meaning that the final surface configuration results from the stability of the evolution equation.

At high angles, the damping term produces morphologies that exhibit self-organized patterning. This damping effect outweighs the templating seen previously for high angles,

indicating that the influence of initial architecture appears to be suppressed by the addition of damping. The effect of damping, however, is not consistent across all angles of incidence. At high angles of incidence, damping significantly alters the morphology of both the linear and nonlinear evolution cases. At middle-range angles, there appears to be no influence on the surface evolution for both linear and nonlinear evolution. At low angles of incidence, damping appears to be influential under nonlinear evolution only, as a self-organized pattern attributed to the damping term overcomes the presence of the nonlinear term. Table 7.1 summarizes the results at each level of angle of incidence, where the check marks indicate an influence of damping and the "×'s" indicate no morphological difference due to damping.

Table 7.1: Angular effect of damping.

	Linear	Nonlinear
Low θ	×	✓
Mid θ	×	×
High θ	✓	✓

This investigation studied the component contributions of the chosen evolution equation, and considered the effect of various parameters on the evolved surface morphology. There was found to be an interconnected dependence of nonlinearities, initial architecture, and damping on the surface evolution. Additionally, the angle of ion incidence was found to interplay with each of these components of the governing equation by affecting their respective influence on the evolution.

CHAPTER 8

Conclusions

8.1 Experimental Achievements and Future Work

The experimental study has produced a number of notable achievements. Examining the behavior of nano- and micro-architectured surfaces under plasma bombardment has produced a deeper level of knowledge about the effects of roughness and unique geometries on plasma-facing materials. Ballistic deposition was observed on dendritic surfaces at low fluences, which indicates a self-healing mechanism that facilitates mass retention through geometric re-trapping of sputtered material. Subsequent QCM measurements demonstrated the effect of the self-healing mechanism on a material's sputtering yield, as material retention properties counteracted the erosive effect of plasma exposure. The sputtering yield of textured molybdenum samples exposed to 300 eV Ar plasma was found to be roughly 1/2 of the corresponding value of flat samples.

QCM data for tests on the textured Mo samples C and D over extended fluence ranges demonstrated the transient nature of the sputtering yield across increasing levels of fluence. Low fluence correlations of the detected sputtering yield with the measured surface roughness indicated an inverse linear relationship, meaning that the surface architecture dictates the level of yield reduction. Therefore, changes in the sputtering yield may be attributed to the evolving surface morphology. The principal conclusion from these results is that the sputtering yield is not a fundamental material property, but can be engineered through surface texturing.

A quantified dependence of the sputtering yield on plasma fluence has been achieved

for Mo samples C and D, which demonstrates the transient effect and dynamic nature of the sputtering yield. Figure 8.1a shows the curve produced from the QCM measurements. Calculating the area under the curve produces the total number of atoms per unit area lost due to exposure. With the curve converging to a yield near 0.42, the corresponding value for a planar sample can be determined, where no yield reduction is present. Comparing the reduced value with the number for a planar surface indicates $\sim 16.5\%$ reduction in material loss due to texturing, over the entire transient fluence range. Various techniques may be employed to harness the yield reduction of micro-architectured materials such as layering and scaffolding (Figure 8.2), which allows for renewed yield reduction as the texturing is worn down and new layers are exposed, which would result in yield behavior similar to that shown in Figure 8.1b.

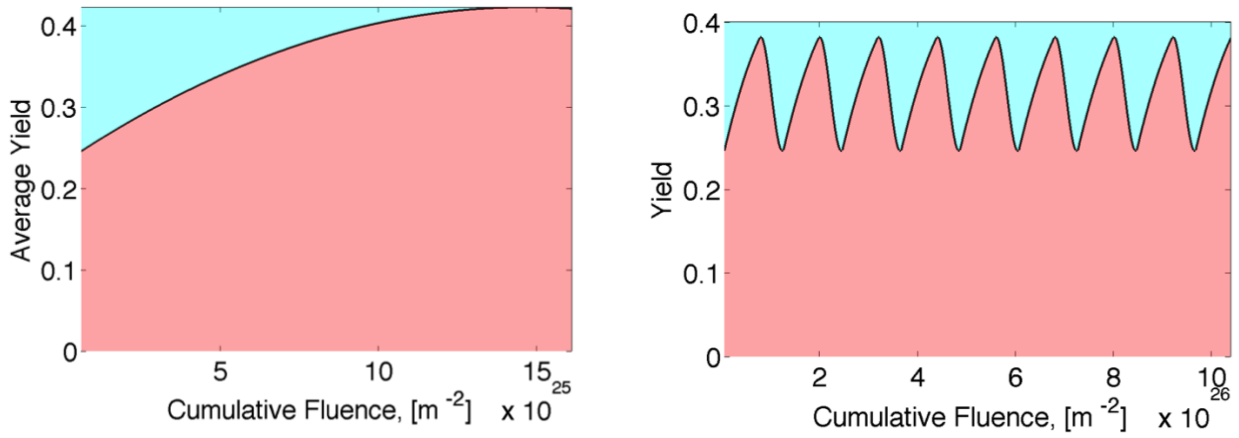

Figure 8.1: (a) Transient yield region for Sample C (b) Architecture-renewed transient yield.

A new class of materials that provides significant potential for further development is refractory metal foams (Figure 8.3a). This material architecture offers potential for improved longevity on multiple scales. The ligaments themselves offer a means for ballistic deposition effects through geometric retrapment of sputtered material. In addition, Figure 8.3b shows the texturing of the ligament surfaces through the growth of grass-like dendrites, which can offer an additional scale of healing. These foams may be used as shown in Figure 8.2b to provide a scaffold for multiscale architectures, providing a further avenue for sustained yield

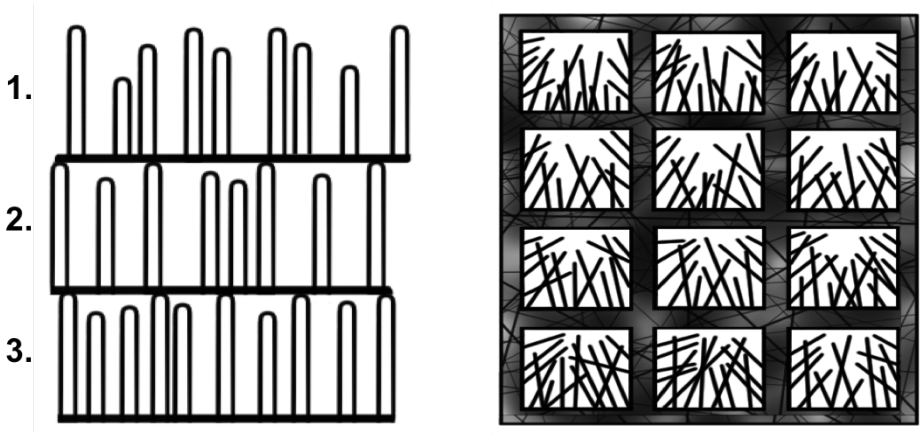

(a) (b)

Figure 8.2: Proposed structures (a) Layering of architectured surfaces (b) Scaffolding with foam structure.

reduction. Future testing of these material structures can provide further insight into the ways metallic foams may be used to increase the lifetime of EP device components.

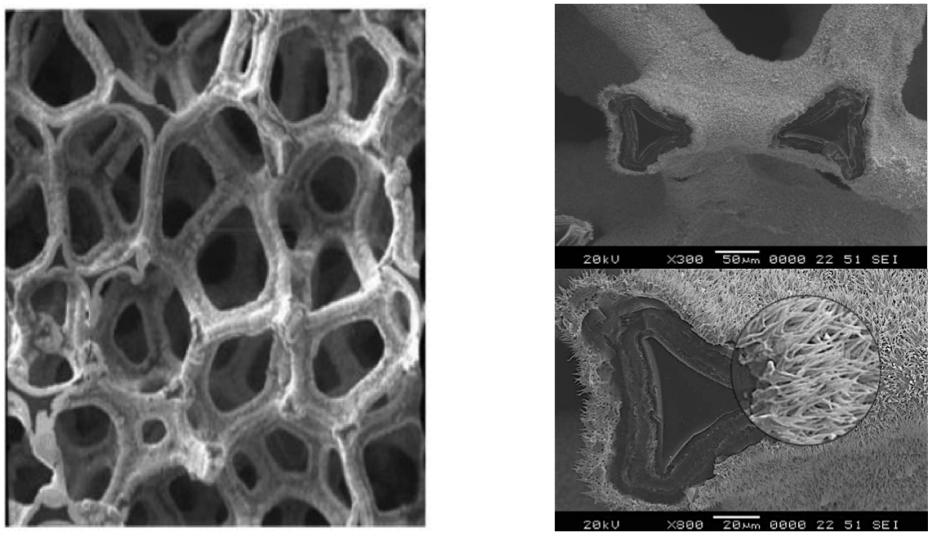

(a) (b)

Figure 8.3: (a) SEM image of tungsten foam. (b) Nano-texturing of foam ligaments.

8.2 Modeling Achievements

The modeling effort was designed to explore the physical effects of surface evolution by simulating the development of surface nano-patterns that emerge through plasma exposure. A theoretical framework based on the formulation first presented by Bradley and Harper[6] was expanded to include nonlinearities and linear damping. The outcome can therefore be expected to be more physically relevant and applicable to the study of plasma-facing materials.

The effect of nonlinearities in the evolution equation is discussed in Section 7.2, where it is noted that at long time scales, the nonlinear term dominates the evolution. Early in the evolution, nonlinearities are shown to have only a peripheral effect on the final morphology. This result is demonstrated by the spectral analysis in Figure 7.5, which also shows that at longer time scales, the nonlinear term takes over the evolution and forces the dominant wavelength to be half the expected wavelength found using linear stability analysis. The influence of initial architecture is considered in Section 7.3, where it is noted that the "templated regime" exists only for higher angles of ion incidence. Prior to this transition point, the evolved morphology is organized according to what is determined by the evolution equation, however in the templated regime, the initial pattern is evident in the final configuration. Deposition is modeled as damping in Section 7.4, where it was shown that the effect of damping is prevalent only for certain angular conditions, which is also related to the presence of nonlinearities in the evolution equation.

The simulations performed in this study extend the scope of exploration accomplished by the experimental study of surface evolution, and offer an avenue for further theoretical development. The size scale of surface patterns observed in the simulations ranged from the nanometer to the millimeter scale, indicating the multi-scale application of the simulations.

CHAPTER 9

Appendices

9.1 Appendix A

$E(\boldsymbol{r'})$ is the deposited energy distribution, as defined by Sigmund. Knowing the surface element $d\boldsymbol{r} \simeq dXdY$ in the local coordinate system, the distances X', Y', Z' from the exponential distribution (5.9) can also be defined in the local coordinate frame as follows:

$$\begin{aligned} X' &= X\cos\varphi + Z\sin\varphi \\ Y' &= Y \\ Z' &= a + X\sin\varphi - Z\cos\varphi \end{aligned} \tag{9.1}$$

Therefore, from (5.14) the following expression is found:

$$\begin{aligned} v_n =& \frac{J\epsilon p}{(2\pi)^{3/2}\alpha\beta^2} \int\int (\cos\varphi + (\partial_x Z)\sin\varphi) \\ & \times \exp\left\{ -\frac{(a + X\sin\varphi - Z\cos\varphi)^2}{2\alpha^2} - \frac{(X\cos\varphi + Z\sin\varphi)^2 + Y^2}{2\beta^2} \right\} dXdY \end{aligned} \tag{9.2}$$

The dimensionless variables $\zeta_x = X/a$, $\zeta_y = Y/a$, and $\zeta_z = Z/a$ are introduced, and the integration limits are extended to infinity. From (9.3), the expression is expanded to:

$$\begin{aligned} v_n =& \frac{J\epsilon p}{(2\pi)^{3/2}\alpha\beta^2}\int\int (\cos\varphi + (\partial_x Z)\sin\varphi) \\ & \times \exp\left\{ -\frac{\left(a^2 + 2Xa\sin\varphi - 2Za\cos\varphi - 2XZ\sin\varphi\cos\varphi + X^2\sin^2\varphi + Z^2\cos^2\varphi\right)^2}{2\alpha^2} \right. \\ & \left. -\frac{\left(X^2\cos^2\varphi + 2XZ\sin\varphi\cos\varphi + X^2\sin^2\varphi + Z^2\cos^2\varphi\right)^2 + Y^2}{2\beta^2} \right\} dXdY \end{aligned} \tag{9.3}$$

The dimensionless variables $\zeta_x = X/a$, $\zeta_y = Y/a$, and $\zeta_z = Z/a$ are introduced, and the integration limits are extended to infinity. The following expression results:

$$\begin{aligned} v_n =& \frac{J\epsilon p}{(2\pi)^{3/2}\alpha\beta^2}\exp\left(-\frac{a_\alpha^2}{2}\right)\int_{-\infty}^{\infty}\int_{-\infty}^{\infty}\left(\cos\varphi + \frac{\partial\zeta_z}{\partial\zeta_x}\sin\varphi\right)\exp\left(-\frac{\zeta_x a^2\sin\varphi}{\alpha^2}\right) \\ & \times \exp\left(\frac{\zeta_z a^2\cos\varphi}{\alpha^2}\right)\exp\left(\frac{\zeta_x\zeta_z a^2\sin\varphi\cos\varphi}{\alpha^2}\right)\exp\left(-\frac{\zeta_x^2 a^2\sin^2\varphi}{2\alpha^2}\right) \\ & \times \exp\left(-\frac{\zeta_z^2 a^2\cos^2\varphi}{2\alpha^2}\right)\exp\left(-\frac{\zeta_x^2 a^2\cos^2\varphi}{2\beta^2}\right)\exp\left(-\frac{\zeta_x\zeta_z a^2\sin\varphi\cos\varphi}{\beta^2}\right) \\ & \times \exp\left(-\frac{\zeta_z^2 a^2\sin^2\varphi}{2\beta^2}\right)\exp\left(-\frac{\zeta_y^2 a^2}{2\beta^2}\right)d\zeta_x d\zeta_y a^2 \end{aligned} \tag{9.4}$$

Regrouping the terms:

$$\begin{aligned} v_n =& \frac{J\epsilon p a^2}{(2\pi)^{3/2}\alpha\beta^2}\exp\left(-\frac{a_\alpha^2}{2}\right)\int_{-\infty}^{\infty}\int_{-\infty}^{\infty}d\zeta_x d\zeta_y\left(\cos\varphi + \frac{\partial\zeta_z}{\partial\zeta_x}\sin\varphi\right) \\ & \times \exp\left(-\zeta_y^2\left[\frac{a^2}{2\beta^2}\right]\right)\exp\left(-\zeta_x\left[a_\alpha^2\sin\varphi\right]\right)\exp\left(\zeta_z\left[a_\alpha^2\cos\varphi\right]\right) \\ & \times \exp\left(-\frac{\zeta_x^2}{2}\left[a_\alpha^2\sin^2\varphi + a_\beta^2\cos^2\varphi\right]\right)\exp\left(-\frac{\zeta_z^2}{2}\left[a_\alpha^2\cos^2\varphi + a_\beta^2\sin^2\varphi\right]\right) \\ & \times \exp\left(-2\zeta_x\zeta_z\left[a_\alpha^2 - a_\beta^2\right]\sin\varphi\cos\varphi\right) \end{aligned} \tag{9.5}$$

Further simplification leads to

$$\begin{aligned} v_n =& \frac{J\epsilon p a^2}{(2\pi)^{3/2}\alpha\beta^2}\exp\left(-\frac{a_\alpha^2}{2}\right)\int_{-\infty}^{\infty}\int_{-\infty}^{\infty} d\zeta_x d\zeta_y \left(\cos\varphi + \frac{\partial\zeta_z}{\partial\zeta_x}\sin\varphi\right) \\ & \times \exp\left(-\zeta_y^2 L^2\right)\exp\left(-\zeta_x A\right)\exp\left(\zeta_z B_2\right) \\ & \times \exp\left(-\frac{\zeta_x^2}{2}B_1\right)\exp\left(-4D\zeta_z^2\right)\exp\left(-2C\zeta_x\zeta_z\right) \end{aligned} \tag{9.6}$$

Where

$$A = a_\alpha^2 \sin\varphi \tag{9.7}$$

$$B_1 = a_\alpha^2 \sin^2\varphi + a_\beta^2 \cos^2\varphi \tag{9.8}$$

$$B_2 = a_\alpha^2 \cos\varphi \tag{9.9}$$

$$C = \frac{1}{2}\left(a_\beta^2 - a_\alpha^2\right)\sin\varphi\cos\varphi \tag{9.10}$$

$$D = \frac{1}{8}\left(a_\beta^2 \sin^2\varphi + a_\alpha^2 \cos^2\varphi\right) \tag{9.11}$$

$$L = \frac{a_\beta}{\sqrt{2}} \tag{9.12}$$

The surface profile can be approximated at an arbitrary point as follows, to second order:

$$Z(X,Y) \simeq \frac{\Delta_{20}X^2}{a} + \frac{\Delta_{02}Y^2}{a} \tag{9.13}$$

Where the following notation is introduced:

$$\Delta_{nm} = \frac{a^{n+m-1}}{n!m!}\frac{\partial^{n+m}Z(X,Y)}{\partial^n X \partial^m Y} \tag{9.14}$$

Therefore, we can say

$$\zeta_z \approx \Delta_{20}\zeta_x^2 + \Delta_{02}\zeta_y^2 \tag{9.15}$$

Substituting (9.15) into the velocity equation results in

$$\begin{aligned} v_n =& \frac{J\epsilon p a^2}{(2\pi)^{3/2}\alpha\beta^2}\exp\left(-\frac{a_\alpha^2}{2}\right)\int_{-\infty}^{\infty}\int_{-\infty}^{\infty} d\zeta_x d\zeta_y \\ & \times \exp\left(-\zeta_y^2 L^2\right)\exp\left(-\zeta_x A - \frac{1}{2}\zeta_x^2 B_1\right) \\ & \times \left(\cos\varphi + \frac{\partial}{\partial\zeta_x}\left[\Delta_{20}\zeta_x^2 + \Delta_{02}\zeta_y^2\right]\sin\varphi\right) \\ & \times \exp\left(-2C\left[\Delta_{20}\zeta_x^3 + \Delta_{02}\zeta_x\zeta_y^2\right]\right)\exp\left(B_2\left[\Delta_{20}\zeta_x^2 + \Delta_{02}\zeta_y^2\right]\right) \end{aligned} \tag{9.16}$$

Using the approximation $e^t \approx 1 + t$

$$\begin{aligned} v_n =& \frac{J\epsilon p a^2}{(2\pi)^{3/2}\alpha\beta^2}\exp\left(-\frac{a_\alpha^2}{2}\right)\int_{-\infty}^{\infty}\int_{-\infty}^{\infty} d\zeta_x d\zeta_y \\ & \times \exp\left(-\zeta_y^2 L^2\right)\exp\left(-\zeta_x A - \frac{1}{2}\zeta_x^2 B_1\right)\left(\cos\varphi + 2\Delta_{20}\varphi_x \sin\varphi\right) \\ & \times \left(1 + B_2\Delta_{20}\zeta_x^2 + B_2\Delta_{02}\zeta_y^2 - 2C\Delta_{20}\zeta_x^3 - 2C\Delta_{02}\zeta_x\zeta_y^2\right) \end{aligned} \tag{9.17}$$

Grouping the terms:

$$\begin{aligned} v_n =& \frac{J\epsilon p a^2}{(2\pi)^{3/2}\alpha\beta^2}\exp\left(-\frac{a_\alpha^2}{2}\right)\int_{-\infty}^{\infty}\int_{-\infty}^{\infty} d\zeta_x d\zeta_y \\ & \times \exp\left(-\zeta_y^2 L^2\right)\exp\left(-\zeta_x A - \frac{1}{2}\zeta_x^2 B_1\right) \\ & \times \left[\cos\varphi + \left\{\left(B_2\zeta_x^2 - 2C\zeta_x^3\right)\cos\varphi + 2\zeta_x\sin\varphi\right\}\Delta_{20}\right. \\ & \left. + \left\{\left(B_2\zeta_y^2 - 2C\zeta_x\zeta_y^2\right)\cos\varphi\right\}\Delta_{02}\right] \end{aligned} \tag{9.18}$$

This is integrated first for ζ_y:

$$\begin{aligned} v_n =& \frac{J\epsilon p a^2}{(2\pi)^{3/2}\alpha\beta^2}\exp\left(-\frac{a_\alpha^2}{2}\right)\int_{-\infty}^{\infty}\exp\left(-\zeta_x A - \frac{1}{2}\zeta_x^2 B_1\right) \\ & \left[\frac{B_2\sqrt{\pi}\,\mathrm{erf}\left(L\zeta_y\right) - 2C\zeta_x\sqrt{\pi}\,\mathrm{erf}\left(L\zeta_y\right)}{4L^3}\cos\varphi\Delta_{02}\right. \\ & \left. + \frac{\sqrt{\pi}\,\mathrm{erf}\left(L\zeta_y\right)}{2L}\left[\cos\varphi + B_2\zeta_x^2\cos\varphi\Delta_{20} - 2C\zeta_x^3\cos\varphi\Delta_{20} + 2\zeta_x\sin\varphi\Delta_{20}\right]\right]_{-\infty}^{\infty} d\zeta_x \end{aligned} \tag{9.19}$$

which evaluates to give

$$\begin{aligned} v_n =& \frac{J\epsilon p a^2}{(2\pi)^{3/2}\alpha\beta^2}\exp\left(-\frac{a_\alpha^2}{2}\right)\int_{-\infty}^{\infty}\exp\left(-\zeta_x A-\frac{1}{2}\zeta_x^2 B_1\right) \\ & \left\{\frac{(B_2-2C\zeta_x)\sqrt{\pi}}{2L^3}\cos\varphi\Delta_{02}+\frac{\sqrt{\pi}}{L}\Big[\cos\varphi+B_2\zeta_x^2\cos\varphi\Delta_{20}\right. \\ & \left.-2C\zeta_x^3\cos\varphi\Delta_{20}+2\zeta_x\sin\varphi\Delta_{20}\Big]\right\}d\zeta_x \end{aligned} \tag{9.20}$$

Grouping the terms

$$\begin{aligned} v_n =& \frac{J\epsilon p a^2}{(2\pi)^{3/2}\alpha\beta^2}\exp\left(-\frac{a_\alpha^2}{2}\right)\int_{-\infty}^{\infty}\exp\left(-\zeta_x A-\frac{1}{2}\zeta_x^2 B_1\right) \\ & \left\{\left(\frac{B_2}{2L^3}\Delta_{02}+\frac{1}{L}\right)\sqrt{\pi}\cos\varphi+\left(\frac{2\sqrt{\pi}}{L}\sin\varphi\Delta_{20}-\frac{C\sqrt{\pi}\cos\varphi\Delta_{02}}{L^3}\right)\zeta_x\right. \\ & \left.+\left(\frac{B_2\sqrt{\pi}\cos\varphi\Delta_{20}}{L}\right)\zeta_x^2-\left(\frac{2C\sqrt{\pi}\cos\varphi\Delta_{20}}{L}\right)\zeta_x^3\right\}d\zeta_x \end{aligned} \tag{9.21}$$

Which can be written as

$$v_n =\frac{J\epsilon p a^2}{(2\pi)^{3/2}\alpha\beta^2}\exp\left(-\frac{a_\alpha^2}{2}\right)\int_{-\infty}^{\infty}\exp\left(-\zeta_x A-\frac{1}{2}\zeta_x^2 B_1\right)\left\{G+H\zeta_x+I\zeta_x^2-J\zeta_x^3\right\}d\zeta_x \tag{9.22}$$

Where

$$G=\left(\frac{B_2}{2L^3}\Delta_{02}+\frac{1}{L}\right)\sqrt{\pi}\cos\varphi=\left(\frac{B_2\sqrt{2\pi}}{a_\beta^3}\cos\varphi\Delta_{02}\right)+\left(\frac{\sqrt{2\pi}}{a_\beta}\right) \tag{9.23}$$

$$H=\left(\frac{2\sqrt{\pi}}{L}\sin\varphi\Delta_{20}-\frac{C\sqrt{\pi}}{L^3}\cos\varphi\Delta_{02}\right)=\left(\frac{2\sqrt{2\pi}}{a_\beta}\sin\varphi\Delta_{20}-\frac{2C\sqrt{2\pi}}{a_\beta^3}\cos\varphi\Delta_{02}\right) \tag{9.24}$$

$$I=\left(\frac{B_2\sqrt{\pi}\cos\varphi\Delta_{20}}{L}\right)=\left(\frac{B_2\sqrt{2\pi}\cos\varphi\Delta_{20}}{a_\beta}\right) \tag{9.25}$$

$$J=\left(\frac{2C\sqrt{\pi}\cos\varphi\Delta_{20}}{L}\right)=\left(\frac{2C\sqrt{2\pi}\cos\varphi\Delta_{20}}{a_\beta}\right) \tag{9.26}$$

Solving the remaining integral in the erosion velocity equation gives

$$\begin{aligned} v_n =& \frac{J\epsilon p a^2}{(2\pi)^{3/2}\alpha\beta^2}\exp\left(-\frac{a_\alpha^2}{2}\right)\left\{G\cdot\exp\left\{\frac{A^2}{2B_1}\right\}\frac{\sqrt{2\pi}}{\sqrt{B_1}}\right. \\ &- H\cdot\frac{1}{\sqrt{B_1}}\frac{A}{B_1}\exp\left\{\frac{A^2}{2B_1}\right\}\sqrt{\frac{\pi}{2}}\mathrm{erf}\left[\frac{A+B_1\zeta_x}{\sqrt{2B_1}}\right]_{-\infty}^{\infty} \\ &+ I\cdot\frac{(A+B_1)}{B_1^2}\frac{1}{\sqrt{B_1}}\exp\left\{\frac{A^2}{2B_1}\right\}\sqrt{\frac{\pi}{2}}\mathrm{erf}\left[\frac{A+B_1\zeta_x}{\sqrt{2B_1}}\right]_{-\infty}^{\infty} \\ &\left.+ J\cdot\frac{A\left(A^2+3B_1\right)}{B_1^3}\frac{1}{\sqrt{B_1}}\exp\left\{\frac{A^2}{2B_1}\right\}\sqrt{\frac{\pi}{2}}\mathrm{erf}\left[\frac{A+B_1\zeta_x}{\sqrt{2B_1}}\right]_{-\infty}^{\infty}\right\} \end{aligned} \tag{9.27}$$

This evaluates to give

$$\begin{aligned} v_n =& \frac{J\epsilon p a^2}{(2\pi)^{3/2}\alpha\beta^2}\exp\left(-\frac{a_\alpha^2}{2}\right)\frac{\sqrt{2\pi}}{\sqrt{B_1}}\exp\left\{\frac{A^2}{2B_1}\right\} \\ &\times\left[G - H\frac{A}{B_1} + I\frac{(A^2+B_1)}{B_1^2} + J\frac{A\left(A^2+3B_1\right)}{B_1^3}\right] \end{aligned} \tag{9.28}$$

Plugging in the values of the constants,

$$\begin{aligned} v_n =& \frac{J\epsilon p a^2}{(2\pi)^{3/2}\alpha\beta^2}\exp\left(-\frac{a_\alpha^2}{2}\right)\frac{2\pi}{\sqrt{B_1}}\exp\left\{\frac{A^2}{2B_1}\right\} \\ &\times\left[\frac{B_2}{a_\beta^3}\cos\varphi\Delta_{02} + \frac{1}{a_\beta}\cos\varphi + \frac{2AC}{B_1 a_\beta^3}\cos\varphi\Delta_{02}\right. \\ &- \frac{2A}{a_\beta B_1}\sin\varphi\Delta_{20} + \frac{B_2}{B_1^2}\frac{(A^2+B_1)}{a_\beta}\cos\varphi\Delta_{20} \\ &\left.+ \frac{2AC}{a_\beta}\frac{(A^2+3B_1)}{B_1^3}\cos\varphi\Delta_{20}\right] \end{aligned} \tag{9.29}$$

Collecting the terms

$$\begin{aligned} v_n =& 2\pi\frac{\beta}{a}\frac{J\epsilon p a^2}{(2\pi)^{3/2}\alpha\beta^2}\exp\left(-\frac{a_\alpha^2}{2}+\frac{A^2}{2B_1}\right)\frac{1}{\sqrt{B_1}} \\ &\times\left[\cos\varphi + \left\{-\frac{2A}{B_1}\sin\varphi + \frac{B_2}{B_1}\left[1+\frac{A^2}{B_1}\right]\cos\varphi + \frac{2AC}{B_1^2}\left[3+\frac{A^2}{B_1}\right]\cos\varphi\right\}\Delta_{20}\right. \\ &\left.+\left\{\frac{2}{a_\beta^2}\cos\varphi\left(\frac{B_2}{2}+\frac{AC}{B_1}\right)\right\}\Delta_{02}\right] \end{aligned} \tag{9.30}$$

This expression leads to the result shown by (5.21).

9.2 Appendix B

The BH velocity equation is written up to second order as follows:

$$v_n = \frac{J\epsilon pa}{\sqrt{2\pi}\alpha\beta}\exp\left(-\frac{a_\alpha^2}{2}+\frac{A^2}{2B_1}\right)\frac{1}{\sqrt{B_1}}\Big[\cos\varphi-\Gamma_X\frac{a}{2}(\partial_X^2 h)-\Gamma_Y\frac{a}{2}(\partial_Y^2 h)\Big]$$

Makeev wrote this equation up to fourth order (Eq. 32 in his paper). This is where the higher order terms with coefficients Ω and D come from in the final height evolution equation (Eq. 40). We only consider the principal curvatures ($\partial_X^2 h$ and $\partial_Y^2 h$) so second order is all that is needed.

For an isotropic energy distribution ($\alpha = \beta$):

$$\begin{aligned} A &= a_\alpha^2 \sin\varphi \\ B_1 &= a_\alpha^2 \\ B_2 &= a_\alpha^2 \cos\varphi \\ C &= 0 \end{aligned}$$

This produces the following coefficients:

$$\begin{aligned} \Gamma_X(\varphi) &= -\frac{2A}{B_1}\sin\varphi+\frac{B_2}{B_1}\left[1+\frac{A^2}{B_1}\right]\cos\varphi \\ &= -2\ \sin^2\varphi+\left(1+a_\alpha^2\sin^2\varphi\right)\cos^2\varphi \end{aligned}$$

$$\begin{aligned} \Gamma_Y(\varphi) &= \frac{2}{a_\alpha^2}\cos\varphi\left(\frac{B_2}{2}\right) \\ &= \cos^2\varphi \end{aligned}$$

Next, the local velocity v_n needs to be written in terms of the laboratory coordinates (x, y, h). The following approximation is used for powers of derivatives of $h(x, y, t)$ in the local and laboratory frames:

$$\frac{\partial^{n+m} h}{\partial^n X \partial^m Y} \simeq \frac{\partial^{n+m} h}{\partial^n x \partial^m y} \tag{9.31}$$

The unit vector $\hat{n}$ represents the surface normal along Z in the local reference frame (X, Y, Z), and is related to $h(x, y, t)$ as follows:

$$\hat{n} = \frac{(-\partial_x h, -\partial_y h, 1)}{\sqrt{g}} \tag{9.32}$$

where $g \equiv 1 + (\partial_x h)^2 + (\partial_y h)^2$. The unit vector $\hat{m}$ is at an angle θ from the h axis in the laboratory coordinate frame (x, y, h):

$$\hat{m} = (\ sin\theta, 0, \cos\ \theta) \tag{9.33}$$

We write the angle φ in terms of θ by expressing $\cos\varphi$ as the dot product of the unit vectors $\hat{m}$, along the ion trajectory, and $\hat{n}$, along the local normal. The following is obtained, where s = $\sin\theta$ and c = $\cos\theta$:

$$\cos\varphi = \hat{m} \cdot \hat{n} = (s, 0, c) \cdot \frac{(-\partial_x h, -\partial_y h, 1)}{\sqrt{g}} = \frac{c - (\partial_x h)s}{\sqrt{g}}$$

$$\sin\varphi = \left[\frac{s^2 + 2(\partial_x h)sc + (\partial_x h)^2 c^2 + (\partial_y h)^2}{g}\right]^{1/2} \simeq s + (\partial_x h)c - \frac{s}{2}(\partial_x h)^2 + \frac{c^2}{2s}(\partial_y h)^2$$

We expand these expressions in powers of the surface height derivatives using the following approximation method:

$$F\left[(\partial_x h)^2, (\partial_y h)^2\right] = F(0,0) + \left.\frac{\partial F}{\partial\left[(\partial_x h)^2\right]}\right|_{(0,0)} (\partial_x h)^2 + \left.\frac{\partial F}{\partial\left[(\partial_y h)^2\right]}\right|_{(0,0)} (\partial_y h)^2 + ...$$

So applied to $\cos\varphi$ and $\sin\varphi$:

$$\begin{aligned}
\cos\varphi(0,0) &= c - (\partial_x h)s \\
\frac{\partial\left[\cos\varphi\right]}{\partial\left[(\partial_x h)^2\right]} &= \frac{\partial\left[\cos\varphi\right]}{\partial\left[(\partial_y h)^2\right]} = \left[c - (\partial_x h)s\right]\cdot\left(-\frac{1}{2}\right)\left[1 + (\partial_x h)^2 + (\partial_y h)^2\right]^{-3/2} \\
&\qquad @\ (0,0) = -\frac{1}{2}\left[c - (\partial_x h)s\right] \\
\Rightarrow\quad \cos\varphi &\simeq c - (\partial_x h)s - \frac{1}{2}\left[c - (\partial_x h)s\right](\partial_x h)^2 - \frac{1}{2}\left[c - (\partial_x h)s\right](\partial_y h)^2 \\
&\boxed{\cos\varphi \simeq c - (\partial_x h)s - \frac{c}{2}\left[(\partial_x h)^2 + (\partial_y h)^2\right]}
\end{aligned}$$

$$\sin\varphi = \left[\frac{s^2 + 2(\partial_x h)sc + (\partial_x h)^2 c^2 + (\partial_y h)^2}{g}\right]^{1/2} = \left[\frac{\left[s + (\partial_x h)c\right]^2 + (\partial_y h)^2}{g}\right]^{1/2}$$

$$\begin{aligned}
\sin\varphi(0,0) &= \left[(s + (\partial_x h)c)^2\right]^{1/2} = s + (\partial_x h)c \\
\frac{\partial\left[\sin\varphi\right]}{\partial\left[(\partial_x h)^2\right]} &= \frac{1}{2}\left[\frac{s^2 + 2(\partial_x h)sc + (\partial_x h)^2 c^2 + (\partial_y h)^2}{1 + (\partial_x h)^2 + (\partial_y h)^2}\right]^{-\frac{1}{2}} \\
&\qquad \times\left[\frac{c^2\left(1 + (\partial_y h)^2\right) - s^2 - 2(\partial_x h)sc - (\partial_y h)^2}{\left[1 + (\partial_x h)^2 + (\partial_y h)^2\right]^2}\right] \\
&\qquad @\ (0,0) = \frac{1}{2}\,\frac{c^2 - s^2 - 2(\partial_x h)sc}{\sqrt{s^2 + (\partial_x h)sc}} \approx \frac{c^2}{2s} - \frac{s}{2} \\
\Rightarrow\quad \sin\varphi &\simeq s + (\partial_x h)c + \left(\frac{c^2}{2s} - \frac{s}{2}\right)\left[(\partial_x h)^2 + (\partial_y h)^2\right]
\end{aligned}$$

Therefore

$$\begin{aligned}
\cos^2\varphi &\simeq s^2 + (\partial_x h)(2sc) + (\partial_x h)^2(c^2 - s^2) + (\partial_y h)^2(c^2) \\
\sin^2\varphi &\simeq c^2 + (\partial_x h)(-2sc) + (\partial_x h)^2(s^2 - c^2) + (\partial_y h)^2(-c^2)
\end{aligned}$$

Substituting the expressions for $\sin\varphi$ and $\cos\varphi$ into the Γ functions, and ignoring higher

order nonlinearities (above 2^{nd} order), the following is obtained:

$$\begin{aligned}
\Gamma_X(\theta) = &-2\left[s^2 + (\partial_x h)(2sc) + (\partial_x h)^2(c^2 - s^2) + (\partial_y h)^2(c^2)\right] \\
&+ \left(1 + a_\alpha^2\left[s^2 + (\partial_x h)(2sc) + (\partial_x h)^2(c^2 - s^2) + (\partial_y h)^2(c^2)\right]\right) \\
&\quad \times \left[c^2 + (\partial_x h)(-2sc) + (\partial_x h)^2(s^2 - c^2) + (\partial_y h)^2(-c^2)\right] \\
= &-2s^2 + c^2 + a_\alpha s^2 c^2 \\
&+ (\partial_x h)(-6sc - 2a_\alpha s^3 c + 2a_\alpha s c^3) \\
&+ (\partial_x h)^2(3s^2 - 3c^2 + a_\alpha s^4 - 6a_\alpha s^2 c^2 + a_\alpha c^4) \\
&+ (\partial_y h)^2(-3c^2 - a_\alpha s^2 c^2 + a_\alpha c^4)
\end{aligned}$$

$$\Gamma_Y(\theta) = c^2 + (\partial_x h)(-2sc) + (\partial_x h)^2(s^2 - c^2) + (\partial_y h)^2(-c^2)$$

Since these will be multiplied by a second order term, we can ignore all terms above 0^{th} order:

$$\begin{aligned}
\Gamma_X(\theta) &= -2s^2 + c^2 + a_\alpha s^2 c^2 \\
\Gamma_Y(\theta) &= c^2
\end{aligned}$$

Revisiting the velocity equation:

$$v_n = \frac{J\epsilon pa}{\sqrt{2\pi}\alpha\beta}\exp\left(-\frac{a_\alpha^2}{2} + \frac{A^2}{2B_1}\right)\frac{1}{\sqrt{B_1}}\Big[\cos\varphi - \Gamma_X\frac{a}{2}(\partial_X^2 h) - \Gamma_Y\frac{a}{2}(\partial_Y^2 h)\Big]$$

We know that

$$B_1^{-1/2} \simeq \frac{1}{a_\alpha}$$

Relating φ with θ in the exponential and ignoring nonlinearities above 2^{nd} order, we can say:

$$\exp\left(\frac{A^2}{2B_1}\right) = \exp\left(\frac{a_\alpha^2 \sin^2\varphi}{2}\right) \simeq \exp\left[\frac{a_\alpha^2}{2}\left(s^2 + (\partial_x h)(2sc) + (\partial_x h)^2(c^2 - s^2) + (\partial_y h)^2(c^2)\right)\right]$$
$$= \exp\left[\frac{a_\alpha^2 s^2}{2}\right] \exp\left[a_\alpha^2(\partial_x h)(2sc) + a_\alpha^2(\partial_x h)^2(c^2 - s^2) + a_\alpha^2(\partial_y h)^2(c^2)\right]$$

Using the Taylor series approximation $e^x = 1 + x$:

$$= \exp\left[\frac{a_\alpha^2 s^2}{2}\right] \left\{1 + a_\alpha^2(\partial_x h)(2sc) + a_\alpha^2(\partial_x h)^2(c^2 - s^2) + a_\alpha^2(\partial_y h)^2(c^2)\right\}$$

This results in:

$$v_n = \frac{J\epsilon p a_\alpha}{\sqrt{2\pi}\alpha} \exp\left(\frac{a_\alpha^2\,(s^2 - 1)}{2}\right) \frac{1}{a_\alpha} \left\{1 + a_\alpha^2(\partial_x h)(2sc) + a_\alpha^2(\partial_x h)^2(c^2 - s^2) + a_\alpha^2(\partial_y h)^2(c^2)\right\}$$
$$\times \left[c - (\partial_x h)s - \frac{c}{2}\left[(\partial_x h)^2 + (\partial_y h)^2\right] + \left(2s^2 - c^2 - a_\alpha^2 s^2 c^2\right)\frac{a}{2}(\partial_x^2 h) - c^2\frac{a}{2}(\partial_y^2 h)\right]$$

This simplifies to:

$$v_n = F\left\{1 + a_\alpha^2(\partial_x h)(2sc) + a_\alpha^2(\partial_x h)^2(c^2 - s^2) + a_\alpha^2(\partial_y h)^2(c^2)\right\}$$
$$\times \left[c - (\partial_x h)s - \frac{c}{2}\left[(\partial_x h)^2 + (\partial_y h)^2\right] + \left(2s^2 - c^2 - a_\alpha^2 s^2 c^2\right)\frac{a}{2}(\partial_x^2 h) - c^2\frac{a}{2}(\partial_y^2 h)\right]$$
$$= \frac{Fa}{2}\left((2s^2 - c^2 - a_\alpha^2 s^2 c^2)(\partial_x^2 h) - c^2(\partial_y^2 h)\right)$$
$$+ Fc + F(\partial_x h)(2a_\alpha^2 sc^2 - s) + F(\partial_x h)^2\left(-\frac{c}{2} + a_\alpha^2 c^3 - a_\alpha^2 s^2 c\right)$$
$$+ F(\partial_y h)^2\left(-\frac{c}{2} + a_\alpha^2 c^3\right)$$

and projecting along the h-axis:

$$\partial_t h = v_n\sqrt{g} = v_n\sqrt{1 + (\partial_x h)^2 + (\partial_y h)^2}$$

Expanding this for small slopes:

$$\begin{aligned}\partial_t h =& Fs(\partial_x h)(c^2(a_\alpha^2-1)-s^2)+\frac{Fa}{2}\left((2s^2-c^2-a_\alpha^2 s^2c^2)(\partial_x^2 h)-c^2(\partial_y^2 h)\right)\\ &+\frac{Fa_\alpha^2}{2}c\left((3s^2-c^2-a_\alpha^2 s^2c^2)(\partial_x h)^2-c^2(\partial_y h)^2\right)\end{aligned}$$

Where

$$F=\frac{J\epsilon p}{\sqrt{2\pi}\alpha}\exp\left(-\frac{a_\alpha^2 c^2}{2}\right)$$

NOTE: Makeev's projection defines v_n to 4^{th} order derivatives, while we only expand to 2^{nd} order derivatives. Therefore, his final equation includes higher order terms (i.e. with coefficients Ω and D). We also ignore nonlinearities above first order (Makeev has terms with coefficient ξ).

Therefore, the higher order terms are not results of the expansion itself, but of the approximation for v_n going up to higher orders.

9.3 Appendix C

Full 4x4 Gaussian bump evolution (corresponding to Figure 7.7):

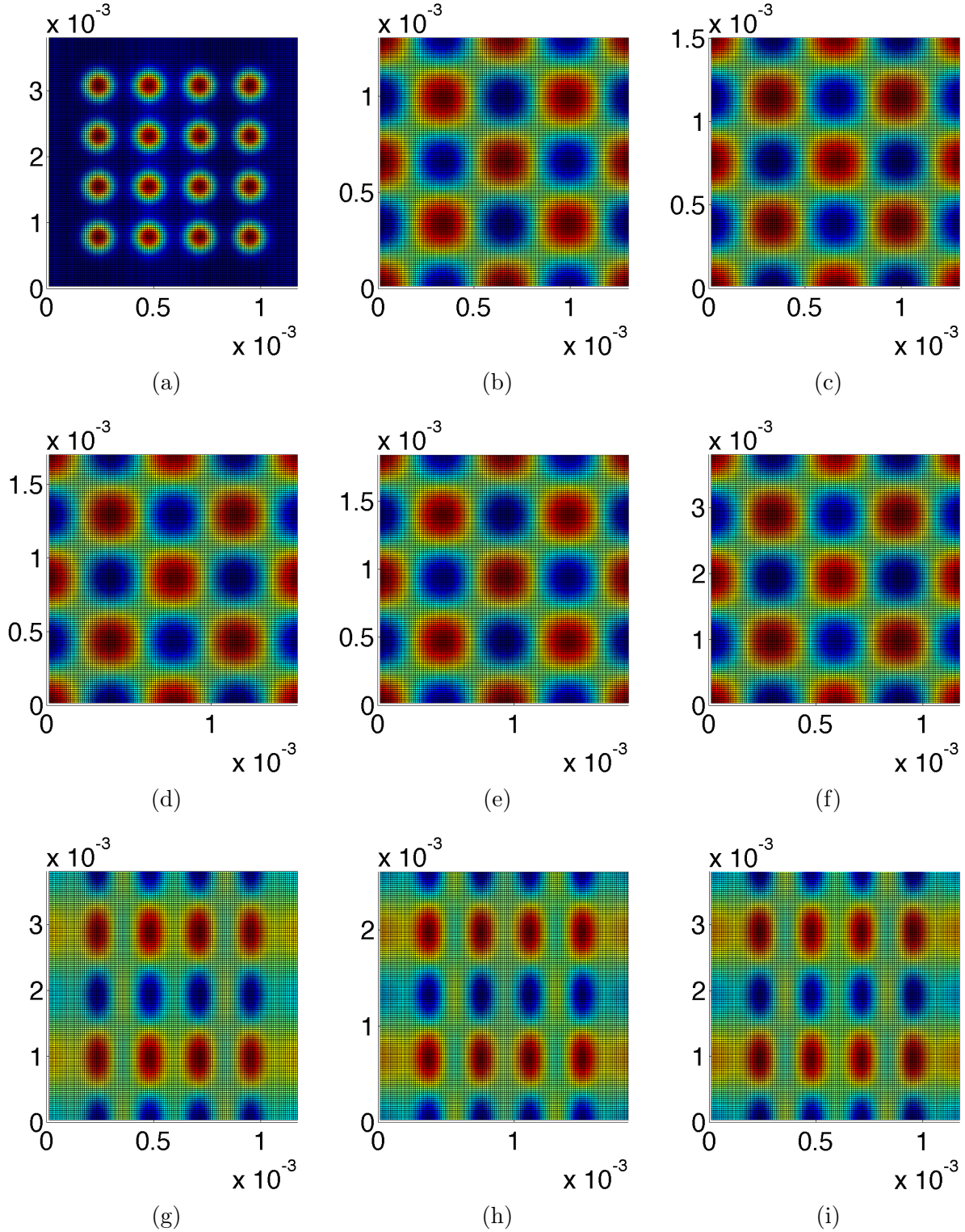

Figure 9.1: Contour plots of evolved surface for linear evolution. Surface2: $h = sin(\omega x)cos(\omega y)$, $\omega = 3.2$. Original Surface (a). Angle of incidence: (b) 0° (c) 30° (d) 40° (e) 45° (f) 50° (g) 55° (h) 60° (i) 70°

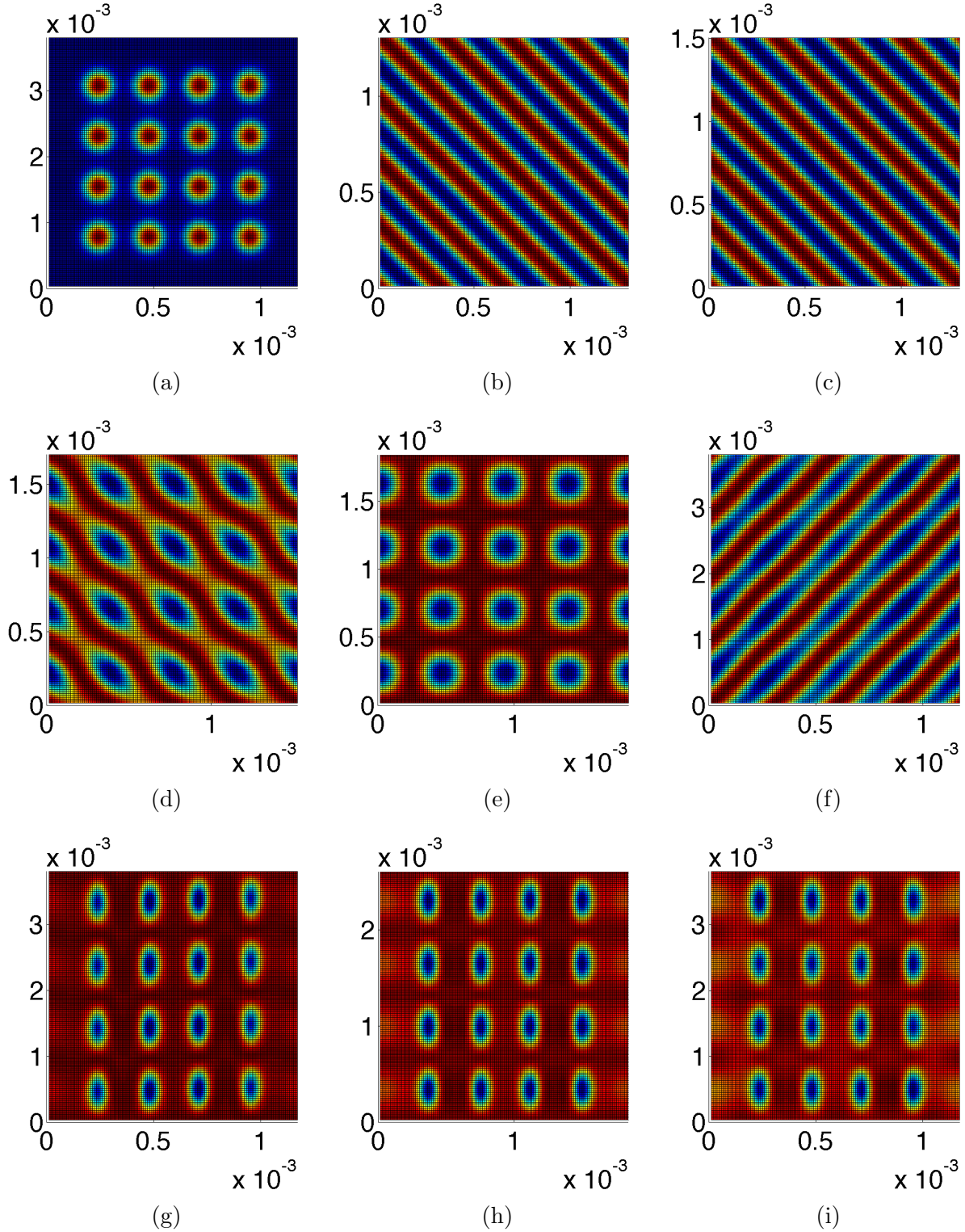

Figure 9.2: Contour plots of evolved surface for nonlinear evolution. Original Surface (a). Original Surface (a). Angle of incidence: (b) 0° (c) 30° (d) 40° (e) 45° (f) 50° (g) 55° (h) 60° (i) 70°

FFT spectral analysis plots corresponding to above contour plots (Figures 9.1 and 9.2):

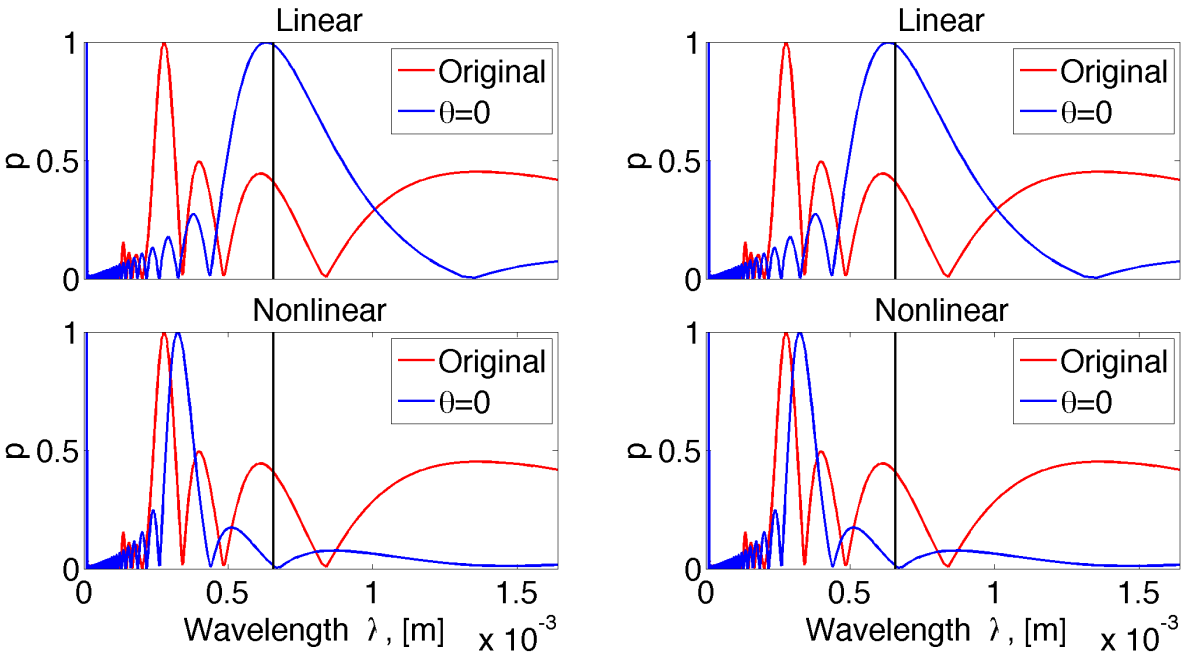

(a) (b)

Figure 9.3: FFT Spectral analysis for Surface2, $\theta = 0°$.

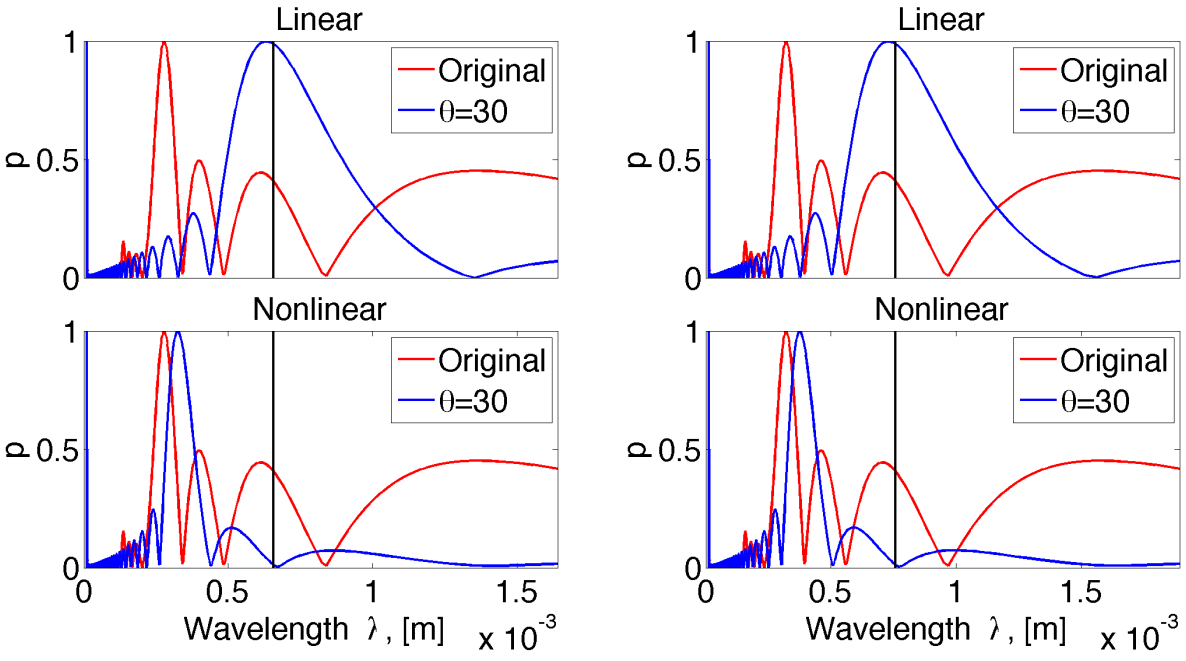

(a) (b)

Figure 9.4: FFT Spectral analysis for Surface2, $\theta = 30°$.

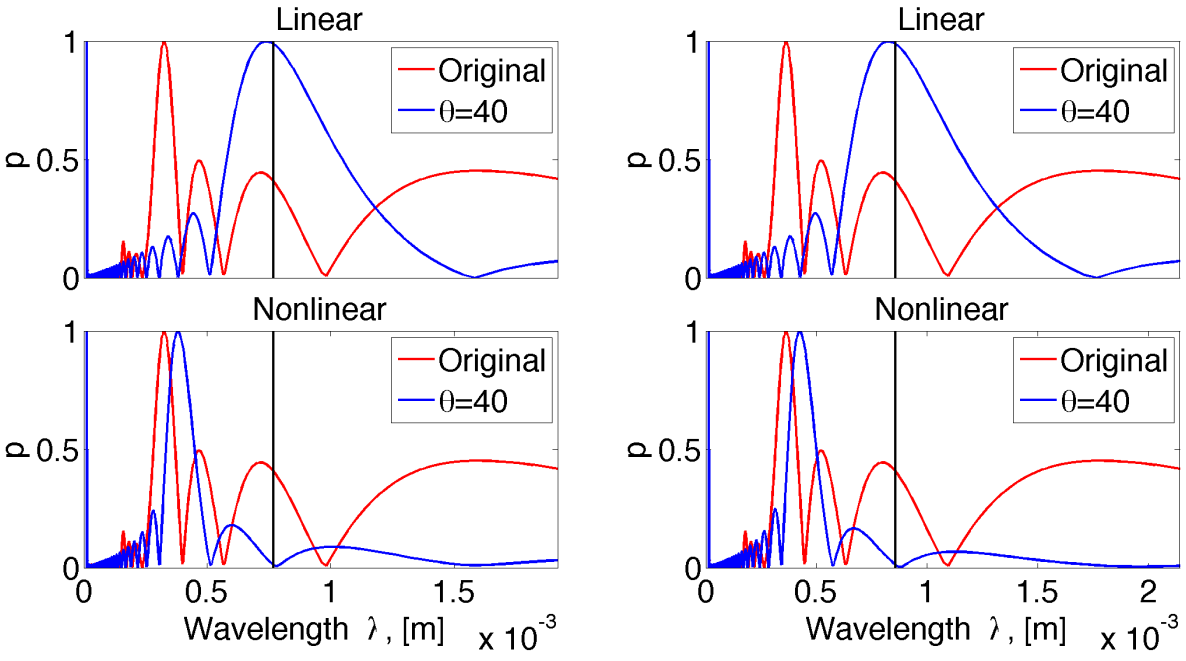

(a) (b)

Figure 9.5: FFT Spectral analysis for Surface2, $\theta = 40°$.

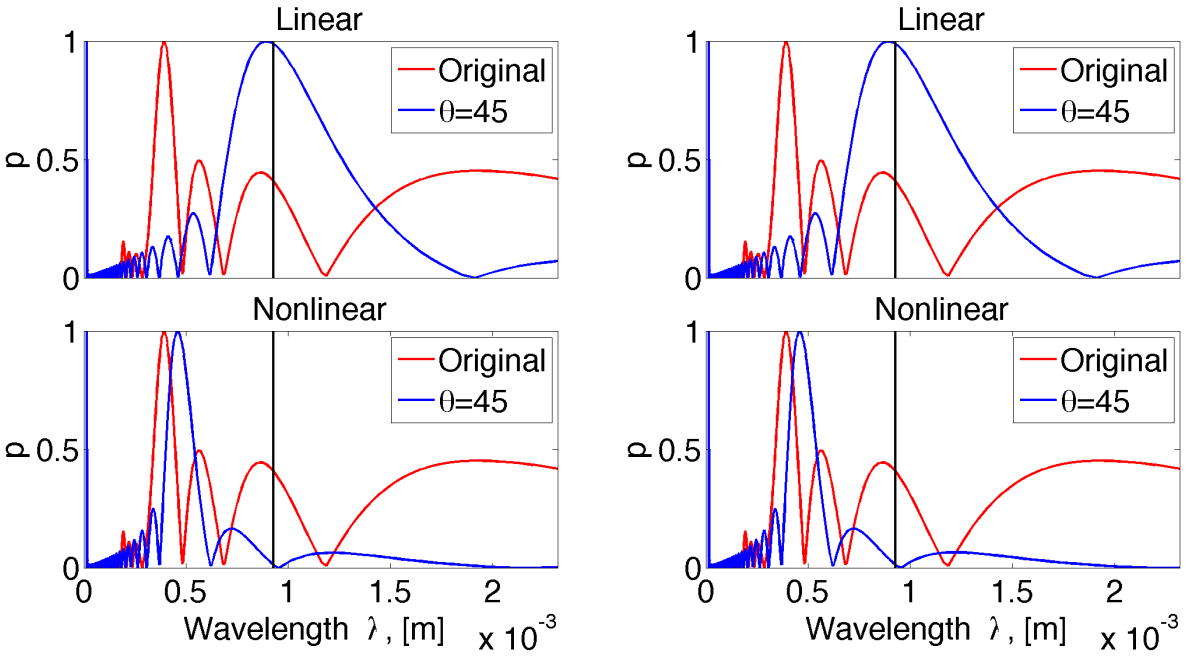

(a) (b)

Figure 9.6: FFT Spectral analysis for Surface2, $\theta = 45°$.

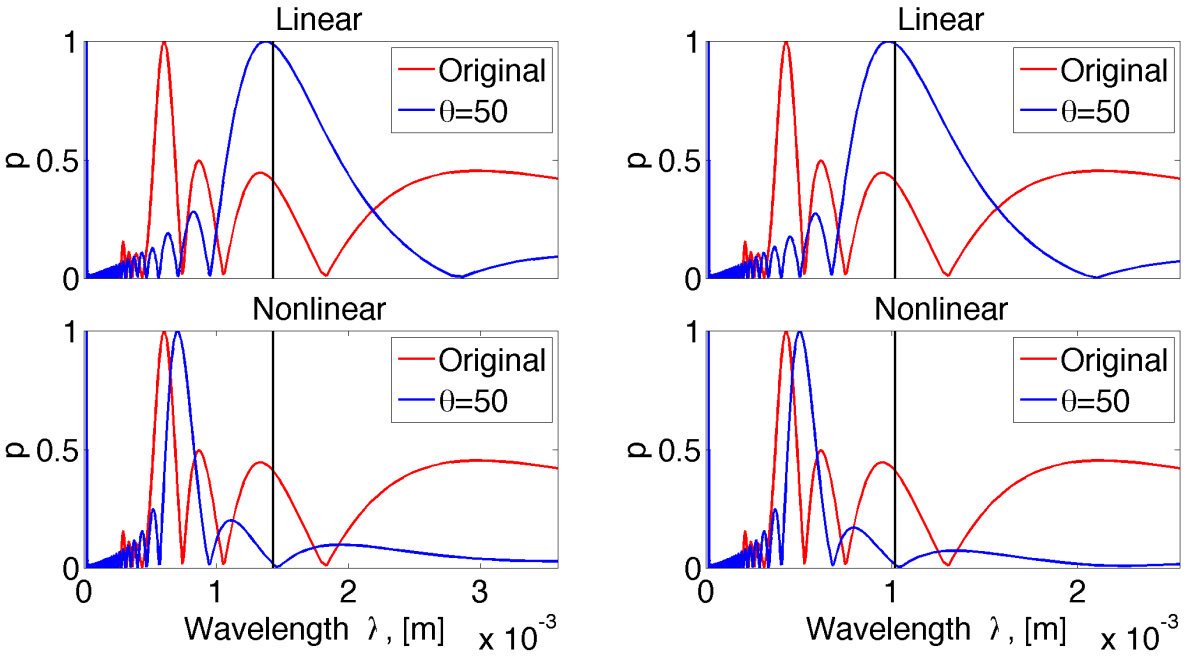

(a) (b)

Figure 9.7: FFT Spectral analysis for Surface2, $\theta = 50°$.

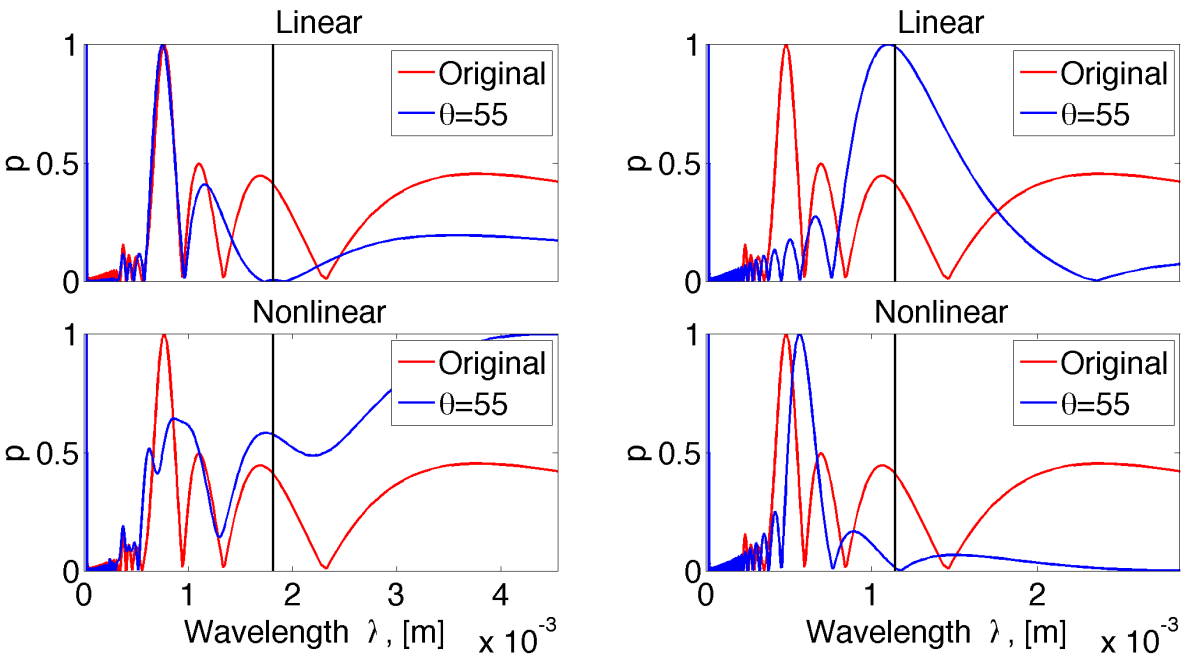

(a) (b)

Figure 9.8: FFT Spectral analysis for Surface2, $\theta = 55°$.

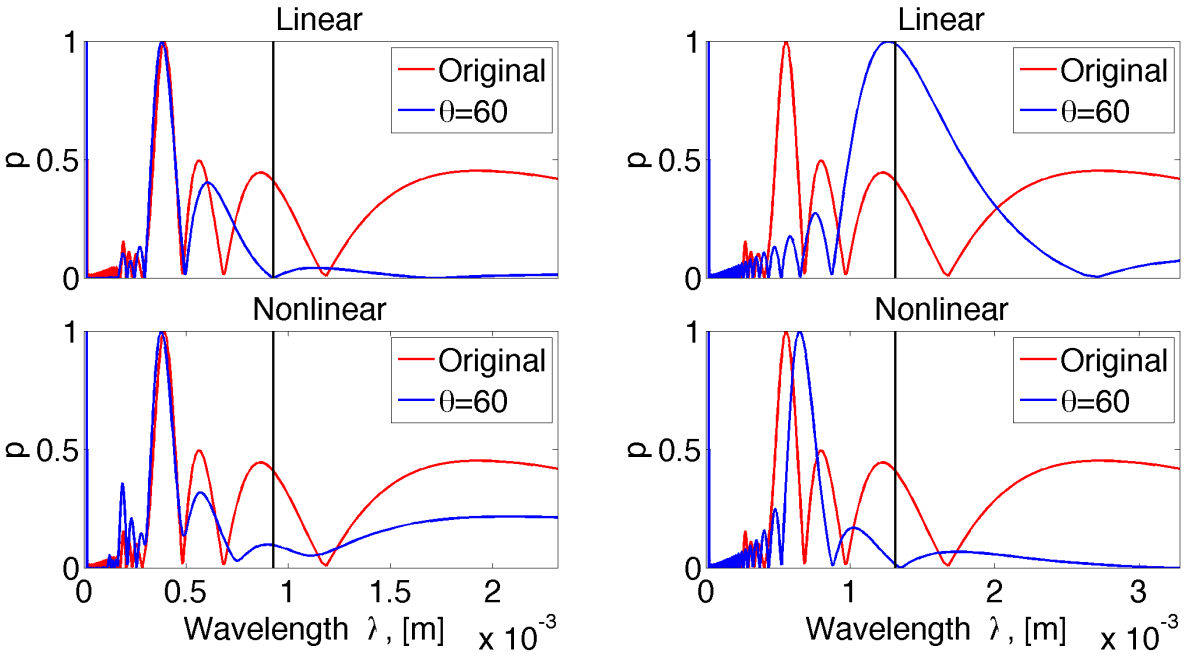

(a) (b)

Figure 9.9: FFT Spectral analysis for Surface2, $\theta = 60°$.

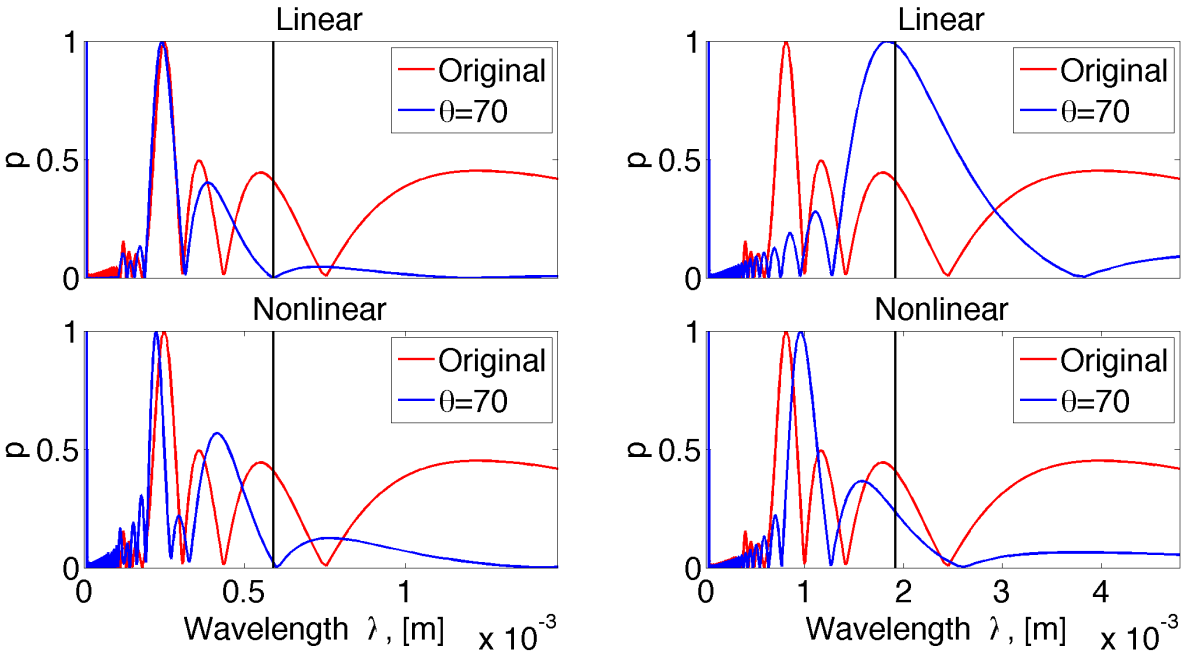

(a) (b)

Figure 9.10: FFT Spectral analysis for Surface2, $\theta = 70°$.

9.4 Appendix D

The following is for sinusoidal "eggshell" pattern initial conditions ($h = sin(\omega x)cos(\omega y)$), corresponding to the results presented in Section 7.4.

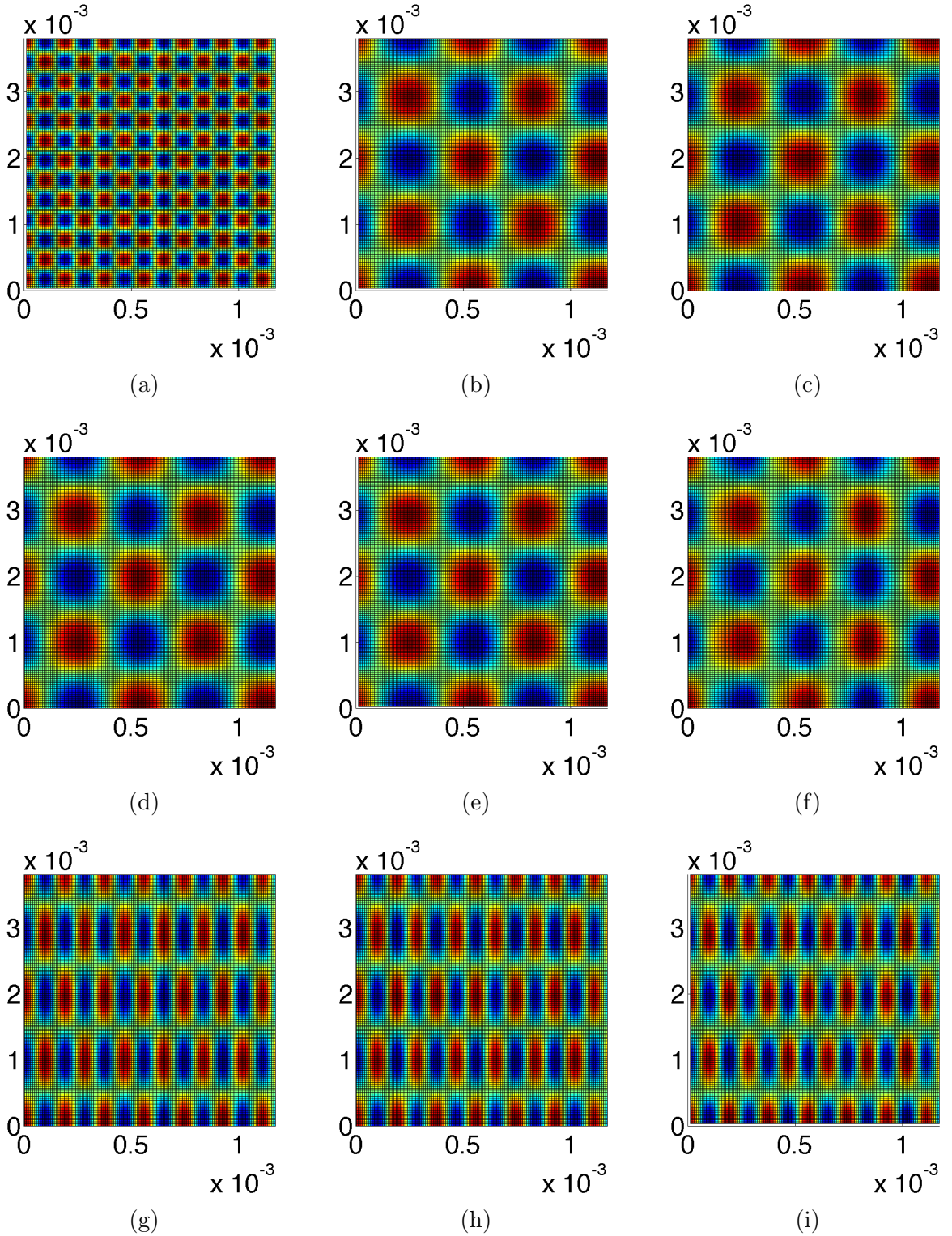

Figure 9.11: Contour plots of evolved surface for undamped linear evolution. Surface1: $h = sin(\omega x)cos(\omega y)$, $\omega = 3.2$. Original Surface (a). Angle of incidence: (b) 0° (c) 30° (d) 40° (e) 45° (f) 50° (g) 55° (h) 60° (i) 70°

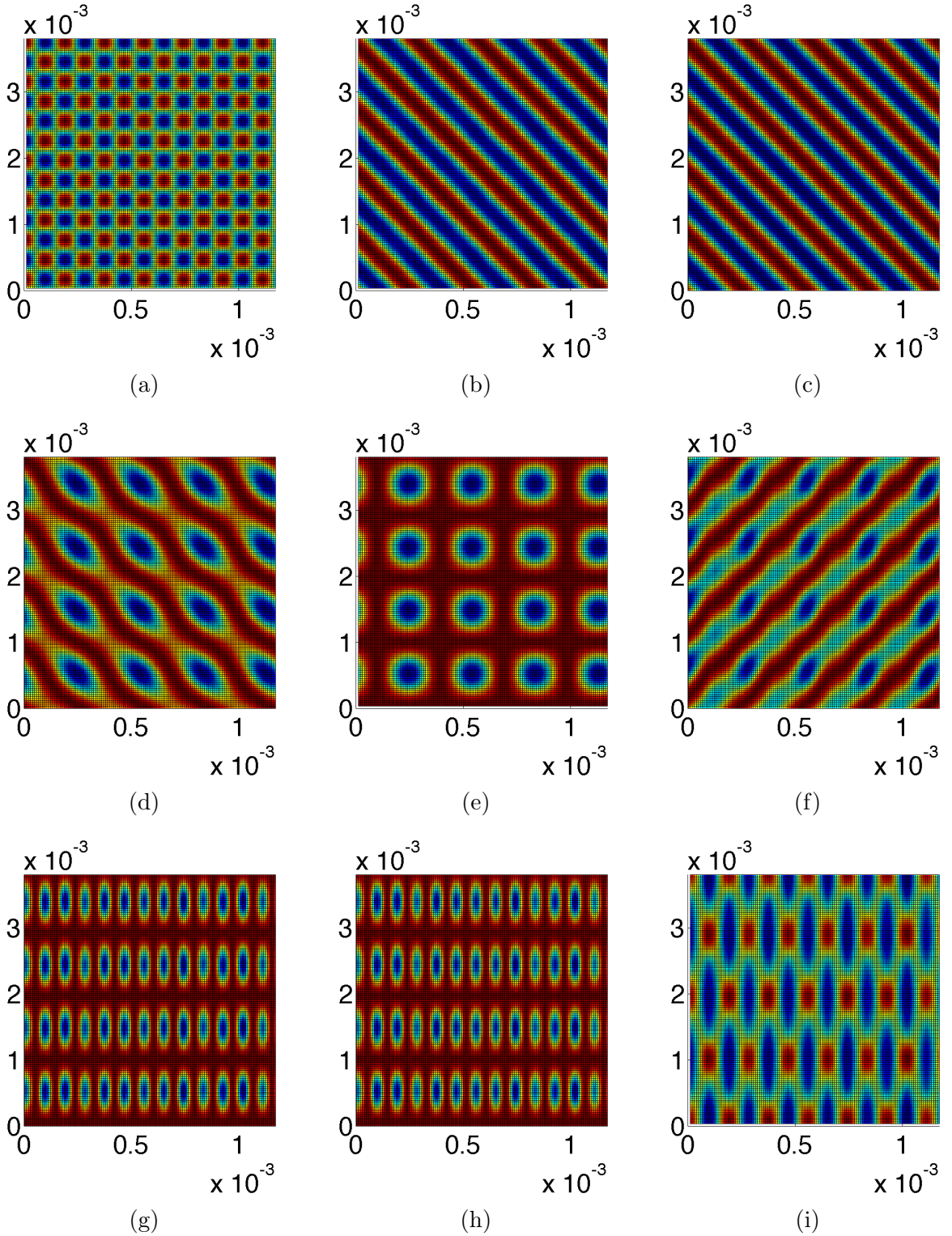

Figure 9.12: Contour plots of evolved surface for undamped nonlinear evolution. Original Surface (a). Original Surface (a). Angle of incidence: (b) 0° (c) 30° (d) 40° (e) 45° (f) 50° (g) 55° (h) 60° (i) 70°

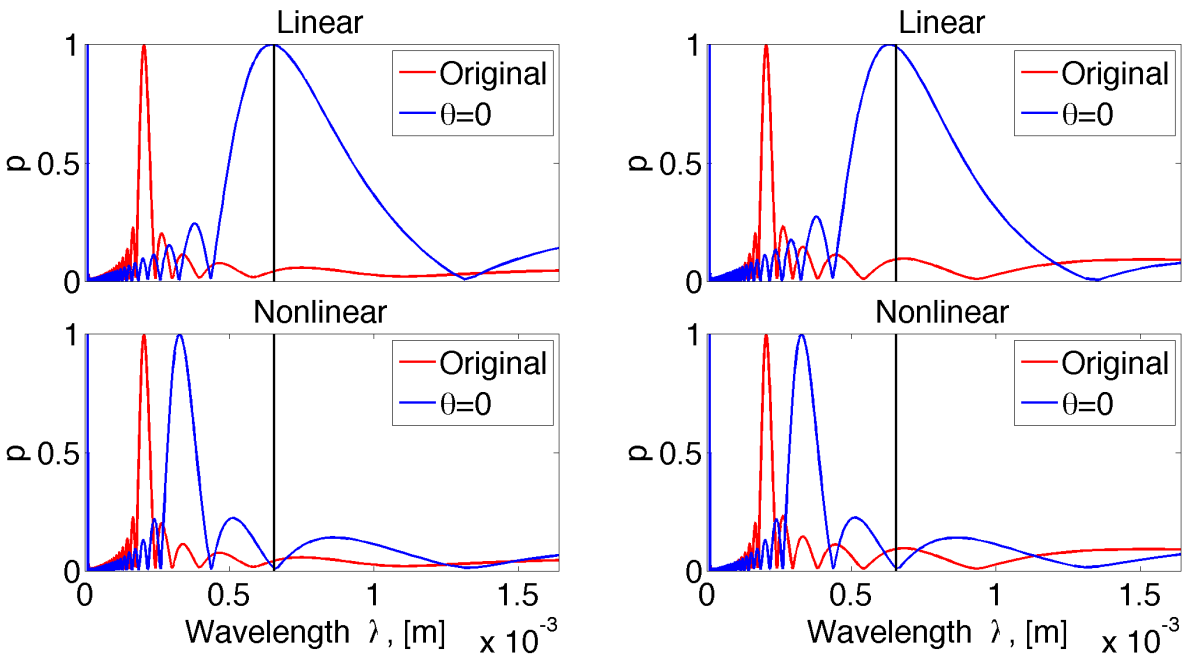

(a) (b)

Figure 9.13: FFT Spectral analysis for initial profile h =sin(ωx)cos(ωy), $\theta = 0°$, undamped.

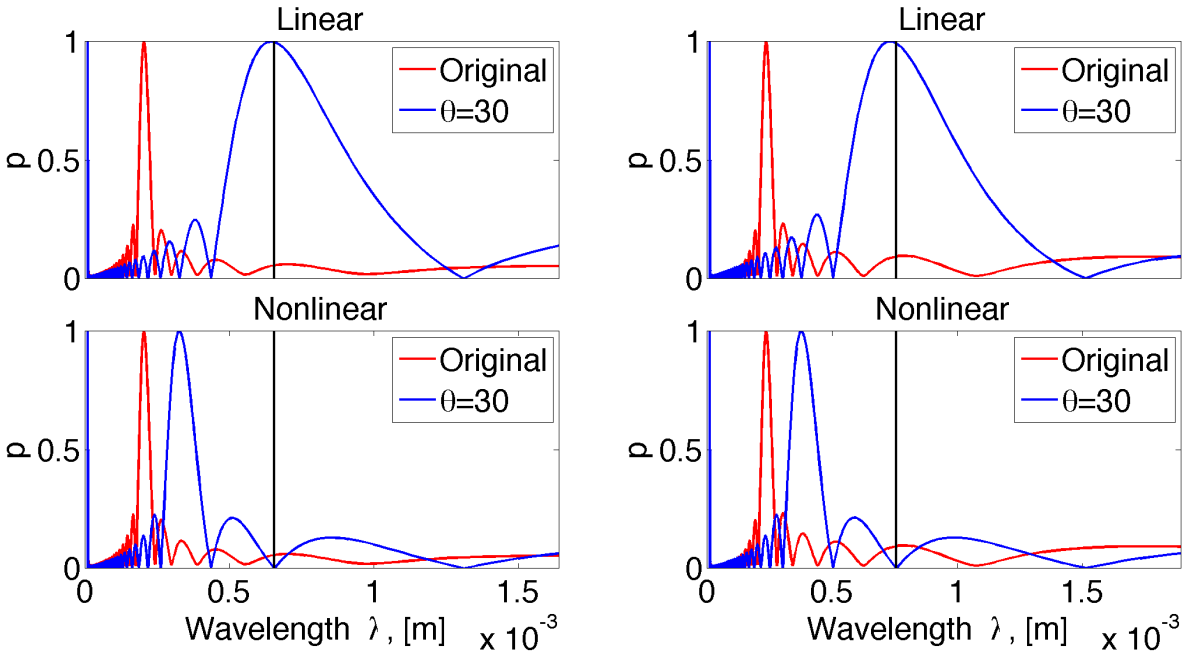

(a) (b)

Figure 9.14: FFT Spectral analysis for initial profile h =sin(ωx)cos(ωy), $\theta = 30°$, undamped.

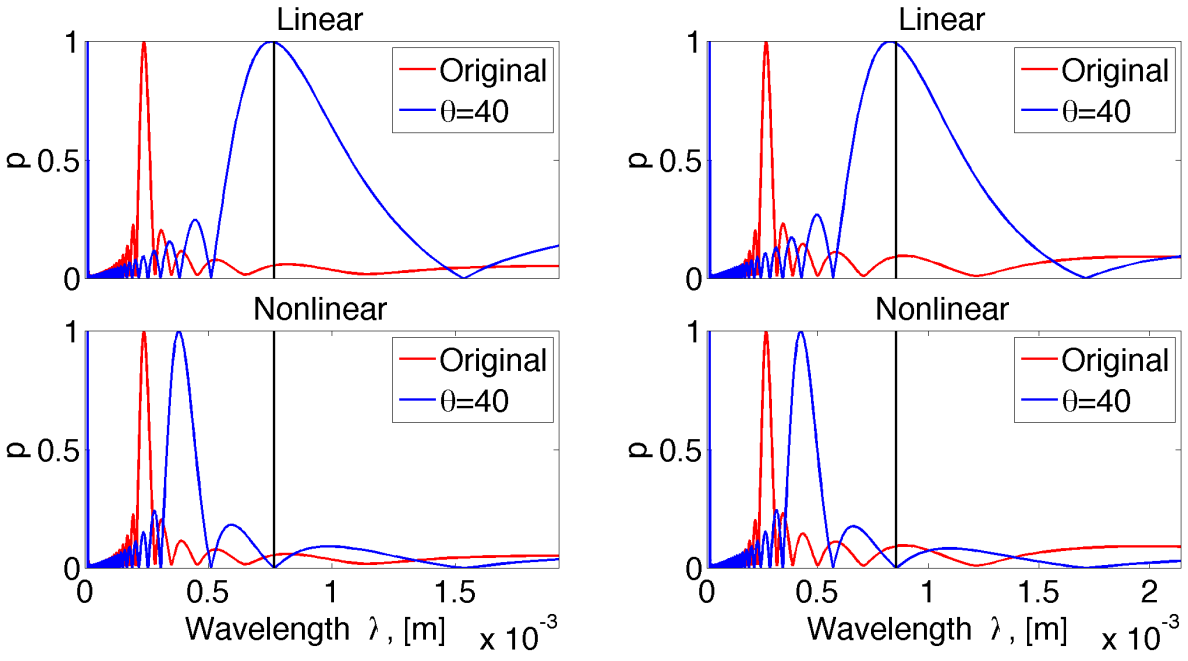

(a) (b)

Figure 9.15: FFT Spectral analysis for initial profile h =sin(ωx)cos(ωy), $\theta = 40°$, undamped.

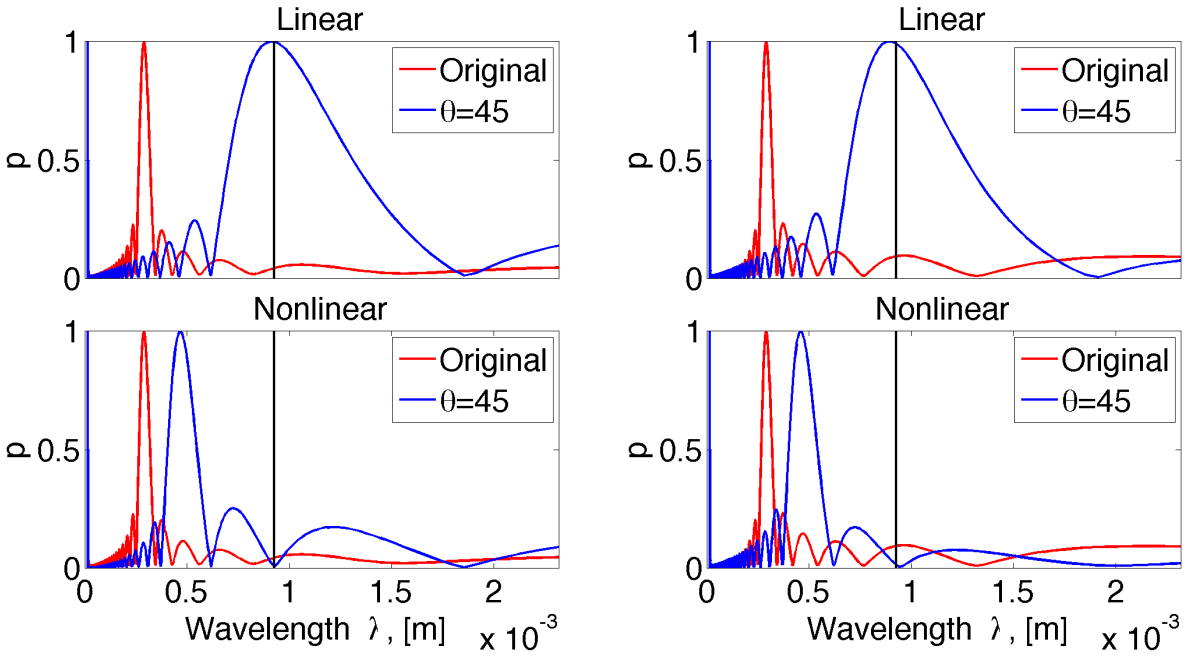

(a) (b)

Figure 9.16: FFT Spectral analysis for initial profile h =sin(ωx)cos(ωy), $\theta = 45°$, undamped.

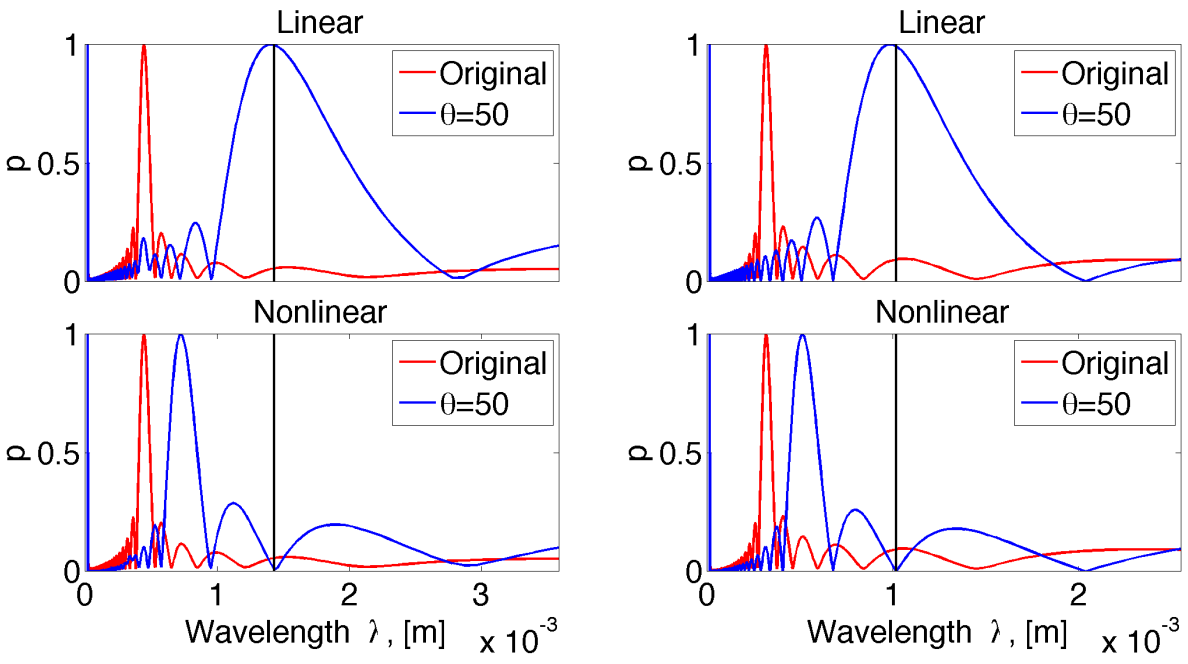

(a) (b)

Figure 9.17: FFT Spectral analysis for initial profile h =sin(ωx)cos(ωy), $\theta = 50°$, undamped.

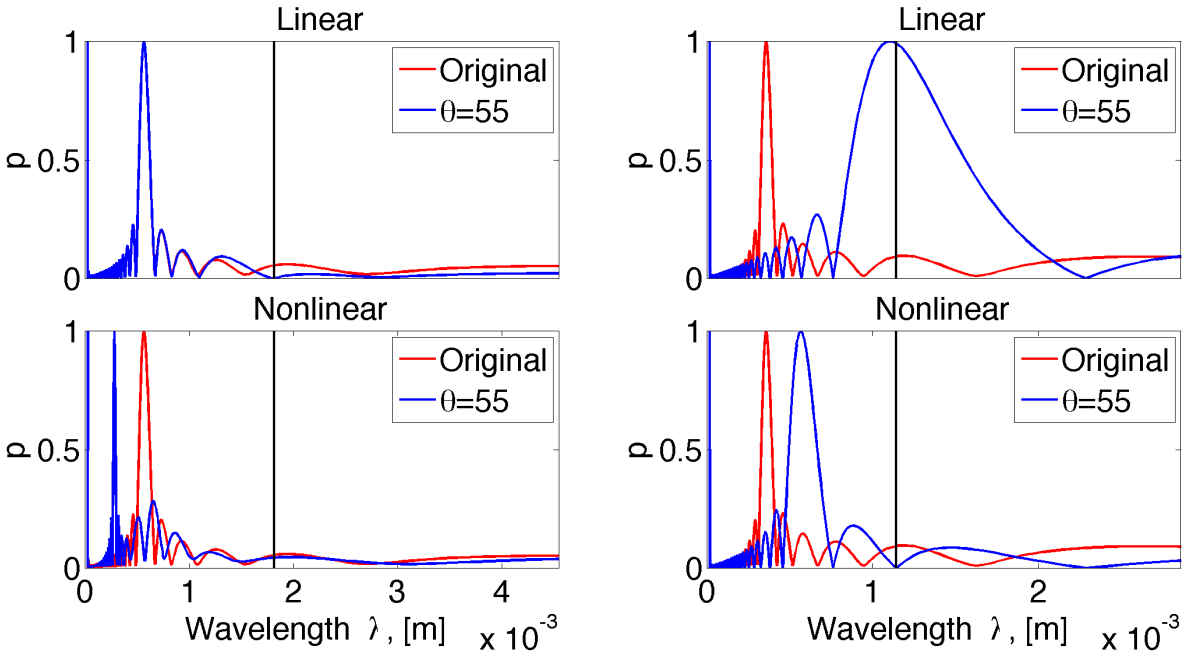

(a) (b)

Figure 9.18: FFT Spectral analysis for initial profile h =sin(ωx)cos(ωy), $\theta = 55°$, undamped.

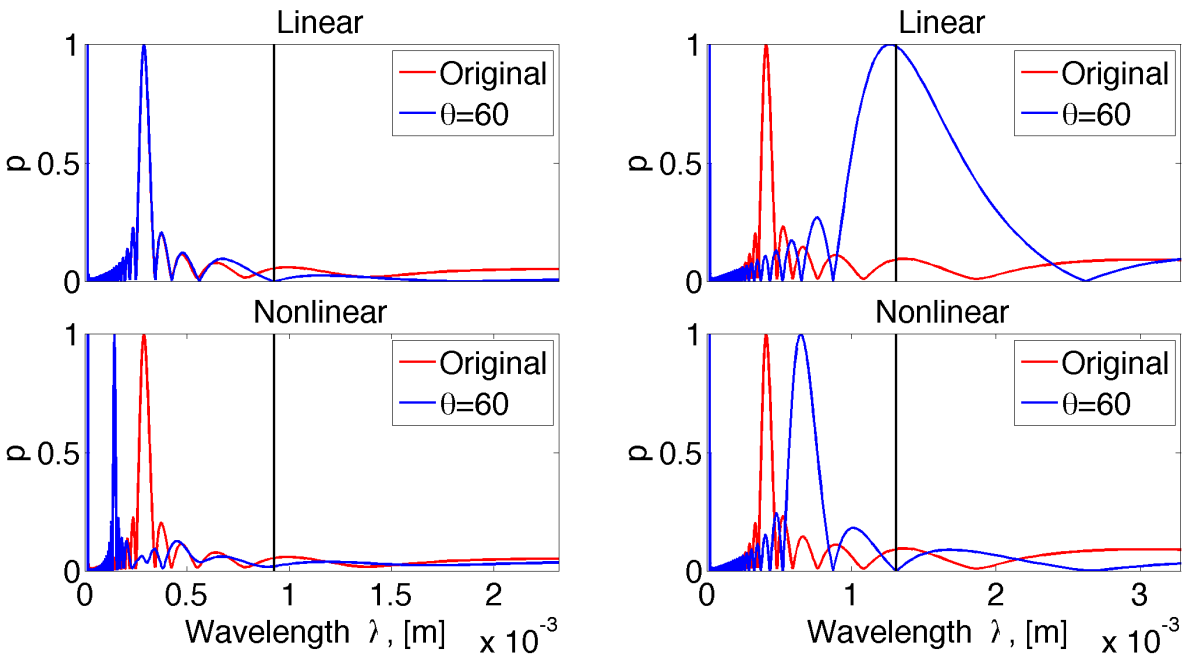

(a) (b)

Figure 9.19: FFT Spectral analysis for initial profile h =sin(ωx)cos(ωy), $\theta = 60°$, undamped.

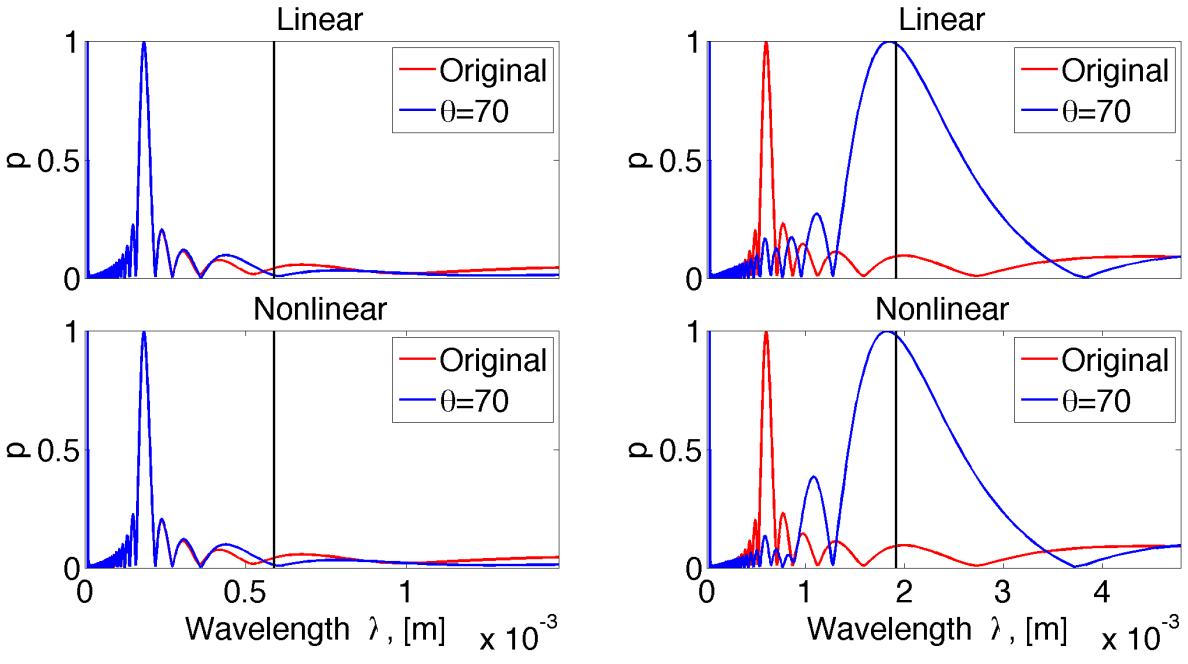

(a) (b)

Figure 9.20: FFT Spectral analysis for initial profile h =sin(ωx)cos(ωy), $\theta = 70°$, undamped.

The following is for the identical initial conditions ($h = sin(\omega x)cos(\omega y)$), but with the damping term included

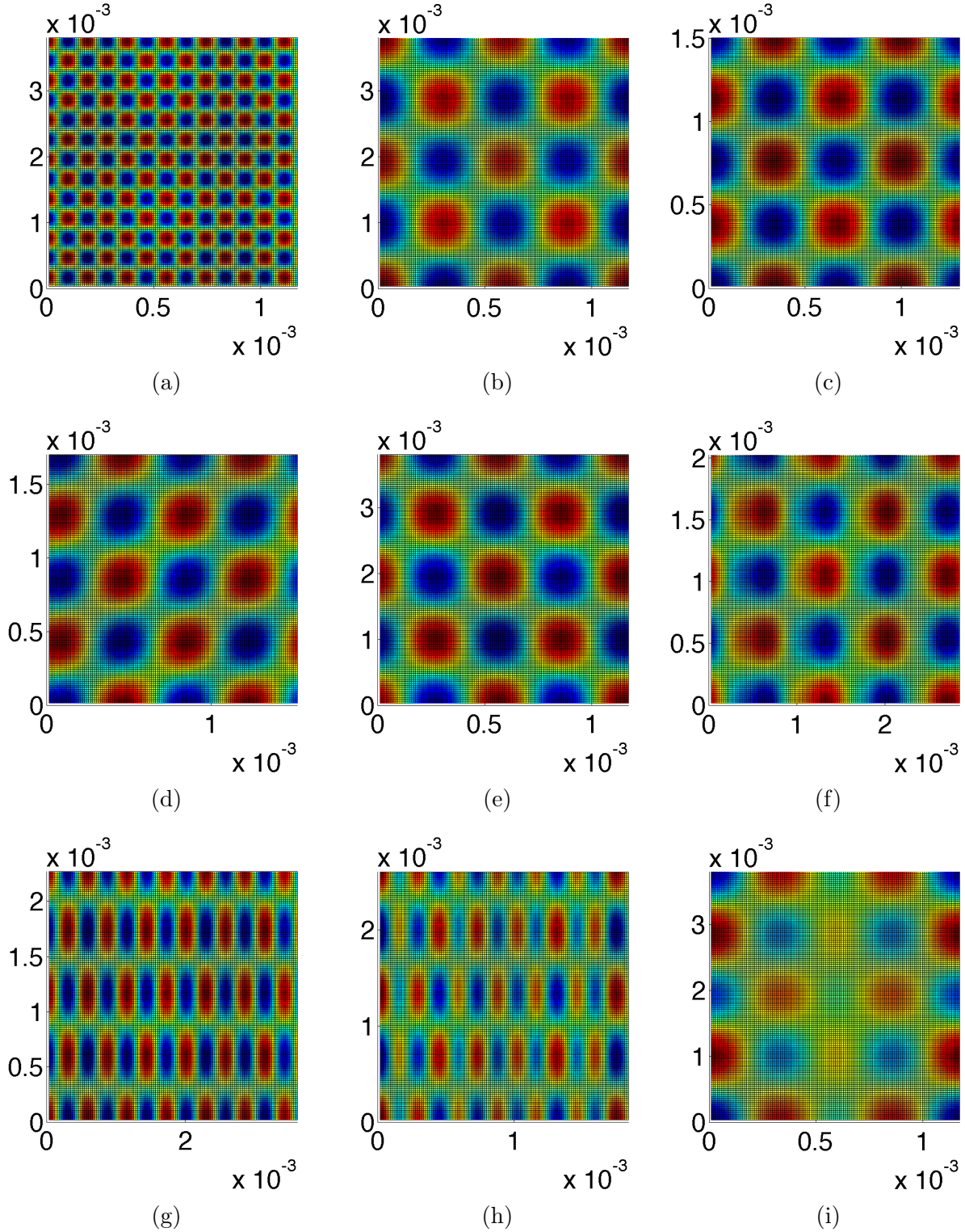

Figure 9.21: Contour plots of evolved surface for damped linear evolution. Damped1: $h = sin(\omega x)cos(\omega y)$, $\omega = 3.2$. Original Surface (a). Angle of incidence: (b) 0° (c) 30° (d) 40° (e) 45° (f) 50° (g) 55° (h) 60° (i) 70°

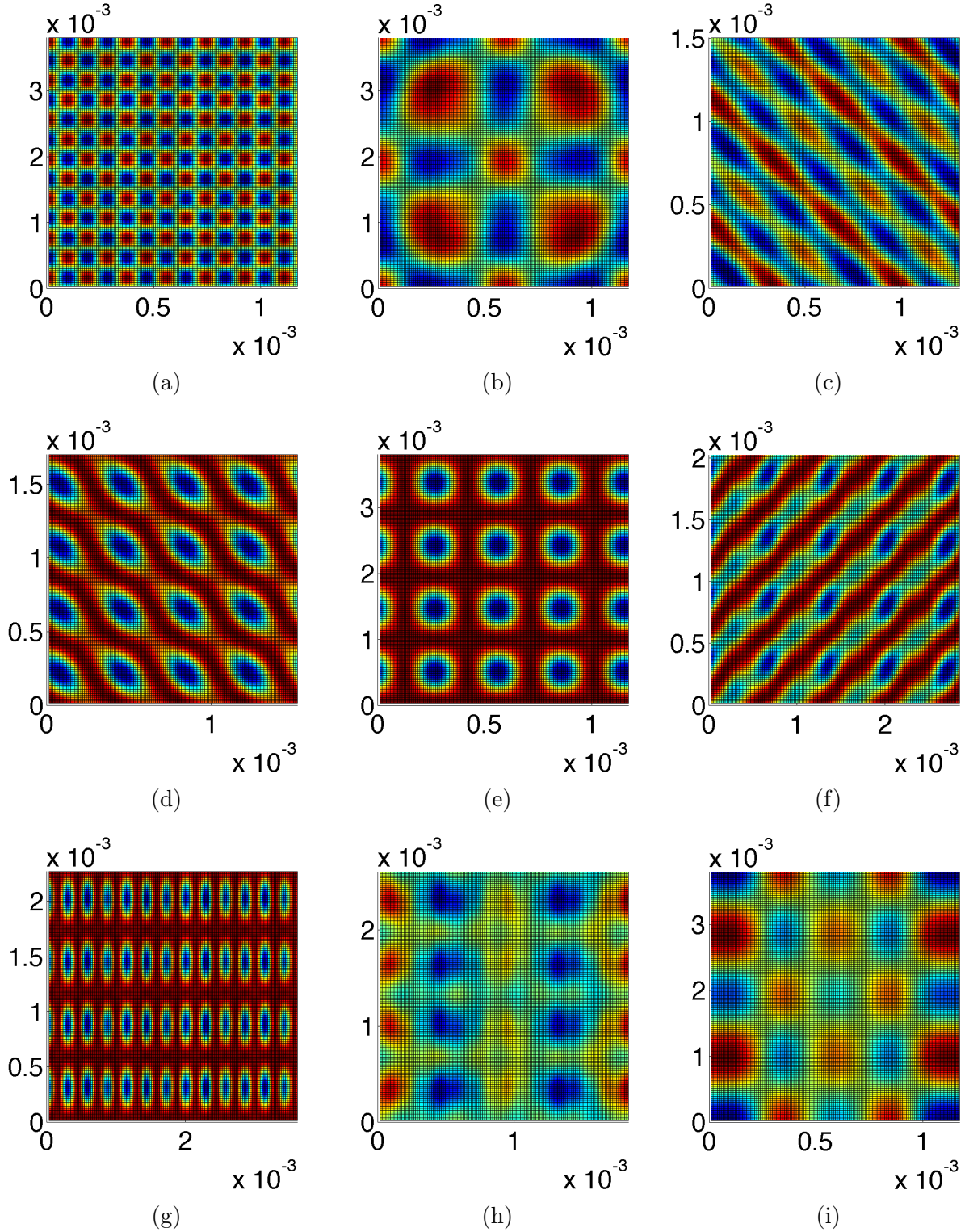

Figure 9.22: Contour plots of evolved surface for damped nonlinear evolution. Original Surface (a). Original Surface (a). Angle of incidence: (b) 0° (c) 30° (d) 40° (e) 45° (f) 50° (g) 55° (h) 60° (i) 70°

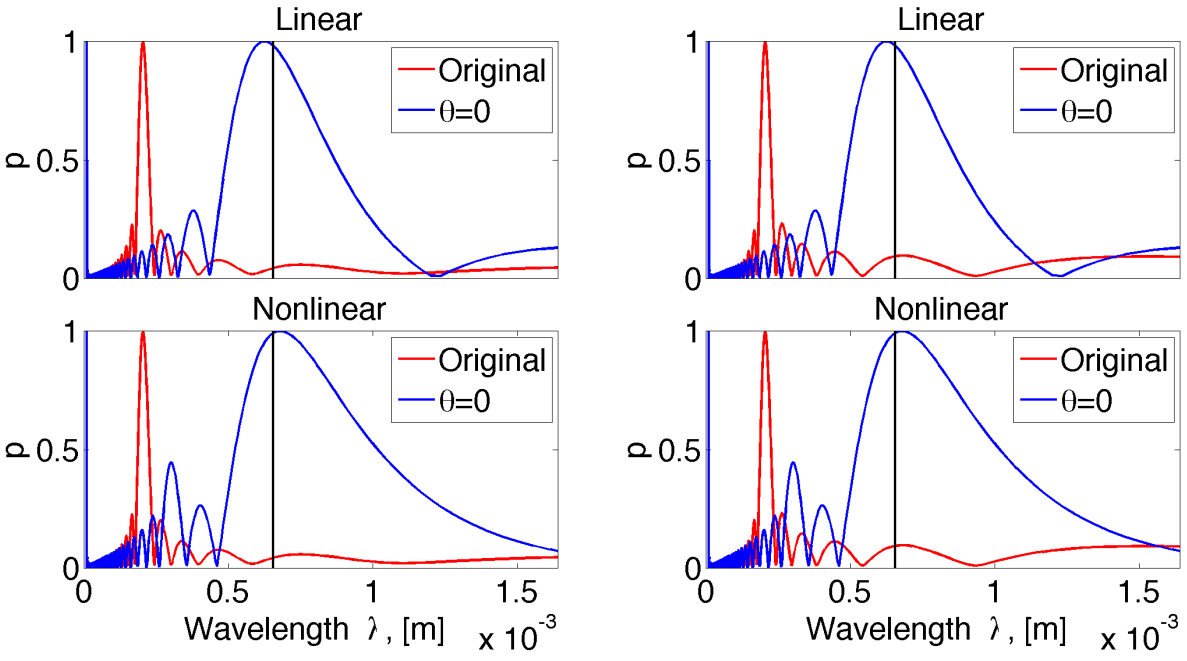

(a) (b)

Figure 9.23: FFT Spectral analysis of damped evolution for Surface1, $\theta = 0°$, damped.

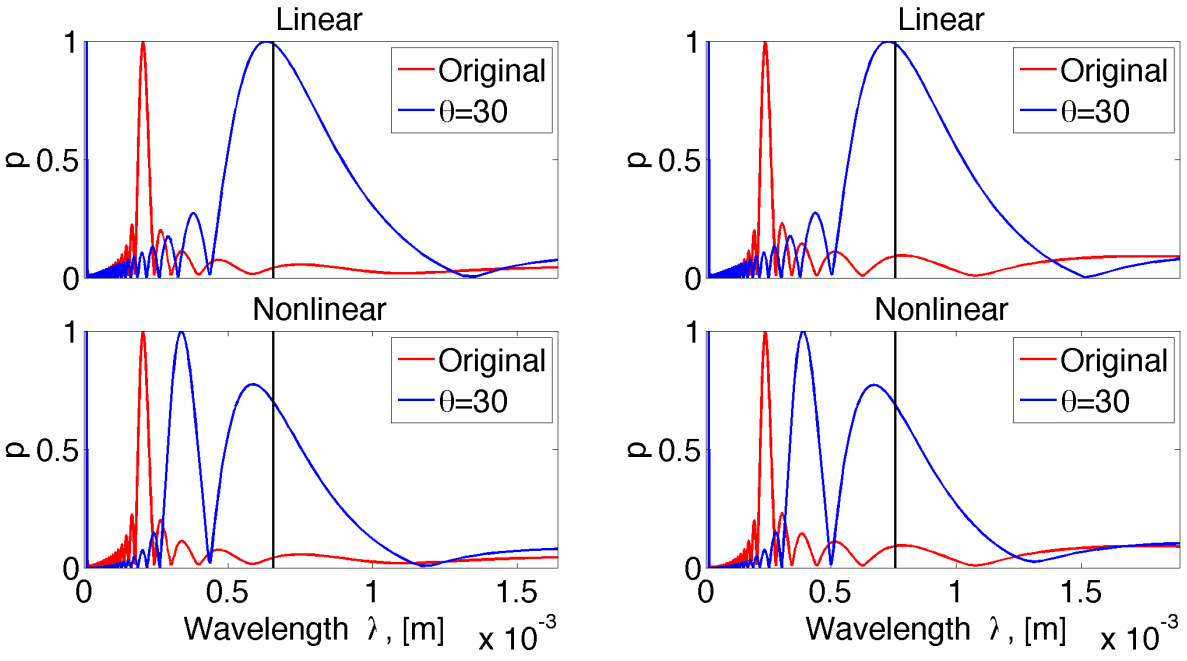

(a) (b)

Figure 9.24: FFT Spectral analysis of damped evolution for Surface1, $\theta = 30°$, damped.

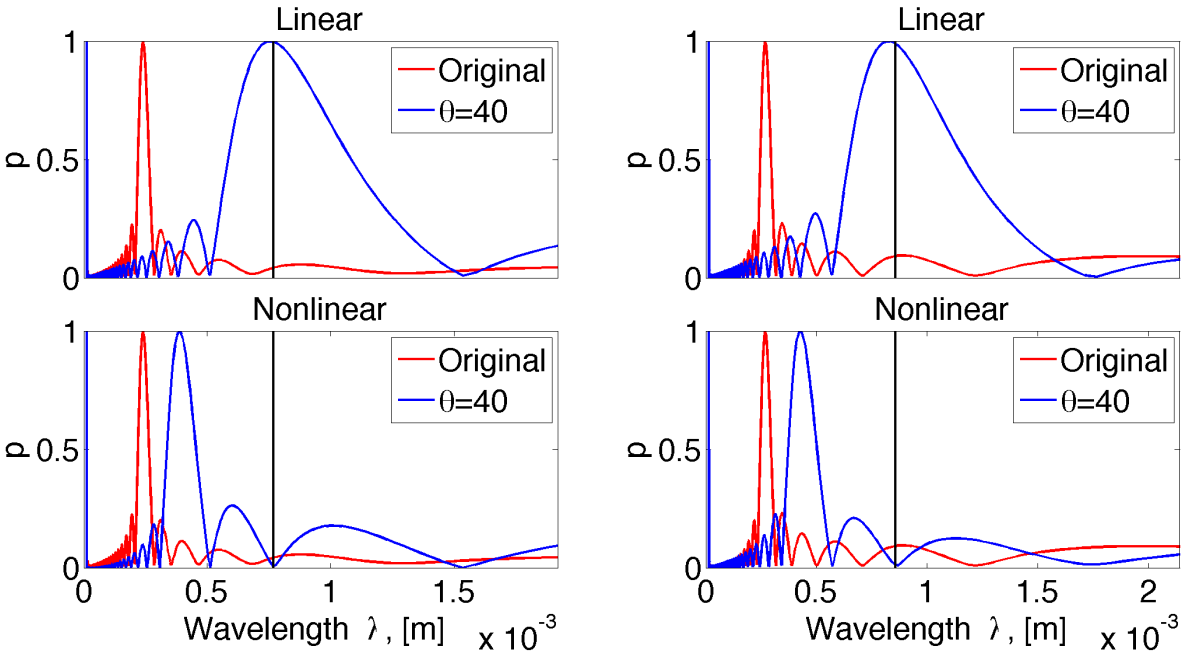

(a) (b)

Figure 9.25: FFT Spectral analysis of damped evolution for Surface1, $\theta = 40°$, damped.

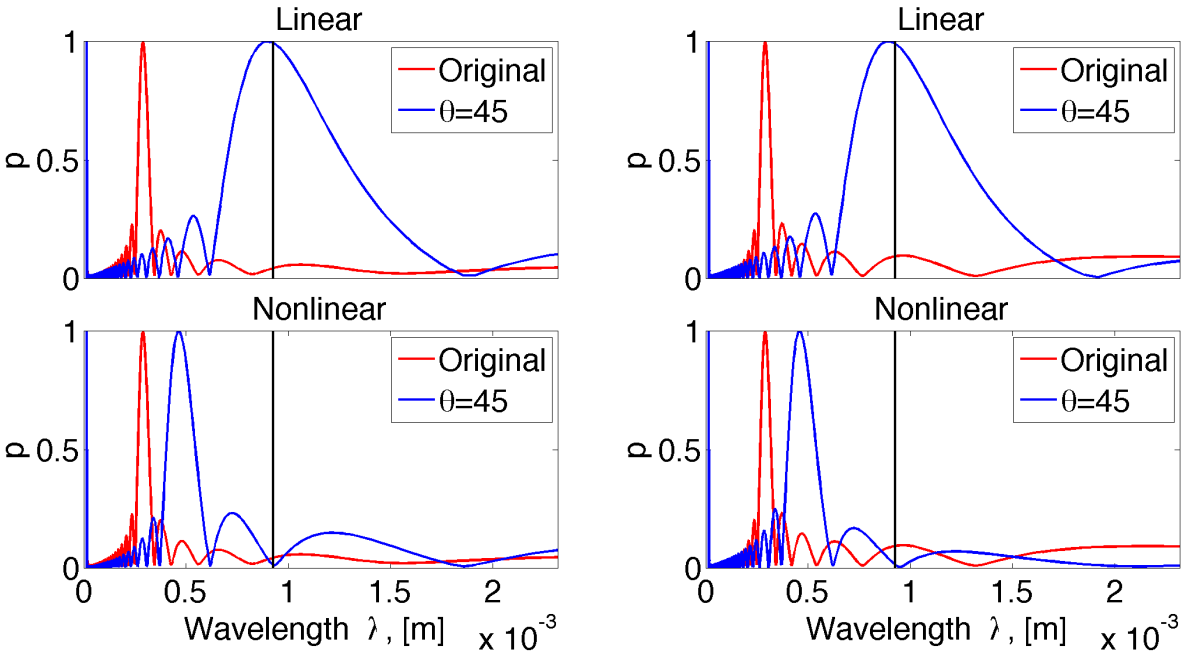

(a) (b)

Figure 9.26: FFT Spectral analysis of damped evolution for Surface1, $\theta = 45°$, damped.

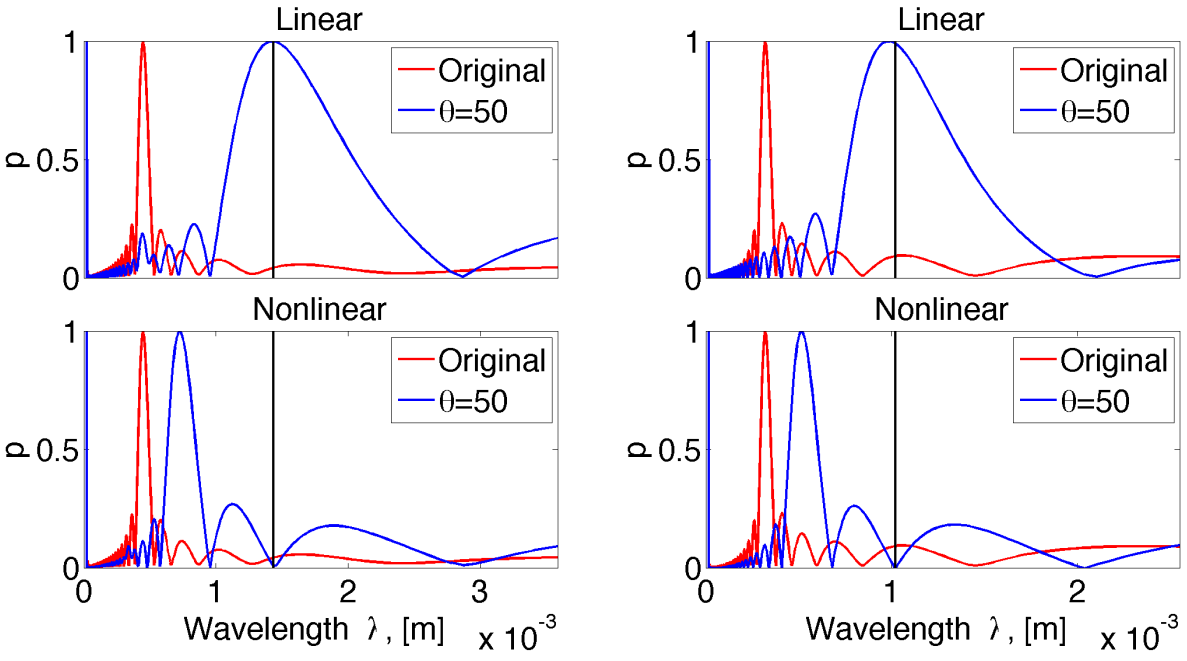

(a) (b)

Figure 9.27: FFT Spectral analysis of damped evolution for Surface1, $\theta = 50°$, damped.

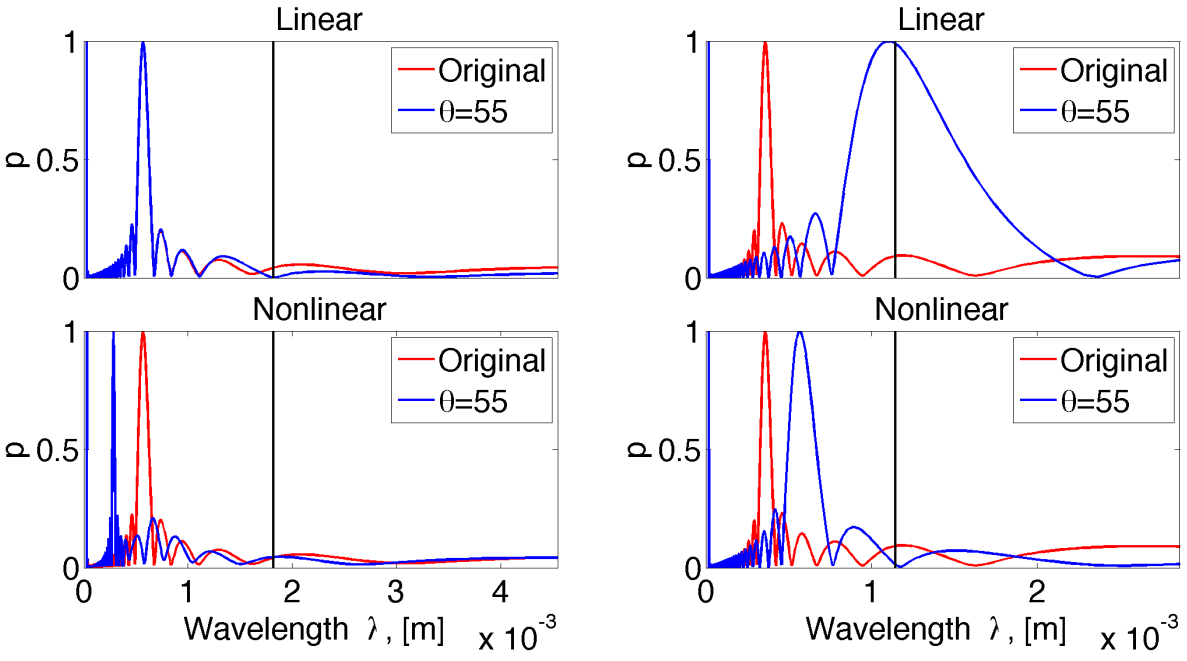

(a) (b)

Figure 9.28: FFT Spectral analysis of damped evolution for Surface1, $\theta = 55°$, damped.

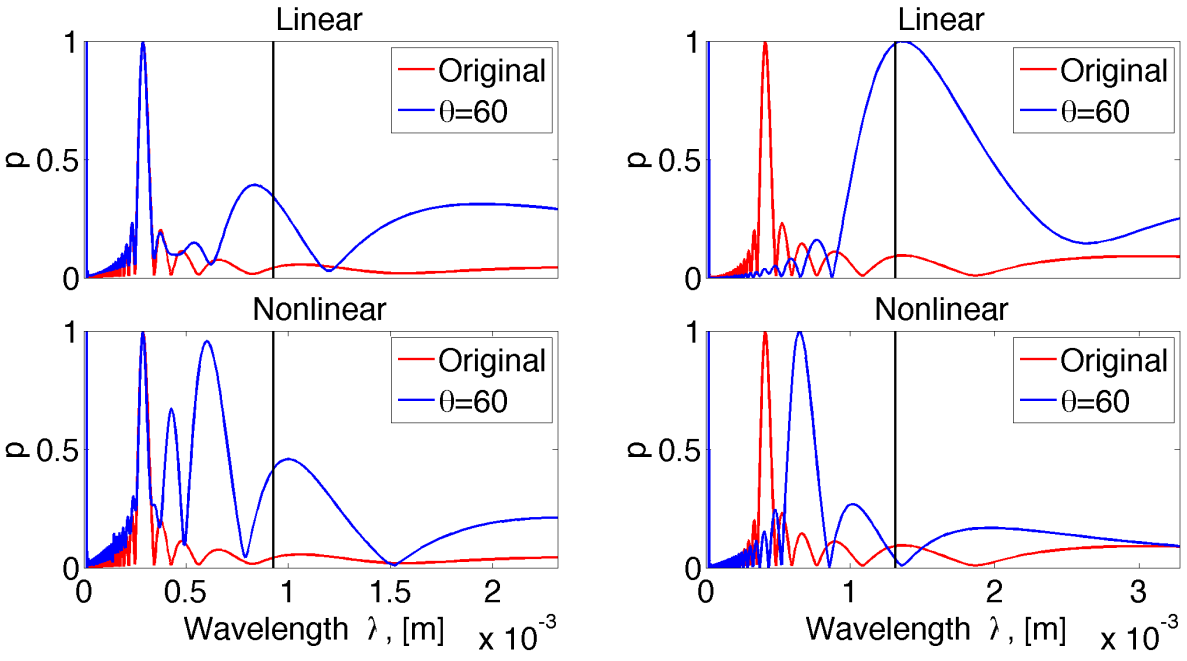

(a) (b)

Figure 9.29: FFT Spectral analysis of damped evolution for Surface1, $\theta = 60°$, damped.

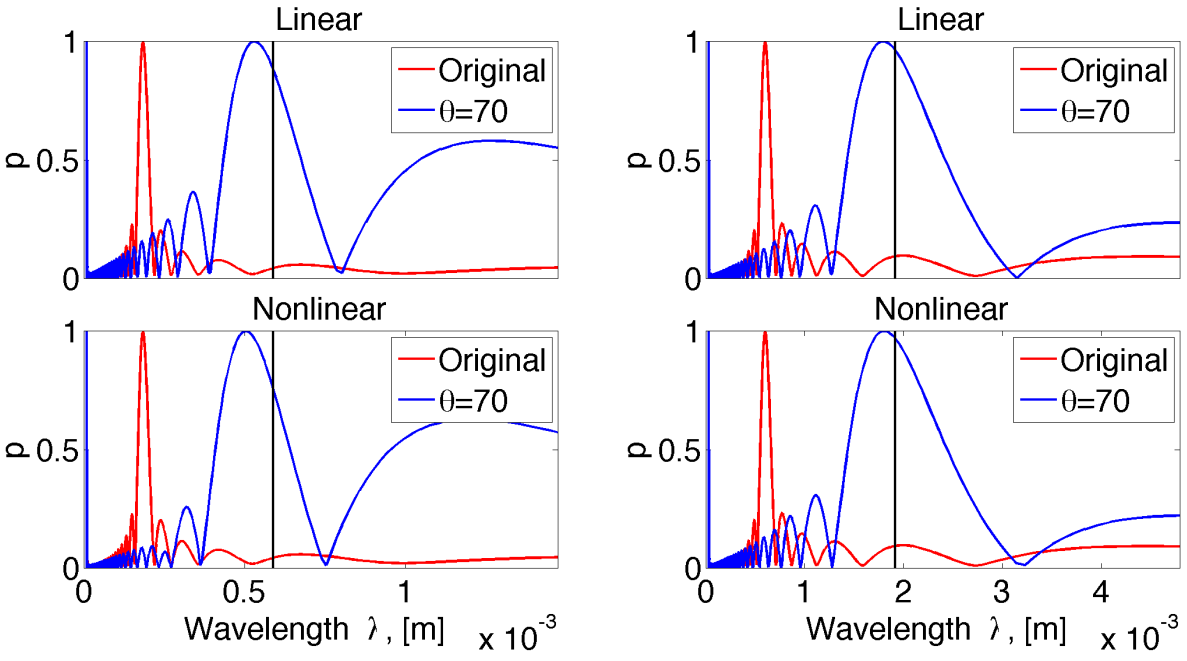

(a) (b)

Figure 9.30: FFT Spectral analysis of damped evolution for Surface1, $\theta = 70°$, damped.

References

[1] Vh-1000 measuring microscope system catalog (english). *Keyence Corporation*, Itasca, IL.

[2] RJ Asaro and WA Tiller. Interface morphology development during stress corrosion cracking: Part i. via surface diffusion. *Metallurgical Transactions*, 3(7):1789–1796, 1972.

[3] MS Bharathi, H Ramanarayan, and YW Zhang. Pattern formation and nonlinear evolution in alloy surfaces by ion-beam sputtering. *Applied Physics Letters*, 99(8):083103, 2011.

[4] Agnès Bogner, P-H Jouneau, Gilbert Thollet, D Basset, and Catherine Gauthier. A history of scanning electron microscopy developments: towards "wet-stem" imaging. *Micron*, 38(4):390–401, 2007.

[5] R Mark Bradley. Redeposition of sputtered material is a nonlinear effect. *Physical Review B*, 83(7):075404, 2011.

[6] R Mark Bradley and James ME Harper. Theory of ripple topography induced by ion bombardment. *Journal of Vacuum Science & Technology A: Vacuum, Surfaces, and Films*, 6(4):2390–2395, 1988.

[7] Mario Castro and Rodolfo Cuerno. Hydrodynamic approach to surface pattern formation by ion beams. *Applied Surface Science*, 258(9):4171–4178, 2012.

[8] E Chason, WL Chan, and MS Bharathi. Kinetic monte carlo simulations of ion-induced ripple formation: Dependence on flux, temperature, and defect concentration in the linear regime. *Physical Review B*, 74(22):224103, 2006.

[9] Gong Chen, Brandon Cloutier, Ning Li, Benson K Muite, Paul Rigge, Sudarshan Balakrishnan, Andre Souza, and Jeremy West. Parallel spectral numerical methods. *Blue Waters Undergraduate Petascale Module*, 2012.

[10] Ryan W Conversano, Dan M Goebel, Richard R Hofer, Taylor S Matlock, and Richard E Wirz. Magnetically shielded miniature hall thruster: development and initial testing. In *Proceedings of the thirty-third international electric propulsion conference, Electric Rocket Propulsion Society, Washington DC, USA*, 2013.

[11] G Costantini, S Rusponi, F Buatier de Mongeot, C Boragno, and U Valbusa. Periodic structures induced by normal-incidence sputtering on ag (110) and ag (001): flux and temperature dependence. *Journal of Physics: Condensed Matter*, 13(26):5875, 2001.

[12] Rodolfo Cuerno and Albert-László Barabási. Dynamic scaling of ion-sputtered surfaces. *Physical review letters*, 74(23):4746, 1995.

[13] KH De Grys, Alex Mathers, Ben Welander, and Vadim Khayms. Demonstration of 10,400 hours of operation on 4.5 kw qualification model hall thruster. *AIAA paper*, 6698:2010, 2010.

[14] KH De Grys, Alex Mathers, Ben Welander, and Vadim Khayms. Demonstration of 10,400 hours of operation on 4.5 kw qualification model hall thruster. *AIAA paper*, 6698:2010, 2010.

[15] Samuel F Edwards and DR Wilkinson. The surface statistics of a granular aggregate. In *Proceedings of the Royal Society of London A: Mathematical, Physical and Engineering Sciences*, volume 381, pages 17–31. The Royal Society, 1982.

[16] Jonah Erlebacher, Michael J Aziz, Eric Chason, Michael B Sinclair, and Jerrold A Floro. Spontaneous pattern formation on ion bombarded si (001). *Physical review letters*, 82(11):2330, 1999.

[17] Stefan Facsko, Thomas Bobek, Arne Stahl, Heinrich Kurz, and Thomas Dekorsy. Dissipative continuum model for self-organized pattern formation during ion-beam erosion. *Physical Review B*, 69(15):153412, 2004.

[18] Nasr Ghoniem and Daniel Walgraef. *Instabilities and Self-organization in Materials*. Oxford Univ. Press, 2008.

[19] Nasr M Ghoniem, Dan Goebel, Igor D Kaganovich, Yevgeny Raitses, Robert Shaefer, Alp Sehirlioglu, and Richard Wirz. Micro-engineered materials for electric propulsion and pulsed power. 2012.

[20] NM Ghoniem, Alp Sehirlioglu, Anton L Neff, Jean-Paul Allain, Brian Williams, and Reza Sharghi-Moshtaghin. Sputtering of molybdenum and tungsten nano rods and nodules irradiated with 150ev argon ions. *Applied Surface Science*, 331:299–308, 2015.

[21] Claude Godrèche. *Solids far from Equilibrium*, volume 1. Cambridge University Press, 1991.

[22] Dan M Goebel, Benjamin Jorns, Richard R Hofer, Ioannis G Mikellides, and Ira Katz. Pole-piece interactions with the plasma in a magnetically shielded hall thruster. In *50th AIAA/ASME/SAE/ASEE Joint Propulsion Conference*, page 3899, 2014.

[23] Dan M Goebel and Ira Katz. *Fundamentals of electric propulsion: ion and Hall thrusters*, volume 1. John Wiley & Sons, 2008.

[24] S Habenicht. Morphology of graphite surfaces after ion-beam erosion. *Physical Review B*, 63(12):125419, 2001.

[25] Yoshihiko Hirooka, Toshihiro Imoto, and Tadao Sano. Helium ion irradiation on chemically deposited molybdenum and molybdenum carbide. *Journal of Nuclear Materials*, 113(2-3):202–206, 1983.

[26] RR Hofer, DM Goebel, IG Mikellides, and Ira Katz. Design of a laboratory hall thruster with magnetically shielded channel walls, phase ii: Experiments. *AIAA paper*, 3788:2012, 2012.

[27] CE Huerta, TS Matlock, and RE Wirz. View factor modeling of sputter-deposition on micron-scale-architectured surfaces exposed to plasma. *Journal of Applied Physics*, 119(11):113303, 2016.

[28] Mehran Kardar, Giorgio Parisi, and Yi-Cheng Zhang. Dynamic scaling of growing interfaces. *Physical Review Letters*, 56(9):889, 1986.

[29] Adrian Keller and Stefan Facsko. Ion-induced nanoscale ripple patterns on si surfaces: theory and experiment. *Materials*, 3(10):4811–4841, 2010.

[30] I Koponen, M Hautala, and O-P Sievänen. Simulations of ripple formation on ion-bombarded solid surfaces. *Physical review letters*, 78(13):2612, 1997.

[31] Tanuj Kumar, Ashish Kumar, Dinesh Chander Agarwal, Nirnajan Prasad Lalla, and Dinakar Kanjilal. Ion beam-generated surface ripples: new insight in the underlying mechanism. *Nanoscale research letters*, 8(1):1–5, 2013.

[32] Yoshiki Kuramoto and Toshio Tsuzuki. Persistent propagation of concentration waves in dissipative media far from thermal equilibrium. *Progress of theoretical physics*, 55(2):356–369, 1976.

[33] Nils Laegreid and GK Wehner. Sputtering yields of metals for ar+ and ne+ ions with energies from 50 to 600 ev. *Journal of Applied Physics*, 32(3):365–369, 1961.

[34] GZ Li, TS Matlock, DM Goebel, CA Dodson, CS Matthes, NM Ghoniem, and RE Wirz. Iin situ sputtering yield measurements of molybdenum bombarded by a cusped argon plasma. *Submitted to Plasma Sources Science and Technology*, 2016.

[35] GZ Li, TS Matlock, DM Goebel, CA Dodson, and RE Wirz. Implementation of in situ diagnostics for sputter yield measurements in a focused plasma. In *52nd AIAA/ASME/SAE/ASEE Joint Propulsion Conference*, July 2016.

[36] Charbel S Madi, Eitan Anzenberg, Karl F Ludwig Jr, and Michael J Aziz. Mass redistribution causes the structural richness of ion-irradiated surfaces. *Physical review letters*, 106(6):066101, 2011.

[37] Maxim A Makeev, Rodolfo Cuerno, and Albert-Laszlo Barabasi. Morphology of ion-sputtered surfaces. *Nuclear Instruments and Methods in Physics Research Section B: Beam Interactions with Materials and Atoms*, 197(3):185–227, 2002.

[38] TS Matlock, DM Goebel, R Conversano, and RE Wirz. A dc plasma source for plasma–material interaction experiments. *Plasma Sources Science and Technology*, 23(2):025014, 2014.

[39] Noriaki Matsunami, Yasunori Yamamura, Yukikazu Itikawa, Noriaki Itoh, Yukio Kazumata, Soji Miyagawa, Kenji Morita, Ryuichi Shimizu, and Hiroyuki Tawara. Energy dependence of the ion-induced sputtering yields of monatomic solids. *Atomic Data and Nuclear Data Tables*, 31(1):1–80, 1984.

[40] DM Mattox and DJ Sharp. Influence of surface morphology on the low energy hydrogen ion erosion yields of beryllium. *Journal of Nuclear Materials*, 80(1):115–119, 1979.

[41] William W Mullins. Theory of thermal grooving. *Journal of Applied Physics*, 28(3):333–339, 1957.

[42] M Navez, C Sella, and D Chaperot. Nonlinear ripple dynamics on amorphous surfaces patterned by ion beam sputtering. *Czetch Republic Academy of Science*, 254:240, 1962.

[43] Scott A Norris, Juha Samela, Laura Bukonte, Marie Backman, Flyura Djurabekova, Kai Nordlund, Charbel S Madi, Michael P Brenner, and Michael J Aziz. Molecular dynamics of single-particle impacts predicts phase diagrams for large scale pattern formation. *Nature communications*, 2:276, 2011.

[44] Jérôme Paret. Long-time dynamics of the three-dimensional biaxial grinfeld instability. *Physical Review E*, 72(1):011105, 2005.

[45] Peter Y Peterson, David T Jacobson, David H Manzella, and Jeremy W John. The performance and wear characterization of a high-power high-isp nasa hall thruster. *AIAA Paper*, 4243:2005, 2005.

[46] JE Polk, JR Anderson, JR Brophy, VK Rawlin, MJ Patterson, J Sovey, and J Hamley. An overview of the results from an 8200 hour wear test of the nstar ion thruster. *AIAA Paper*, 2446:1999, 1999.

[47] Michael Rodahl, Fredrik Höök, Anatol Krozer, Peter Brzezinski, and Bengt Kasemo. Quartz crystal microbalance setup for frequency and q-factor measurements in gaseous and liquid environments. *Review of Scientific Instruments*, 66(7):3924–3930, 1995.

[48] D Rosenberg and GK Wehner. Sputtering yields for low energy he+-, kr+-, and xe+-ion bombardment. *Journal of Applied Physics*, 33(5):1842–1845, 1962.

[49] S Rusponi, C Boragno, and U Valbusa. Ripple structure on ag (110) surface induced by ion sputtering. *Physical review letters*, 78(14):2795, 1997.

[50] Shahram Sharafat, Nasr M Ghoniem, Michael Anderson, Brian Williams, Jake Blanchard, Lance Snead, HAPL Team, et al. Micro-engineered first wall tungsten armor for high average power laser fusion energy systems. *Journal of nuclear materials*, 347(3):217–243, 2005.

[51] Daisuke Shindo and Tetsuo Oikawa. Energy dispersive x-ray spectroscopy. In *Analytical Electron Microscopy for Materials Science*, pages 81–102. Springer, 2002.

[52] Peter Sigmund. Theory of sputtering. i. sputtering yield of amorphous and polycrystalline targets. *Physical review*, 184(2):383, 1969.

[53] Peter Sigmund. A mechanism of surface micro-roughening by ion bombardment. *Journal of Materials Science*, 8(11):1545–1553, 1973.

[54] GI Sivashinsky. Nonlinear analysis of hydrodynamic instability in laminar flamesi. derivation of basic equations. *Acta astronautica*, 4(11):1177–1206, 1977.

[55] David J Srolovitz. On the stability of surfaces of stressed solids. *Acta Metallurgica*, 37(2):621–625, 1989.

[56] U Valbusa, C Boragno, and F Buatier de Mongeot. Nanostructuring surfaces by ion sputtering. *Journal of Physics: Condensed Matter*, 14(35):8153, 2002.

[57] J Villain. Continuum models of crystal growth from atomic beams with and without desorption. *Journal de physique I*, 1(1):19–42, 1991.

[58] E Vitral. Nano-patterning of surfaces by ion sputtering: Numerical study of the anisotropic damped kuramoto-sivashinsky equation. Master's thesis, Universidade do Estado do Rio de Janeiro, 2015.

[59] Daniel Walgraef. Nano-patterning of surfaces by ion sputtering. *Working comments and thoughts*, Feb 2014.

[60] Noah Zachary Warner. *Theoretical and experimental investigation of Hall thruster miniaturization*. PhD thesis, Massachusetts Institute of Technology, 2007.

[61] CH Weijsenfeld, A Hoogendoorn, and M Koedam. Sputtering of polycrystalline metals by inert gas ions of low energy (100-1000 ev). *Physica*, 27, 1961.

[62] Richard E Wirz, John R Anderson, and Ira Katz. Time-dependent erosion of ion optics. *Journal of Propulsion and Power*, 27(1):211–217, 2011.

[63] Y Yamamura and Shigeru Shindo. An empirical formula for angular dependence of sputtering yields. *Radiation effects*, 80(1-2):57–72, 1984.

[64] Yasunori Yamamura, N Matsunami, and N Itoh. Theoretical studies on an empirical formula for sputtering yield at normal incidence. *Radiation Effects*, 71(1-2):65–86, 1983.

[65] Yasunori Yamamura and Hiro Tawara. Energy dependence of ion-induced sputtering yields from monatomic solids at normal incidence. *Atomic data and nuclear data tables*, 62(2):149–253, 1996.

[66] Wei H Yang and David J Srolovitz. Surface morphology evolution in stressed solids: surface diffusion controlled crack initiation. *Journal of the Mechanics and Physics of Solids*, 42(10):1551–1574, 1994.

[67] JF Ziegler, Jerome J Cuomo, and J Roth. Reduction of ion sputtering yield by special surface microtopography. *Applied Physics Letters*, 30(6):268–271, 1977.

[68] Kirk A Zoerb, John D Williams, Desiree D Williams, and Azer P Yalin. Differential sputtering yields of refractory metals by xenon, krypton, and argon ion bombardment at normal and oblique incidences. In *29th International Electric Propulsion Conference*, pages 2005–293, 2005.